

University of California  
Santa Barbara

# Studying quantum dynamics in driven degenerate gases

A dissertation submitted in partial satisfaction  
of the requirements for the degree

Bachelor of Science  
in  
Physics

by

Alec Jiahua Cao

Committee in charge:

Professor David Weld, Chair  
Dr. Tengiz Bibilashvili

June 2021

The Dissertation of Alec Jiahua Cao is approved.

---

Dr. Tengiz Bibilashvili

---

Professor David Weld, Committee Chair

June 2021

Studying quantum dynamics in driven degenerate gases

Copyright © 2021

by

Alec Jiahua Cao

## Acknowledgements

First and foremost, I'd like to thank my parents for all their support. I'm so grateful for the opportunities and life you've provided me, as well as the work ethic you've instilled in me.

I spent almost my entire undergraduate education in Prof. David Weld's lab, and during that time I've been extremely fortunate to learn from so many amazing mentors. To Dr. Toshihiko Shimasaki, I am indebted to all the wisdom and Blaze pizza that you shared with me. Given how "experimentally-challenged" I am, I constantly relied on your incredible know-how in the lab, and you have been an absolutely critical piece in my progress. I still remember you teaching me how to trigger an oscilloscope just a few years back, and that was the first of many lessons learned over these past few years., I'm holding onto memories of many amazing, insightful and hilarious conversations we have had since then, and will miss chatting over Freebirds' nachos and McDonalds nuggets with you. To Peter Dotti, its been a lot of fun chatting with you about physics over the years. You taught me how to think critically through all aspects of a problem and challenge my own often-wrong intuitions, and that's been an absolutely crucial part of my development. You've also been such a great friend to me and I will cherish all of the ridiculous (in a good way) discussions we've had. To Cora Fujiwara, Kevin Singh, and Shankari Rajagopal, thank you for all the knowledge and kindness you offered me as I slowly assimilated myself into this group.

To my Lithium labmates over the last couple years, it's been a pleasure and honor working with you all! Firstly, I appreciate you all putting up with my stubbornness and strong opinions when it comes to the physics. I had a lot of fun working on this experiment with everyone and I'm glad to have helped this experiment transition to a new era in terms of personnel. To Roshan Sajjad, it's been a blast! I still remember

the great times at our first DAMOP getting AJ Bomber's and cheese curds and steak and cheesecake. I feel we bonded on a spiritual level on that trip, and since then we've learned so much about machine running and data analysis and simulations and actual physics together and from each other. I'm really pumped to see you take the experiment to another level and do awesome science over the next few years. To Quinn Simmons, it's been an amazing journey working together with you. I remember our days trapped together on the fourth floor, and you helping me out with the learning the basics of optics. It was really fun learning how to run the machine together and I deeply appreciate how great of a friend you've been to me. To Hector Mas, we've only known each other for about half a year, but I've deeply enjoyed our many conversations. I learned a lot of AMO from you and I hope I was able to repay with a bit of condensed matter knowledge. Also, I hope I wasn't too much of a bother as I strolled over to the DL every other afternoon to chat, but they were great chats! Keep loving Drake! To Jeremy Tanlimco and Eber Nolasco-Martinez, you guys are doing a great job running the experiment. Keep up the good work and you guys will do awesome science.

In addition to my lithium labmates, I also need to thank our theory collaborator Prof. Victor Galitski at the Joint Quantum Institute and University of Maryland, as a third of this thesis has sprouted from the idea you proposed to us back at the end of 2019. I am deeply indebted to all the ideas you've taught and shared with us through this collaboration, and look forward to more fruitful discussion in the future.

A lot of my early efforts in the group were dedicated to the quantum interfaces project in collaboration with Prof. Ania Jayich's lab. To Shuo Ma and Sophia Han, thank you for being amazing friends and mentors to me. You both helped me build up confidence as a new researcher, and I had so much fun chatting about life with you guys while putting together the experiment. To Dr. Maxime Joos, we didn't get to work together directly much, but I've marveled from afar at how you've pushed this project to the next

level. It was always a pleasure chatting with you. And of course to Prof. Ania Jayich, I'm so grateful to have had the chance to work under and learn from you through this collaboration. I learned so much about how to ask the right questions and figure out how to progress an experiment forward from listening to you at the QI meetings. I am extremely appreciative of how kind and supportive you've been to me as an advisor, and your honest thoughts were extremely helpful in my graduate school decision making.

The College of Creative Studies program was absolutely vital in helping me mature as a thinker, and I also have so many fond personal memories with my many CCS physics peers. To Charles Zhang, Jacob Miller, Mark Zhao, David Wang, Max Prichard (my Weld lab compatriot) and many others, you are all inspirations to me and I will always look back fondly to all the homework, meals and laughter we bonded over together. To Dolev Bluvstein, thank you for being an amazing mentor who was always willing to give me great advice no matter what silly questions I was asking. And when it comes to CCS physics, there's no more important person than Dr. B. I still vividly remember how nervous I was chatting with you in your office for the first time as a prospective student, and the vision of CCS you left me with over that 30 minute conversation totally won me over. Since then we've had so many more deep and cheerful conversations over the last 4 years, and I've had the privilege of listening to you deliver the beautiful physics introduction series that transformed the way I approach and think about this wonderful subject. You are an incredible person in character and spirit, and I feel so fortunate to be one of the many students whose lives you've touched for the better.

Finally, I need and want to thank my advisor Prof. David Weld. It's no hyperbole to say that you have been a transformative force in my life. I still remember the first conversation we had back when I was still in high-school, where you convinced me to apply for CCS. Looking back, that was a rather fateful call that started this journey I've been on at UCSB. A little less than a year later, I began working in your group, rapidly

falling in love with this incredible field of atomic and condensed matter physics with cold atoms. From our earliest conversations when I could barely understand the basic optics concepts you were trying to teach me, to our more recent discussions and debates on more esoteric topics in quantum chaos and the like, I feel so fortunate to have worked and learned under a PI with such an infectious enthusiasm for physics. On the advising side, I'm extremely grateful for how you continued to provide and encourage me to seize new, challenging opportunities in research. I've reached heights that I honestly couldn't have imagined just 4 years ago, and so much of that is from the confidence you've instilled in me as a scientist. You allowed me to work on so many projects, and through that I've gained so much knowledge and experience, both scientific and personal, from the breadth of ideas and people I've come across in these endeavors. Thank you so much for the incredible mentorship and partnership over the last 4 year!

# Curriculum Vitæ

Alec Jiahua Cao

## Education

2021 B.S. in Physics (Expected), University of California, Santa Barbara.

## Publications

*Prethermal Dynamical Localization and the Emergence of Chaos in a Kicked Interacting Quantum Gas.* **A. Cao**, R. Sajjad, H. Mas, E. Q. Simmons, J. L. Tanlimco, E. Nolasco-Martinez, T. Shimasaki, E. Kondakci, V. Galitski, and D. M. Weld, arXiv:2106.09698 (2021).

*Transport controlled by Poincare orbit topology in a driven inhomogeneous lattice gas.* **A. Cao**, R. Sajjad, E. Q. Simmons, C. J. Fujiwara, T. Shimasaki, and D. M. Weld, Phys. Rev. Research 2, 032032 (2020).

*Probing Nonexponential Decay in Floquet-Bloch Bands.* **A. Cao**, C. J. Fujiwara, R. Sajjad, E. Q. Simmons, E. Lindroth, and D. Weld, Zeitschrift für Naturforschung 75, 443448 (2020).

*Quantifying and Controlling Prethermal Nonergodicity in Interacting Floquet Matter.* K. Singh, C. J. Fujiwara, Z. A. Geiger, E. Q. Simmons, M. Lipatov, **A. Cao**, P. Dotti, S. V. Rajagopal, R. Senaratne, T. Shimasaki, M. Heyl, A. Eckardt, and D. M. Weld, Phys. Rev. X 9, 041021 (2019).

## Awards

2021 UCSB Chancellor's Award for Undergraduate Research Excellence  
2021 NSF GRFP  
2021 NDSEG (declined)  
2021 Churchill Scholarship  
2020 UCSB Physics Worster Fellow  
2020 Barry Goldwater Scholarship  
2019 UCSB CCS Physics Roig Fellow  
2018 UCSB MRL Future Leaders of Advanced Materials  
2017 UCSB Regents Scholarship

## Abstract

Studying quantum dynamics in driven degenerate gases

by

Alec Jiahua Cao

Dynamical control of out-of-equilibrium quantum matter represents a rapidly advancing frontier in quantum science and technology. Recently ultracold atom experiments have greatly pushed forward the field of Floquet engineering, the control of quantum systems with a time-periodic drive. In this thesis, I will discuss experimental efforts utilizing a  $^7\text{Li}$  Bose-Einstein condensate (BEC) in a periodically modulated laser potential as a tool for understanding and controlling quantum Floquet dynamics across a broad range of physical contexts. In particular, I will discuss 3 primary efforts: an application of dynamical band-structure engineering for probing the foundational nature of quantum decay, a realization of how transport properties of quantum gases connect to the topology of classical phase space orbits, and an exploration of the emergence of many-body quantum chaos in interacting Floquet matter.

# Contents

<b>Curriculum Vitae</b>	<b>viii</b>
<b>Abstract</b>	<b>ix</b>
<b>1 Introduction</b>	<b>1</b>
1.1 Permissions and Attributions . . . . .	2
<b>2 Background</b>	<b>4</b>
2.1 BEC Dynamics . . . . .	4
2.2 Band Theory and Tight-Binding Models . . . . .	7
2.3 Tilted Lattices . . . . .	11
2.4 Floquet Theory . . . . .	15
<b>3 Engineering Tunable Floquet-Bloch-Zener Decay</b>	<b>19</b>
3.1 Nonexponential Quantum Decay . . . . .	20
3.2 Tunable Decay in Driven Lattices . . . . .	24
3.3 Toward Nonexponential Floquet-Bloch Decay . . . . .	29
<b>4 Transport Controlled by Semiclassical Poincaré Topology</b>	<b>31</b>
4.1 Dynamic Localization and Super Bloch Dynamics . . . . .	32
4.2 Poincaré Topology and Bloch Transport under Slow Amplitude Modulation	35
<b>5 Investigation of the Many-Body Quantum Kicked Rotor</b>	<b>45</b>
5.1 Diffusive Chaos in the Classical Kicked Rotor . . . . .	45
5.2 Localization in the Quantum Kicked Rotor (QKR) . . . . .	48
5.3 Prethermalization and Delocalization in the Interacting Kicked Rotor . .	56
5.4 Time Reversal with Quantum Resonances . . . . .	67
5.5 Many-body Dynamical Localization (MBDL) in Kicked XXZ Chains . . .	76
<b>A Numerical TDSE Simulation with Time-Splitting Spectral Methods</b>	<b>81</b>
A.1 Time-Splitting Spectral Integration . . . . .	82
A.2 Floquet-Bloch Atom Interferometry . . . . .	88

<b>B</b>	<b>Fringe Removal for Absorption Images</b>	<b>92</b>
B.1	Absorption Imaging . . . . .	93
B.2	Ideal Reference Fringe Removal Algorithm . . . . .	94
<b>C</b>	<b>Derivation of Ideal QKR OTOC</b>	<b>101</b>
<b>D</b>	<b>Probing non-exponential decay in Floquet-Bloch bands (preprint)</b>	<b>106</b>
<b>E</b>	<b>Transport controlled by Poincare orbit topology in a driven inhomogeneous lattice gas (preprint)</b>	<b>114</b>
<b>F</b>	<b>Prethermal Dynamical Localization and the Emergence of Chaos in a Kicked Interacting Quantum Gas (preprint)</b>	<b>120</b>
	<b>Bibliography</b>	<b>138</b>

# Chapter 1

## Introduction

The quantum nature of large ensembles of particles becomes manifest at low temperatures. At room temperature, the properties of gases are often well described by simple classical kinetic theory and statistical mechanics; the quantum waviness of the particles is ignorable due to the large average distance between constituents, and the statistical properties of the system are described by the famous Boltzmann distribution  $1/e^{E/k_B T}$ . Quantum mechanics dictates however that each atom (of a single atomic number, isotope, etc.) is identical and indistinguishable (in principle, not just in practice), and this causes an ever so slight modification to the Boltzmann distribution  $1/(e^{E/k_B T} \pm 1)$  (+1 for fermions, -1 for bosons). For the bosonic case, this seemingly inconsequential change leads to the remarkable phenomena of Bose-Einstein condensation (BEC). As the temperature of the gas is lowered through a critical value and the wavefunctions of the atoms begin to overlap, a phase transition occurs wherein a macroscopic fraction of the ensemble all enter into the lowest quantum energy level.

BEC is now a widely-studied platform across the world, providing physicists an extremely versatile tool for preparing an ensemble of many particles into a desired quantum state and observing their behavior under different dynamical evolution protocols. In some

cases, we are interested in using the extreme level of control over the BEC to engineer certain dynamical responses, which may help to experimentally verify long-standing theoretical predictions or which could be used as quantum sensors for practical metrological applications. In others, we seek to use this platform as a quantum simulator to answer complicated questions in many-body condensed matter physics which are intractable to current computing capabilities and are obscured by imperfections in real world materials. In this thesis, I will describe a variety of experimental (and slightly theoretical) works I have performed in Prof. David Weld's lab which touches conceptually on these many possibilities in using BEC for quantum exploration (of course there are many, many more!). The work here focuses particularly on the dynamics of BEC's subjected to optical lattices, artificial crystals formed by interfering laser beams, which are additionally periodically modulated in time. These experiments are particularly well-suited to studying transport/localization phenomena and the dynamics of external/kinetic degrees of freedom.

## 1.1 Permissions and Attributions

1. The content of chapter 3 is the result of a collaboration with Cora J. Fujiwara, Roshan Sajjad, Ethan Q. Simmons, Eva Lindroth and David Weld, and has previously appeared in the *Zeitschrift für Naturforschung A* [1]. It is reproduced here with the permission of *Zeitschrift für Naturforschung A*: <https://www.degruyter.com/document/doi/10.1515/zna-2020-0020/html>.
2. The content of chapter 4 is the result of a collaboration with Roshan Sajjad, Ethan Q. Simmons, Cora J. Fujiwara, Toshihiko Shimasaki, and David M. Weld, and has previously appeared in the *Physical Review Research* [2]. It is reproduced here with the permission of *Physical Review Research*: <https://journals.aps.org/>

[prresearch/abstract/10.1103/PhysRevResearch.2.032032](https://arxiv.org/abs/10.1103/PhysRevResearch.2.032032).

3. The content of chapter 5 is the result of a collaboration with Roshan Sajjad, Hector Mas, Ethan Q. Simmons, Jeremy L. Tanlimco, Eber Nolasco-Martinez Toshihiko Shimasaki, Esat Kondakci, Victor Galitski, and David M. Weld [3]. The preprint can be found here: <https://arxiv.org/abs/2106.09698>.

# Chapter 2

## Background

The experiments outlined in this thesis largely concern the ultracold  ${}^7\text{Li}$  apparatus. The details of our  ${}^7\text{Li}$  BEC production are extensively outlined in the theses of Zachary Geiger [4], Kevin Singh [5] and Cora Fujiwara [6], and will not be detailed further here. A good introductory review of making BEC can be found in [7]. The bread and butter of the experiment is examining BEC dynamics in optical lattices, for which a good review can be found in [8]. Some other useful and very thorough reviews on understanding BEC can be found in [9, 10].

### 2.1 BEC Dynamics

Here I discuss the simplified theoretical framework for understanding the behavior of BECs. This discussion largely follows Pethick and Smith [11]. For  $N$  identical particles, a general Hamiltonian capturing two body interactions can be written as

$$H = \sum_{i=1}^N \left[ \frac{\mathbf{p}_i^2}{2m} + V(\mathbf{r}_i) \right] + \frac{1}{2} \sum_{i=1}^N \sum_{j \neq 1}^N U(\mathbf{r}_i - \mathbf{r}_j). \quad (2.1)$$

Here  $V$  describes a single particle external potential and  $U$  the two-body interaction. We in general consider a pseudopotential describing contact interactions

$$U(\mathbf{r}) = U_0 \delta(\mathbf{r}) = \frac{4\pi\hbar^2 a_S}{m} \delta(\mathbf{r}). \quad (2.2)$$

This pseudopotential is characterized by only one parameter which is the s-wave scattering length  $a_S$ . The BEC is generically a many-body quantum system which in first quantization is described by a many-body wavefunction  $\Psi$  with the normalization  $\langle \Psi | \Psi \rangle = N$ . Because the particles are condensed into a single state, the many-body wavefunction is simply a tensor product of identical single-particle wavefunctions  $|\phi\rangle$  in the many-body Hilbert space  $|\Psi\rangle = |\phi\rangle \otimes |\phi\rangle \dots$ . The free energy is then computed as

$$F[\Psi] = \frac{\langle \Psi | H | \Psi \rangle}{\langle \Psi | \Psi \rangle} - \mu \langle \Psi | \Psi \rangle = N \int d\mathbf{r} \left[ \frac{\hbar^2}{2m} |\nabla \phi|^2 + (V(\mathbf{r}) - \mu) |\phi|^2 + \frac{N-1}{2} U_0 |\phi|^4 \right]. \quad (2.3)$$

We then introduce the condensate wavefunction and particle density

$$\psi(\mathbf{r}) = \sqrt{N} \phi(\mathbf{r}), \quad n(\mathbf{r}) = |\psi(\mathbf{r})|^2. \quad (2.4)$$

Minimizing the free energy (2.3) with respect to  $\psi^*$ , we get the time-independent Gross-Pitaevskii equation

$$\left[ -\frac{\hbar^2}{2m} \nabla^2 + V(\mathbf{r}) + U_0 |\psi|^2 \right] \psi = \mu \psi. \quad (2.5)$$

This describes the steady-state solution and has the form of a nonlinear time-dependent Schrodinger equation. To describe our interacting condensate after held in the optical dipole trap (ODT), it is useful to make the Thomas-Fermi approximation where the

kinetic energy term is ignored. Then one can directly solve for the position-space density as

$$n(\mathbf{r}) = \frac{\mu - V(\mathbf{r})}{U_0}. \quad (2.6)$$

So in the ODT, the condensate density can be seen to have a parabolic profile as the trapping potential is Gaussian and thus has leading order quadratic behavior. This profile is a signature of BEC and can be clearly seen in our absorption images. The condensate vanishes in the  $i$ th direction for a trapping potential of  $\omega_i$  outside of radii

$$R_i = \frac{2\mu}{m\omega_i}. \quad (2.7)$$

In general, one will still observe Gaussian tails beyond this radius due to finite thermal population outside of the condensate.

Next we seek an equation to describe the dynamics of the condensate. This is computed in the Lagrangian formalism. One can define the Lagrangian density  $\mathcal{L}$  as

$$\mathcal{L} = \frac{i\hbar}{2} \left( \psi^* \frac{\partial \psi}{\partial t} - \psi \frac{\partial \psi^*}{\partial t} \right) - \left[ \frac{\hbar^2}{2m} |\nabla \psi|^2 + V(\mathbf{r}) |\psi|^2 + \frac{U_0}{2} |\psi|^4 \right]. \quad (2.8)$$

Then applying the variational principle for the action, we find the time-dependent Gross-Pitaevskii equation

$$i\hbar \frac{\partial \psi}{\partial t} = \left( -\frac{\hbar^2}{2m} \nabla^2 + V(\mathbf{r}, t) + U_0 |\psi|^2 \right) \psi. \quad (2.9)$$

Once again this simply looks like a time-dependent nonlinear Schrodinger equation, with the nonlinearity corresponding to a mean-field energy proportional to the local condensate density. Here I've allowed the external potential to possess arbitrary time-dependence,

though dynamical instability can develop; even in time-independent cases there can in principle be large quantum fluctuations which make this description inaccurate. The mean-field energy is tunable in the  ${}^7\text{Li}$  experiment by manipulating a magnetic field which varies the scattering length around the Feshbach resonance. The approximate dependence of the scattering length on the field is given by

$$a_S = a_{\text{bg}} \left( 1 - \frac{\Delta}{B - B_0} \right) \quad (2.10)$$

Detailed numbers can be found in [4, 12]. For many experiment, we are able to set  $a_S \approx 0$  to a great approximation. In these cases, this allows us to study a noninteracting wavefunction which is simply governed by a single-particle Schrodinger equation

$$i\hbar \frac{\partial \psi}{\partial t} = \left( -\frac{\hbar^2}{2m} \nabla^2 + V(\mathbf{r}, t) \right) \psi. \quad (2.11)$$

In this last case the normalization can be taken as  $\int d\mathbf{r} |\psi|^2 = 1$ .

## 2.2 Band Theory and Tight-Binding Models

The most common potential considered on the  ${}^7\text{Li}$  experiment is a 1-dimensional optical lattice of pancakes. This is formed by applying counter-propagating laser beams which are far red-detuned from resonance. In this case, the average effect on time-scales much slower than optical frequencies is a trapping AC Stark shift. One can compute this from first principles given laser beam parameters, but in practice we typically calibrate for the so-called lattice depth  $V_0$  using techniques such as Kapitza-Dirac diffraction and modulation spectroscopy. Many times the transverse dynamics within the pancakes are ignorable, so that the external potential for light of wavelength  $\lambda$  (or wavevector  $k_L =$

$2\pi/\lambda$ ) is given by

$$V(x) = -\frac{V_0}{2} \cos(2k_L x). \quad (2.12)$$

This potential is spatially periodic. Namely it has lattice spacing  $d = \lambda/2$  such that

$$V(x + d) = V(x). \quad (2.13)$$

This motivates us to review simple band theory of condensed matter physics that is used routinely on the  $^7\text{Li}$  experiment. Band theory is the single-particle approximation to solid-state systems which have spatially periodic crystalline structure. Here I will restrict to 1D for notational simplicity, though generalization to multiple dimensions is fairly trivial. Bloch's theorem states that for Hamiltonians with the spatial periodicity property (2.13), the eigenstates of the time-independent Schrodinger equations can be decomposed as

$$\psi(x) = e^{ikx} u_k(x), \quad u_k(x + d) = u_k(x). \quad (2.14)$$

So the eigenfunctions are plane waves modulated by envelopes with the spatial periodicity of the lattice. The normalization of the Bloch waves is over a unit cell

$$\int_0^d |u_k(x)|^2 dx = 1. \quad (2.15)$$

Acting  $H$  on these states we can derive the so-called Bloch Hamiltonian

$$H_k = \frac{(p + \hbar k)^2}{2m} + V(x), \quad (2.16)$$

which defines the eigenvalue problem

$$H_k u_{nk}(x) = \mathcal{E}_{nk} u_{nk}(x). \quad (2.17)$$

The index  $n$  is introduced since the eigenvalue problem in general has an infinite spectrum of discrete solutions. Here  $k$  denotes the quasimomentum which can be restricted to the first Brillouin zone, which in the 1D case can be taken to be  $[-\pi/d, \pi/d]$ . This is because  $V(x)$  admits a Fourier decomposition which contains only coefficients for integer multiples of the reciprocal lattice vector  $2k_L$ , and thus couples only states at the same quasimomentum in different Brillouin zones. Similarly, one can perform the same decomposition for the  $u_{nk}$ . Letting  $G$  denote reciprocal lattice vectors, explicitly we write

$$V(x) = \sum_G V_G e^{iGx}, \quad u_{nk}(x) = \sum_G c_{k+G} e^{iGx}. \quad (2.18)$$

Inserting into the eigenvalue problem defined by (2.16) and (2.17), we have a matrix equation defined by

$$\frac{\hbar^2(k+G)^2}{2m} c_{k+G} + \sum_{G'} V_{G-G'} c_{k+G'} = \mathcal{E}_{nk} c_{k+G}. \quad (2.19)$$

For the cosine optical lattice (2.12),  $V_G$  only has two coefficients which are  $V_{\pm 2k_L} = -V_0/4$ . Thus we simply have a tridiagonal matrix with constants  $-V_0/4$  on the first off-diagonal and a kinetic energy  $\hbar^2(k+2jk_L)^2/2m$  for integer  $j$  on the diagonal. This can be easily solved using any standard diagonalization package. To compute the first  $n$  band energies, one should truncate the matrix at  $N \gg n$  and take the lowest  $n$  eigenvalues; repeating for varying  $k$  will yield the first  $n$  band dispersions across the Brillouin zone. One can also get the coefficients  $c_{k+G}$  this way and reconstruct the periodic part of the Bloch

wavefunctions using (2.18).

Another helpful perspective is the so-called tight-binding limit. We can define spatially localized Wannier orbitals by Fourier transforming the Bloch waves in a given band. The  $n$ th Wannier orbital is then given by

$$w_n(x) = \frac{d}{2\pi} \int_{\text{BZ}} e^{-ikx} \psi_{nk}(x). \quad (2.20)$$

Note that the factor  $2\pi/d$  is the 1D Brillouin zone volume. A complete set for the  $n$ th band can be generated by translating  $w_n(x)$  to every site in the lattice. The Wannier orbitals are not uniquely defined due to the  $U(1)$  symmetry of the Bloch wavefunctions (i.e. we can define a smooth gauge  $f(k)$  that transforms  $\psi_{nk} \rightarrow e^{if(k)}\psi_{nk}$ ). The orbitals are orthonormal with respect to site and band index. To write down the tight-binding Hamiltonian, we simply write down the matrix elements of Hamiltonian in the Wannier basis. Because of the localization properties, it is often only necessary to consider overlap integrals between nearest neighbor sites; this is a better approximation for deeper lattices. In the 1D case, this gives the following Hamiltonian:

$$H_{\text{TB}} = \bar{\mathcal{E}}_n \sum_j c_j^\dagger c_j - J \sum_j [c_{j+1}^\dagger c_j + \text{h.c.}] \quad (2.21)$$

Here  $\bar{\mathcal{E}}_n$  is the average energy of the  $n$ th band and  $J$  is a tunneling energy given by

$$J = \int w^*(x-d) H w(x) dx. \quad (2.22)$$

The  $c_j^\dagger$  is a creation operator for a particle in the Wannier orbital at site  $j$ . The tight-binding Hamiltonian is diagonalized by a Fourier transform, yielding the following dis-

persion

$$\mathcal{E}_{\text{TB}}(k) = \bar{\mathcal{E}}_n - 2J \cos(kd). \quad (2.23)$$

This is the derivation of the famous statement that the bandwidth  $\Delta$  is given by  $4J$ .

## 2.3 Tilted Lattices

Given particles in a lattice, a natural question is to ask how those particles respond to the application of a force. For instance, we seek to characterize the conductivity properties of solids upon application of an applied voltage. In the  ${}^7\text{Li}$  experiment, we routinely apply a magnetic field gradient on the atoms in the direction of the lattice to observe Bloch oscillation transport. Here I will outline a number of theoretical perspectives on this problem. A thorough review of the relevant theory can be found in refs. [13, 14]. Realization of Bloch oscillations on the  ${}^7\text{Li}$  experiment can be found in ref [15].

The Hamiltonian we consider is given by

$$H = \frac{p^2}{2m} + V(x) - Fx. \quad (2.24)$$

Once again  $V(x)$  is spatially periodic, but the total potential along with the force is not. The simplest treatment is to make the following gauge transformation into the frame with linearly increasing momentum

$$U_{Ft} = \exp\left(i\frac{Ft}{\hbar}x\right). \quad (2.25)$$

This is a momentum shift operator which acts by  $p \rightarrow p + Ft$ . When making a generic

unitary transform, one should use the prescription

$$H \rightarrow U H U^\dagger + i\hbar (\partial_t U) U^\dagger \quad (2.26)$$

$$|\psi\rangle \rightarrow U |\psi\rangle \quad (2.27)$$

Our transformed Hamiltonian is then

$$H' = \frac{(p + Ft)^2}{2m} + V(x). \quad (2.28)$$

This Hamiltonian restores translational invariance so the steps to compute band structure can be reapplied. We see everything is the same except for the famous acceleration theorem:

$$k(t) = k_0 + \frac{F}{\hbar} t. \quad (2.29)$$

So if we initialize a Bloch state with quasimomentum  $k_0$ , its quasimomentum will evolve linearly (cyclically) in time. This is the phenomenon of Bloch oscillations. While historically Bloch oscillations were only possible to observe in momentum space, the light mass of lithium enables such oscillations to be visible in position space as well. A rigorous treatment is challenging, but the idea amounts to a group velocity being associated with the momentum space derivative of the  $n$ th band dispersion

$$v_n(k) = \frac{1}{\hbar} \frac{\partial \mathcal{E}_{nk}}{\partial k}. \quad (2.30)$$

Of course this is a periodic function in momentum space. Using the acceleration theorem,

one can then compute the following oscillatory position space trajectory

$$x(t) = \int_0^t v_n(k_0 + Ft'/\hbar) dt'. \quad (2.31)$$

For deep lattices, we can get an analytic expression by using the tight-binding dispersion (2.23). We find

$$x_{\text{TB}}(t) \sim \frac{2J}{F} \cos\left(\frac{2\pi}{T_B} t\right). \quad (2.32)$$

The amplitude of this oscillation defines the Wannier-Stark localization length

$$l_{\text{WS}} = \frac{2J}{F}. \quad (2.33)$$

Here we see the energy difference between adjacent lattice sites due to the force also defines the oscillation time scale called the Bloch period:

$$T_B = \frac{Fd}{2\pi\hbar}. \quad (2.34)$$

So far the analysis has been restricted to purely semiclassical single band effects. By inspection, the tilted lattice problem defined in (2.24) is a pathological Hamiltonian without a ground-state energy. In position space, a particle which is Wannier-Stark localized anywhere in the lattice (i.e. Bloch oscillating) can and necessarily will tunnel a toward negative infinite energy in the  $+x$  direction. In momentum space, every time the particle cycles around the Brillouin zone it crosses an avoided crossing at either  $k = 0$  or  $\pi/d$ . Only in the adiabatic limit where  $T_B \rightarrow \infty$  will the particle strictly remain in its original band. In this lowest order approximation, one can apply the Landau-Zener

tunneling formula to calculate the per cycle decay rate from band  $n$  to  $n + 1$ :

$$P(n \rightarrow n + 1) = \exp\left(-\frac{\pi^2 \Delta_{n,n+1}^2}{2\hbar\omega_B (|\mathcal{E}'_n| + |\mathcal{E}'_{n+1}|)}\right) \quad (2.35)$$

Here  $\mathcal{E}'$  denotes the slope of the bands with respect to dimensionless quasimomentum at the point of the bandgap in the limit that gap goes to 0:  $\Delta_{n,n+1} \rightarrow 0$ .

Alternatively, one can consider the so-called Wannier-Stark ladder of resonances. With respect to the tight-binding model in (2.21), the leading correction is to shift the on-site energies by  $Fd$  for each site:

$$H'_{\text{TB}} = \sum_j (\bar{\mathcal{E}}_n + Fdj) c_j^\dagger c_j - J \sum_j \left[ c_{j+1}^\dagger c_j + \text{h.c.} \right]. \quad (2.36)$$

This shift breaks the degeneracy of the orbitals and thus localizes the eigenstates of the Hamiltonian. Letting  $|j\rangle$  denote the  $j$ th Wannier orbital, one finds that (2.36) is diagonalized by the so-called Wannier-Stark resonance states

$$|\Psi_m\rangle = \sum_j J_{m-j} \left( \frac{l_{\text{WS}}}{d} \right) |j\rangle. \quad (2.37)$$

with the energy spectrum

$$E_{m,n} = \bar{E}_n + Fdm. \quad (2.38)$$

In the above  $J_{m-j}$  denotes a Bessel function of order  $m-j$ . We find that the amplitude of Bloch oscillations is indeed manifest in the localization of these resonance states. These are only resonances because they clearly do not contain any decay. The full spectrum

exists in the complex plane such that

$$\mathcal{E}_{m,n} = E_{m,n} - i\frac{\Gamma_n}{2}. \quad (2.39)$$

$\Gamma_n$  is the decay rate of a resonance state associated with the  $n$ th level Wannier orbitals. It can be approximated through (2.35); an exact calculation of the states and their decay rates is complicated and can be found in [14].

## 2.4 Floquet Theory

Here I review the relevant Floquet theory to establish the basis for discussion of periodically driven quantum systems. For references on Floquet theory for driven optical lattices, see [16, 17]. In terms of the mathematics, the Bloch's theorem encountered previously is in fact no more than a specific application of Floquet theory. Within the context of quantum mechanics, Floquet physics commonly refers to applications with time-periodic quantum systems such that the Hamiltonian obeys

$$H(t + T) = H(t). \quad (2.40)$$

In such cases we define the so-called Floquet Hamiltonian

$$H_F = H(t) - i\hbar\frac{\partial}{\partial t}. \quad (2.41)$$

The usual time-dependent Schrodinger equation is then

$$H_F |\psi(t)\rangle = 0. \quad (2.42)$$

Just as in the Bloch theorem case, the generalized stationary states obey

$$|\psi_n(t)\rangle = e^{-i\epsilon_n t} |u_n(t)\rangle, \quad |u_n(t+T)\rangle = |u_n(t)\rangle. \quad (2.43)$$

Here the  $\psi_n$  are the Floquet states and the  $u_n$  are referred to as Floquet modes which exist in the extended Hilbert space of square-integrable and time-periodic functions. The scalar product on this space is given by

$$\langle\langle u_n | u_m \rangle\rangle = \frac{1}{T} \int_0^T dt \langle u_n | u_m \rangle. \quad (2.44)$$

The eigenvalue problem can then be rewritten as

$$H_F |u_n(t)\rangle = \epsilon_n |u_n(t)\rangle. \quad (2.45)$$

An alternative formulation can be given in terms of the stroboscopic time-evolution operator for which

$$U(T) |u_n(t)\rangle = e^{-i\epsilon_n T} |u_n(t)\rangle. \quad (2.46)$$

The  $\epsilon_n$  are called the quasienergies. Letting  $\omega = 2\pi/T$  be the drive frequency, this last eigenvalue problem makes it clear the quasienergies are only uniquely defined up to a “Brillouin zone” of width  $\hbar\omega$ . A general state can be decomposed as

$$|\psi(t)\rangle = \sum_n c_n e^{-i\epsilon_n t} |u_n(t)\rangle. \quad (2.47)$$

The power of this technique is that the evolution of an explicitly time-dependent problem (which is typically extremely challenging) can then be completely solved by finding time-

independent coefficients  $c_n$ . This supposes one has knowledge of the Floquet modes and quasienergies.

The primary application of this in the Weld lab so far has been for computing so-called Floquet-Bloch bands of an amplitude modulated lattice described by

$$H = \frac{p^2}{2m} + \frac{V_0}{2} [1 + \alpha \sin(\omega t)] \cos(2k_L x). \quad (2.48)$$

This is discussed in ref. [6], and I outline it here for completeness. What one does is numerically calculate  $U(T)$  by Trotterizing the time-evolution operator (breaking up the time-evolution into a bunch of discrete steps  $\Delta t$ ) and writing down the Hamiltonian at each step explicitly in a single basis. The Hamiltonian can be written for a given quasi-momentum  $k$  in momentum space using the strategy in section 2.2. This Hamiltonian will be slightly different at each time step due to the varying lattice depth, and multiplying together a bunch of matrix exponentials  $\exp(-iH(V_0(t_j))\Delta/\hbar)$  over a drive period produces  $U_k(T)$ . By exact diagonalization, one can get the quasienergies  $\epsilon_{nk}$  via (2.46). This should then be repeated for varying  $k$ , and further to compute clean Floquet-Bloch bands one needs to project the states onto the static Bloch states. For weak drive amplitudes  $\alpha$ , one generally finds only significant mixing between undriven states near resonance points where  $\hbar\omega \approx \mathcal{E}_{n,k} - \mathcal{E}_{m,k}$  for the undriven bands  $\mathcal{E}$ ; at stronger drives we can get higher-order processes with coupling of states separated by  $j\hbar\omega$  for different integers  $j$ . At these points, the bands cross in the dressed state picture and an avoided crossing opens up. In fact, Floquet theory in this context is essentially the same as the dressed state picture in atomic physics where the procedure of folding energy levels into a single Brillouin zone corresponds to dressing states with different numbers of photons. Many analytic approximate expansions exist based on this notion of different order photon processes and could be useful for new applications of Floquet theory in the group.

Given the discussion in section 2.3, it is natural to ask how Bloch oscillations are affected in these Floquet-Bloch bands. In practice, we are often in the regime where the gap that opens up between Floquet-Bloch bands is much larger than the energy scale of the forcing potential. In these cases, we can apply semiclassical dynamics to the numerically calculated Floquet-Bloch bands to excellent approximation; see ref [18] for examples. This can alternatively be understood as rapid adiabatic passage between bands, where the Bloch oscillation takes the role of what is traditionally a detuning sweep. By weakening the coupling, one must then consider tunneling events between Floquet-Bloch bands, and this will be the focus of the next section.

# Chapter 3

## Engineering Tunable

## Floquet-Bloch-Zener Decay

Decay is a ubiquitous phenomena in quantum physics. For instance, excited electronic states in an atom are in actuality only meta-stable resonances with a finite lifetime  $\tau$  or alternatively a decay rate  $\Gamma = 1/\tau$ . On fairly general grounds, we expect this decay parameter to describe a generic exponential form  $e^{-\Gamma t}$ . For cold atoms in an optical lattice, we have already encountered one such instance of a decay process: the Wannier-Stark problem. However, the exponential decay is only an approximation (a very good one for sure) and in fact, the study of the Wannier-Stark ladder with the cold atom platform has played a major role in confirming our understanding of quantum mechanical decay processes beyond this approximation. One goal of the  $^7\text{Li}$  experiment is to explore and engineer non-Markovian decay dynamics by utilizing Bloch decay in tunable Floquet band structures. In this chapter I overview some basic theoretical grounds for non-exponential decay and progress made toward realizing tunable tunneling in the Floquet band structure.

The arXiv preprint version of this work is displayed in Appendix D [19].

### 3.1 Nonexponential Quantum Decay

We begin by giving an discussing nonexponential behavior in quantum systems at a high level. An overview of the topic can be found in a supplementary section of the popular textbook Sakurai [20]. To the best of my knowledge, the first account of nonexponential quantum decay was given by Khalfin in 1958 [21]. Other useful theoretical discussions and reviews can be found in [22, 23, 24].

To understand nonexponential violations, it is useful to first discuss perspectives on why decay should be exponential in the first place. From a classical perspective, an exponential law accompanies any process occurring at a constant rate (or probability per discrete time interval). In such cases, the rate of change of a given parameter scales with the magnitude of that parameter:

$$\frac{dN}{dt} \sim \lambda N. \quad (3.1)$$

Such an equation is solved generically by the exponential form. In classical probability theory, we associate such processes with the memoryless or Markov property since the decay at any given instance only depends on the current configuration (i.e. the instantaneous value of the parameter) and not at all on the history of the evolution. The simplest model to understand quantum decay is then to consider a quantum wavefunction localized in a semi-infinite box (infinite wall on one side and barrier of variable width and height on the other). Essentially the particle will bounce back and forth between the walls if it has less energy than the barrier height, and every bounce there will be a finite transmission/tunneling/decay probability out of the box. Because energy is conserved, this probability is constant in time and thus the remaining density inside the box must decay exponentially.

A generic isolated quantum system is described by a wavefunction which can be expanded in a basis of true eigenstates. Here we take energy to be continuous for simplicity:

$$|\psi(t)\rangle = \int_{-\infty}^{\infty} c(E)e^{-iEt/\hbar} |E\rangle dE. \quad (3.2)$$

We define the survival amplitude as the overlap with the initial state

$$A(t) = |\langle\psi_0|\psi(t)\rangle|^2 = \int_{-\infty}^{\infty} |c(E)|^2 e^{-iEt/\hbar} dE. \quad (3.3)$$

The measurable survival probability  $P(t)$  is then defined as the absolute square amplitude  $|A(t)|^2$ . Clearly, the survival amplitude is simply the Fourier transform of the energy distribution of the initial state. If one consider a true stationary state  $|c(E)|^2 = \delta(E - E_0)$ , we indeed find  $P(t) = 1$ . For a quasistationary resonance however,  $c(E)$  will have a finite width and thus the survival probability must decay. Metastable states often exhibit a Breit-Wigner/Lorentzian lineshape:

$$|c(E)|^2 = \frac{1}{2\pi} \frac{\Gamma}{(E - E_0)^2 + \Gamma^2/4}. \quad (3.4)$$

Indeed the Fourier transform of a Lorentzian is exponential and so we find

$$P(t) = |A(t)|^2 = e^{-\Gamma t/\hbar}. \quad (3.5)$$

This can be confirmed explicitly by contour integration over a semicircle in the lower half plane. Given how common the Lorentzian lineshape is, this establishes fairly general grounds for expecting exponential decay across many quantum mechanical processes.

Now we are prepared to understand nonexponential violations. In general, one finds deviations both at short and long times. The short-time deviations result from the fact

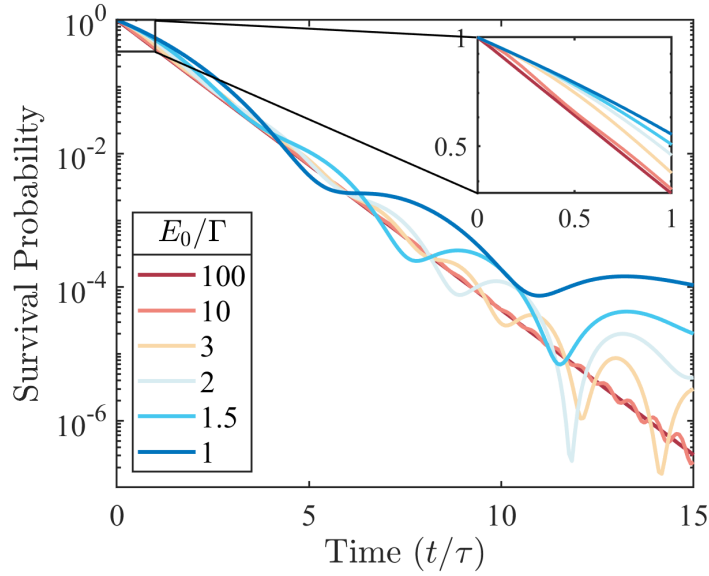


Figure 3.1: Survival probability for the truncated Breit-Wigner distribution for varying ratios between the resonance energy  $E_0$  and decay energy  $\Gamma$ . When the truncation/ground state energy (taken to be  $E = 0$ ) is located within 1-2 linewidths of the resonance, strong deviations from pure exponential decay can be observed at all times, with slower decay at very late times.

that the rate of change of the survival probability must initially be 0, and thus the leading order behavior of the probability decay is only quadratic, precluding exponential behavior. Physically, this is because at short times the energy structure of the states is not yet resolved. This was first observed in Raizen’s 1997 cold atom Wannier-Stark experiments [25], and a thorough decay calculation for the problem beyond the two-level Landau Zener formalism can be found in [26].

Our particular goal is to focus more on long-time corrections which haven’t been observed until more recently [27, 28]. These long-time violations are understood by the simple argument that real quantum systems exhibit a ground state. This ground state should have finite energy, and thus in (3.3) one must bound the integral from below. Alternatively, we should only consider (3.4) as approximate. If the ground states is located at an energy where  $|c(E)|^2$  is still reasonably large, the subsequent corrections to the survival probability (3.5) may also be observable. In particular, one can use the

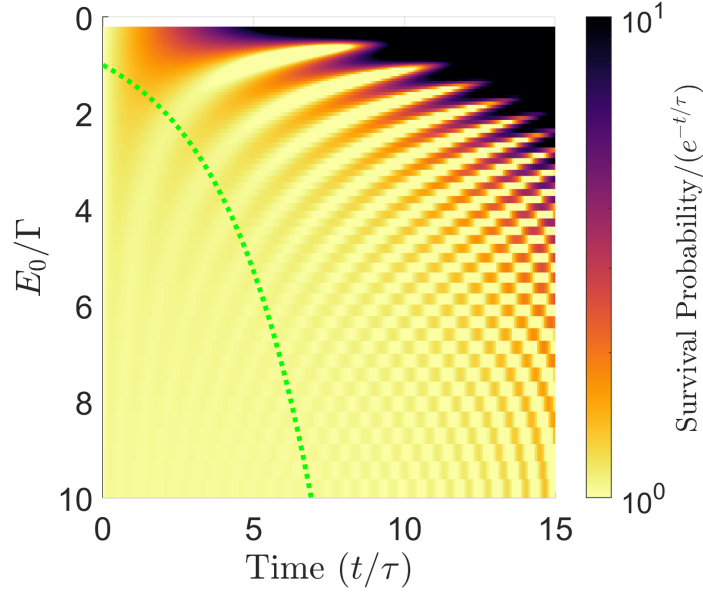


Figure 3.2: Heat map of the survival probability over time normalized to an exponential decay for varying  $E_0/\Gamma$ . The green dashed line indicates the predicted onset of long-time decay as given by (3.7), and the darker regions indicate where strong deviations are actually observed. If one can get the ratio  $E_0/\Gamma$  of order unity, the onset is almost immediate and is experimentally feasible to observe.

Paley-Wiener theorem to eventually show (see [21] for details) that the decay must be slower than exponential

$$P(t) \geq \exp(-\gamma|t|^q), \quad \gamma > 0, \quad q < 1. \quad (3.6)$$

This result states that the long-time decay behavior must be slower than exponential. One can confirm this by numerical computation of the integral in (3.3) with the lower bound set to 0 and assuming a distribution of (3.4). This is shown in Fig. 3.1, where oscillations are seen to emerge before indeed leveling off to slower than exponential at late times. (3.6) does not tell us anything about when such behavior should occur. Defining  $\tau = \hbar/\Gamma$ , an approximate criterion given in [22] for the timescale  $\tau_L$  where the long-time

behavior sets in is given by

$$\tau_L \sim 3\tau \ln\left(\frac{E_0}{\Gamma}\right). \quad (3.7)$$

As seen in Figure 3.2, this equation follows reasonably well at low  $E_0/\Gamma$  but isn't so useful at larger ratios; anyway, for large ratios the corrections are so exponentially small that experimental observation is unfeasible in most cases. Ultimately, this analysis shows that the critical parameter for observing late time non-Markovian dynamics requires achieving  $E_0/\Gamma$  around unity. The calculations presented in this section are done using Matlab's standard numerical integration package.

## 3.2 Tunable Decay in Driven Lattices

As discussed in section 2.3, particles in a forced lattice feature decay processes out of the band in which the particles are Bloch oscillating. At lowest order, Landau-Zener tunneling events happen once per Bloch period at the inversion symmetric points of the Brillouin zone  $k = 0, \pi/a$ . When the optical lattice is amplitude modulated, new Floquet band gaps can open up symmetrically away from these points. From generic knowledge of Rabi oscillations, these gaps are carefully tunable through the amplitude modulation parameter, providing a new potential degree of control for decay experiments. Here I will discuss experiments demonstrating this tunable Bloch-Zener decay in Floquet bands. Ultimately the goal would be to apply these techniques for realizing the physics outlined in section 3.1.

Since much of the discussion up to this point has been theoretical, I will first describe the details of our typical modulated lattice experiment since the same essential ingredients are used in a variety of different contexts. We begin with a BEC of about  $10^5$   $^7\text{Li}$

atoms captured in a crossed optical dipole trap. The atoms are in the  $|F = 1, m_F = 1\rangle$  state with the magnetic field along the  $z$  direction set by a pair of Helmholtz coils so that the scattering length is  $a_S = 240a_0$ . The dipole beams are in the  $x - y$  plane (however not perpendicular) with gravity in the  $z$  direction. I don't have a recent accurate measurement of the trap frequency, though I believe the average to be about 40 Hz; we typically observe Thomas-Fermi radii of about 25-30  $\mu\text{m}$ . At this point, for non-interacting experiments we ramp the magnetic field by about 200 Gauss in 100 ms to reach a regime of negligible interparticle interactions. The lattice is then adiabatically ramped on to the desired depth of  $V_0$  in 100 ms, and roughly one achieves a  $k = 0$  1D Bloch state with Gaussian envelope along the lattice direction; for the most part we do not seem to saturate the expected momentum width bound based on the uncertainty principle given the imaged size of the BEC. We typically do not observe any strong transverse dynamics for trapped lattice experiments. At this point the optical dipole traps are snapped off and the atoms feel a force along the axial direction from the local magnetic gradient produced by another set of magnetic field generating coils. This magnetic potential is close to harmonic, and the relevance of the field curvature varies from experiment to experiment. In this chapter, I will assume a uniform force to explain the dynamics. As the dipole traps are snapped off at  $t = 0$ , we also begin sinusoidal modulation of the lattice depth. The system is then well-described by the 1D Hamiltonian

$$H = \frac{p^2}{2m} + \frac{V_0}{2} [1 + \alpha \sin(\omega t)] \cos(2k_L x) - Fx. \quad (3.8)$$

The lattice lasers are  $\lambda = 1064$  nm so that  $k_L = 2\pi/\lambda$ . Of course  $m = 7$  amu.  $V_0$  and  $\alpha$  are controlled by laser intensity and  $F$  can be set by changing the current in the push coils. The typical energy scale of the lattice is given in recoils of the 1064 laser  $E_R = \hbar^2 k_L^2 / 2m$ . The recoil frequency is  $\omega_R = E_R / \hbar \approx 25.17$  kHz. Typically we take the

lattice depth to be around  $5 E_R$  so position space dynamics are observable. The forces we can apply typically correspond to Bloch periods  $T_B$  in the range of 15-20 ms. Thus the energy scale of the Stark ladder is much smaller than any band gap and single-band Bloch oscillations are a good approximation in the absence of modulation; in the presence of a weak drive, we expect that Bloch oscillations also dictate dynamics away from any drive resonances.

The modulation however sets a new energy scale by opening up a band gap. We consider a drive frequency  $\omega$  such that we are near resonance between the lowest two bands  $\mathcal{E}_{2,k} - \mathcal{E}_{1,k}$  away from the Brillouin zone center/edge; care has to be taken to avoid coupling to higher bands but I will assume this to be the case for the analysis. Because the modulation is quasimomentum conserving, at any stage in the system evolution we can model the dynamics in a two-level formalism; see Dan Steck's online quantum optics notes for a review [29]. In the rotating-wave approximation, we have the matrix

$$H_2(k) = \begin{pmatrix} \mathcal{E}_{2,k} & \frac{\hbar\Omega(k)}{2}e^{-i\omega t} \\ \frac{\hbar\Omega(k)}{2}e^{i\omega t} & \mathcal{E}_{1,k} \end{pmatrix} \quad (3.9)$$

Here the Rabi frequency is given by

$$\Omega(k) = \frac{\alpha V_0}{\hbar} \int_0^d u_{1,k}^*(x)u_{2,k}(x) \sin^2(k_L x) dx. \quad (3.10)$$

Here I switched from  $\cos(2k_L x)/2 \rightarrow \sin^2(k_L x)$  so that  $\Omega$  is positive for bands with the same parity; the absolute value which is the only thing that matters for the gap size is the same. These Rabi frequencies are always real. We dress the excited state by a drive

photon to get the effective Hamiltonian

$$\tilde{H}_2(k) = \hbar \begin{pmatrix} -\delta(k) & \frac{\Omega(k)}{2} \\ \frac{\Omega(k)}{2} & 0 \end{pmatrix} \quad (3.11)$$

with  $\delta(k) = \omega - (\mathcal{E}_{2,k} - \mathcal{E}_{1,k})/\hbar$ . To apply the Landau-Zener formalism, the band gap  $\Delta$  should be defined near the resonant quasimomentum  $k_0$  that obeys  $\delta(k_0) = 0$ . For this we have

$$\Delta_{1,2} = \hbar|\Omega(k_0)|. \quad (3.12)$$

The overlap integral is typically order  $\sim 0.1$ , and so the Floquet band gap will be order  $\alpha V_0/10$ , which for weak modulations  $\alpha$  on the level of a few percent brings it to a comparable scale as the forcing potential. At a practical level for the  ${}^7\text{Li}$  experiment, this is an important capability as the push coils simply don't have the capacity to get to  $E_R$  level couplings, preventing the study of static Bloch-Zener transitions (without going to exceedingly small lattice depths which is not ideal). One could eventually imagine implementing accelerating lattices to resolve this (which also has further potential applications beyond this), but already we see that Floquet engineering enables our experiment to access decay physics.

The simple analysis here suggests that we can fine-tune the direct band gap between any two bands in an optical lattice at any quasimomentum (except for the Brillouin zone edge and center where the matrix element vanishes for opposite parity bands due to the perturbation being parity preserving). I explicitly used labels for bands 1 and 2 here for concreteness, but this analysis follows for any pair of bands. Returning to the Landau-Zener formula (2.35), we can write down an explicit expression for the tunneling

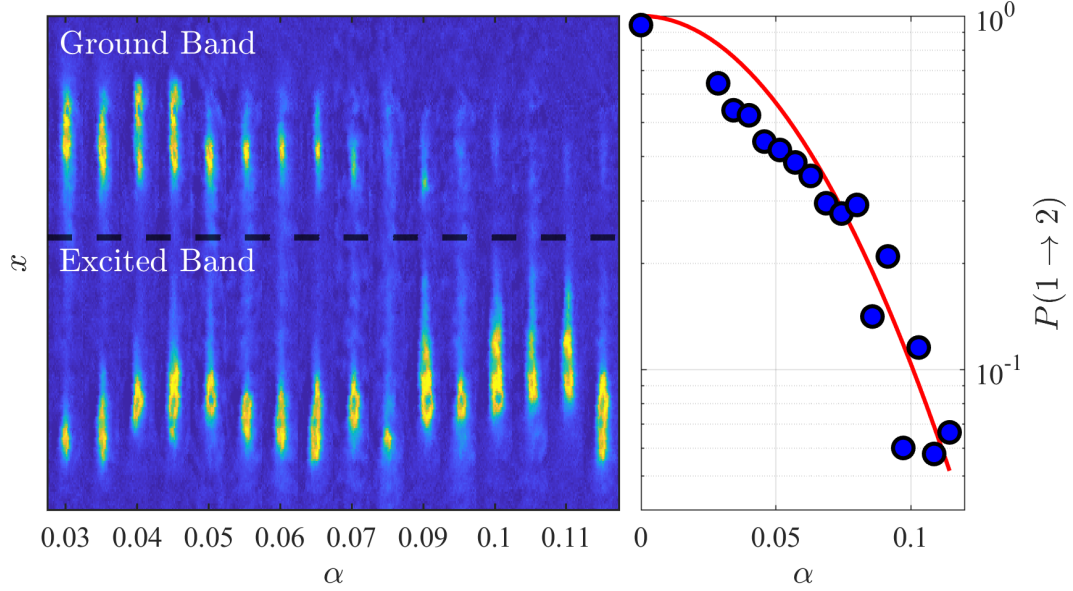


Figure 3.3: Measurement of Landau-Zener band tunneling with position-space Floquet-Bloch oscillations. Images are taken after half a Bloch period with drive resonantly coupling the lowest two bands; the relative population in the ground band (above dashed line) is plotted as blue circles in the right panel. Here  $V_0 = 3.5E_R$ ,  $T_B = 27.8$  ms and  $\omega = 2\pi \times 55$  kHz. Red theory line is based on equation (3.13) with no fit parameters.

probability during each pass of the Bloch oscillation:

$$P(1 \rightarrow 2) = \exp\left(-\frac{\pi^2 \alpha^2 V_0^2 I^2}{2\hbar\omega_B(|\mathcal{E}'_1| + |\mathcal{E}'_2|)}\right). \quad (3.13)$$

Here  $I$  denotes the integral in (3.10). One difference to note in the application of this formula as compared to the static lattice case is that the energies here are taken in the limit of  $\alpha \rightarrow 0$  with  $V_0$  held constant, so the  $\mathcal{E}$  here are actual band energies as opposed to free particle energies (recall there we took the limit as the static band gap vanished which is equivalent to  $V_0 \rightarrow 0$ ). So in addition to having linear control over Floquet band gaps, we expect to be able to exponentially tune tunneling rates over orders of magnitude in the modified Floquet Wannier-Stark problem.

While this dressed state analysis assists in getting an analytic form for the transition

probability, it is less helpful in visualizing how an experiment could measure this effect. However, we know the physics away from the transition points is dominated by semiclassical dynamics. The slope of the bands gives the velocity, and thus position-space Bloch oscillations map out the Floquet bands themselves. Because of  ${}^7\text{Li}$ 's light mass, after the tunneling event occurs the band populations spatially separate and can be read out. Thus simply allowing the BEC to evolve for half a Bloch period under the Hamiltonian (3.8), we are able to trivially probe band structure tunneling in real space. This is demonstrated in Fig. 3.3 where we perform the experiment at varying modulation index  $\alpha$ . The observable in the right panel matching to (3.13) is the fraction of the population remaining in the ground band. This is a subtle difference with respect to the static lattice case as the tunneling event across the Floquet-Bloch gap is from a single static Bloch band back to itself and adiabatic passage corresponds to transfer between static bands. In the undriven case, it is exactly opposite where tunneling corresponds to static Bloch band transfer. This figure demonstrates the tremendous tunability of Landau-Zener decay in Floquet-Bloch bands, which we hope will be the basis for realizing non-exponential late time decay with cold atoms as well as atom interferometry in modulated lattices (see section A.2).

### 3.3 Toward Nonexponential Floquet-Bloch Decay

Historically, one of the primary hurdles in observing late time violations has been a lack of tunability in decay parameters for common experimental platforms such as radioactive nuclei [30]. The decay control provided by Floquet engineering serves as a useful technique to overcoming these challenges. However, there is another challenge that warrants serious consideration in relation to realization within the  ${}^7\text{Li}$  experiment. The argument given for late time violations in section 3.1 is the existence of a ground state

at an energy relevant to the linewidth of the metastable resonance. In a Wannier-Stark ladder model however, the ground-state is in some sense ill-defined as one can always translate over a lattice site to reduce the energy. In the real world of course the ladder will not extend infinitely, but for an accelerating optical lattice the ground state is likely too far away to make significant corrections.

In the  ${}^7\text{Li}$  experiment there is a true ground state, namely the forcing potential is actually harmonic and features a minimum. However, as seen in previous explorations of long-range transport on this apparatus [18], the atoms do not decay to this minimum but simply oscillate back and forth between two symmetric positions across this harmonic potential. Conceptualizing how the decay processes work out in detail for this experiment is something that remains a task for future work. For instance, one simple solution that has been discussed is adding in a spatially local resonant light beam which removes atoms that have decayed (tunneled to higher bands) from the lattice. Does this lead to any complications? Are you able to change the effective ground state energy if you put the resonant beam at different points along the harmonic trap?

# Chapter 4

## Transport Controlled by Semiclassical Poincaré Topology

Understanding the transport dynamics of particles in periodic potentials is a fundamental question of condensed matter physics. Transport under a uniform applied force is of course a standard protocol, and for clean periodic potentials the phenomena of Bloch oscillations is now deeply understood. Over the past decade or so, the interplay between Bloch oscillations and an external drive has unveiled a whole host of novel transport protocols. In this chapter, I'll discuss new interpretations of driven Bloch oscillation dynamics through the topological properties of Poincaré orbits in the semiclassical phase space.

The arXiv preprint version of this work is displayed in Appendix E [31].

## 4.1 Dynamic Localization and Super Bloch Dynamics

Much interest has been put into 1D force modulated lattices at low frequencies where the physics is single-band. This regime has the benefit of being simple and tractable while also possessing a wealth of rich behaviors. Experiments include observation of coherent delocalization [32, 33], photon-assisted tunneling [34], Wannier-Stark ladder resonances [35] and super Bloch oscillations [36]. The theoretical literature is also rich [37, 38, 39, 40, 41]. For a review of modulated lattices that covers all of these experiments and more, see [17]. The main concept of interest from these works to our experiment is that of dynamic localization. This term refers to the rescaling of a characteristic scale in the problem due to the drive, and in this case refers to renormalization of the Wannier-Stark localization length (2.33) due to the force modulation.

There are subtleties in the calculation but the essential idea is as follows. Suppose we consider noninteracting atoms in an optical lattice and subject them to a time-periodic force with zero average:

$$F(t) = F(t + T), \quad \frac{1}{T} \int_0^T F(\tau) d\tau = 0. \quad (4.1)$$

Once again we consider a regime where single-band approximation is valid. Using a similar unitary transformation from section 2.3 to derive the acceleration theorem, we can make the Hamiltonian periodic in both time and space. This allows us to then apply both Bloch and Floquet theory, i.e. we have spatiotemporal Bloch waves with a time-averaged band. This band dispersion is given by

$$\epsilon(k) = \frac{1}{T} \int_0^T \mathcal{E}(q_k(t)) dt \quad (4.2)$$

where the acceleration theorem implies

$$q_k(t) = k + \frac{1}{\hbar} \int_0^t F(\tau) d\tau. \quad (4.3)$$

In tight-binding, the dispersion is  $\mathcal{E}(q) = -2J \cos(qd)$ , and so for sinusoidal modulation at frequency  $\omega$  and amplitude  $F$ , we get the analytic expression

$$\epsilon(k) = -2J \mathcal{J}_0 \left( \frac{Fd}{\hbar\omega} \right) \cos(kd). \quad (4.4)$$

Here  $\mathcal{J}_0$  is a zero order Bessel's function which rescales the tunneling  $J$ . For certain values of the force amplitude with respect to the drive frequency, the band completely collapses and one has strong dynamical suppression of transport.

When one adds in an additional static force (i.e.  $\int_0^T F(t) dt \neq 0$ ), one has to be a bit more careful but can arrive at similar results showing rescaled tunnelings. In addition, there is a new frequency scale set in the problem of the ladder spacing and the dynamics end up strongly depending on the detuning of the modulation with respect to this frequency. In the case of small detuning  $\delta\omega$  (here  $\delta$  denotes a small number), it was shown that for an initial quasimomentum  $k$  the center of mass evolution is given by [40]

$$x(t) \approx -\frac{Jd}{\delta\omega} \mathcal{J}_1 \left( \frac{Fd}{\hbar\omega} \right) [\sin(K_F + \delta\omega t) - \sin K_F], \quad K_F = kd + \frac{Fd}{\hbar\omega} \cos \phi - \phi. \quad (4.5)$$

Here  $\phi$  is the phase of the force drive. This clearly shows that there are position space oscillations at the detuning  $\delta\omega$  with a localization length which is rescaled not only by a Bessel's function but also by the inverse detuning. On resonance, we have a divergent tunneling which corresponds to the fact that drive photons resonantly couple the entire Wannier-Stark ladder. In this case, one finds directed linear transport that depends on the phase of the drive relative to the initial quasimomentum.

To understand this visually, one can consider the micromotion during a drive period. First I'll consider the case of resonant driving. On resonance for a sinusoidal forcing about a non-zero mean, the Bloch period is exactly equal to the drive period and so we can figure out the average dynamics by considering a single period. Suppose we start at  $k = 0$ . For a sine function drive, then traversing the positive side of the group velocity from  $k = 0$  to  $k = \pi$  is done more quickly than at the static force background, and so we get less transport. On the other hand, the quasimomentum goes across the negative side of the group velocity from  $k = \pi/a$  to  $k = 0$  over a longer time frame and thus we get more transport in this direction. The net effect is then transport in the negative  $x$  direction over a single period, and this leads to an average nonzero group velocity. If one flips the drive phase by  $\pi$  (or alternatively begins the Bloch oscillation at  $k = \pi/a$ ), the argument just flips and transport is directed in the other direction. For in between phases, the average velocity will smoothly interpolate between these two extremes. In the next section, I will derive a simple result for the cycle-averaged velocity for a weak amplitude modulation, but the result holds similar intuition for the force modulation case described here.

If one is at nonzero detuning, the quasimomentum does not exactly map back to itself. However for small detunings such that the change in quasimomentum per drive period is small compared to the width of the Brillouin zone, one can use a perturbative argument. Each drive cycle there is a net transport one way or the other as in the resonant case, and the effect of the detuning is to slightly modify the phase (starting quasimomentum) for the next cycle. Each cycle there will be some net transport dictated by the current phase, and then since the Bloch cycle doesn't complete exactly due to the detuning the phase is modified slightly. Iterating this idea repeatedly leads one to conclude that the stroboscopic dynamics are position space oscillations across a Brillouin phase-space cylinder. This schematic argument qualitatively derives much of the super Bloch behavior

measured in ref. [36], and will be expanded upon and visualized in the next section.

## 4.2 Poincaré Topology and Bloch Transport under Slow Amplitude Modulation

A natural question to ask is whether slow lattice amplitude modulation leads to similar dynamics as force modulation. The super Bloch oscillations of the last section could be understood as a rescaling of the Wannier-Stark localization length by modulating one of its parameters, namely  $1/F$ . The localization length also depends on  $J$ , and so it seems possible that lattice depth modulation could produce similar effects. Indeed tuning effective tunneling with amplitude modulation was demonstrated in [42]; this experiment is also described by (3.8) in the large  $V_0$  regime for both negligible static tunneling and interband coupling. In this section we consider a similar experimental setup, but with two key differences: non-negligible tunneling/spatial transport in the absence of the drive and a significant harmonic curvature to the external forcing potential. This combination of features significantly modifies the transport dynamics from any of the previously mentioned experiments, which we ultimately describe through an analysis of semiclassical orbits in phase space. Specifically, the parameters considered for the data in the rest of the chapter are  $V_0 = 4.3E_R$ ,  $\omega = 2\pi \times 53.56$  Hz,  $\alpha = 0.24$  and  $T_B = 16.75$  ms.

The scheme for directed transport is shown in figure 4.1. Since the force is weak, at every instance in time we can calculate a band dispersion and corresponding group velocity which describes the instantaneous dynamics. For a resonant drive with respect to the Bloch frequency, it is then possible to compute an effective band dispersion and group velocity which dictates the transport every period. From the group velocity, it is

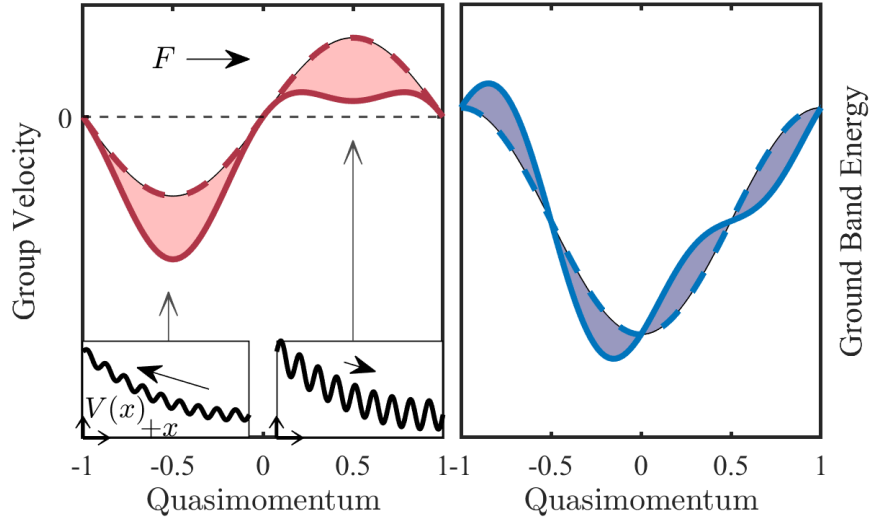


Figure 4.1: Schematic of directed transport in amplitude modulated optical lattices driven on Wannier-Stark resonance. Treating the force semiclassically, the atoms see an effective modulated band structure due to time variation of the lattice (right). Equivalently, the atoms experience an asymmetric group velocity across the Brillouin zone amenable to directed transport.

easy to then integrate over the Brillouin zone to obtain the average group velocity which will be nonzero except when the drive and Bloch oscillation are exactly  $\pi/2$  out of phase (in the sense established in the previous section).

In fact one can write down an analytic expression for the transport using some approximations. Assuming a small lattice depth modulation, we can expand the tunneling modulation to linear order as

$$J[V(t)] \approx J(V_0) [1 - \alpha_0 \sin(\omega t + \varphi)]. \quad (4.6)$$

Here  $V_0$  is the static lattice depth and  $J$  depends on time only parametrically through the instantaneous lattice depth; the scaled modulation index  $\alpha_0 = \alpha |J'(V_0)| V_0 / J(V_0)$  can be computed explicitly using Mathieu function relations for the band edges [16]. In the

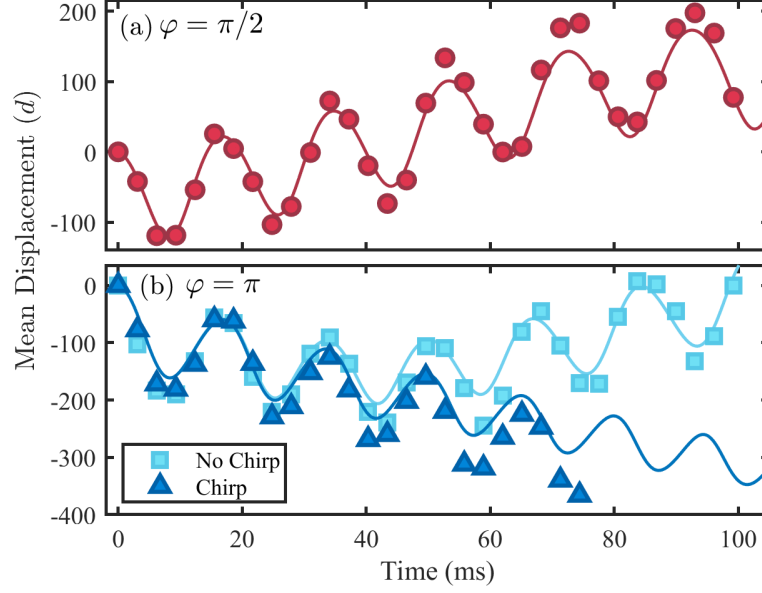


Figure 4.2: Center of mass trajectories for slow amplitude modulation under a magnetic force gradient for two drive phases. Theory is based on semiclassical equations of motion. Additionally, a drive frequency chirp is shown to be able to extend the transport range against the force gradient (up the magnetic potential).

tight-binding regime, the group velocity can be taken as

$$v_g(t) = \frac{2J[V(t)]d}{\hbar} \sin(k(t)d). \quad (4.7)$$

Integrating this expression for the resonant driving case  $\omega_B = \omega$  where  $k(t) = (\omega t + \pi)/d$  (here the  $\pi$  is just to be consistent with experimental protocol) and using the small modulation tunneling approximation, we compute a cycle-averaged group velocity of

$$\bar{v}_g = \frac{\alpha_0 v_0}{2} \cos \varphi, \quad v_0 = \frac{2J(V_0)d}{\hbar}. \quad (4.8)$$

Indeed the analysis shows a group velocity which oscillates appropriately with respect to the phase between drive and Bloch oscillations.

In fact this analysis is correct in producing the center-of-mass dynamics of the Hamiltonian (3.8) in the stated parameter regime, and it qualitatively explains some of the

dynamics observed in the experiment. Namely we do indeed see the ability to direct slow, stroboscopic transport by varying the drive phase. However, figure 4.2 reveals that it is quantitatively wrong. At  $\varphi = \pi/2$  where (4.8) predicts zero net transport, we experimentally observe ideal pumping along the direction of the force. On the other hand at  $\varphi = \pi$  which should yield maximal transport against the force, we observe a rapid trajectory reversal after just a few cycles. The reason for this deviation from the analytic expression resides in the fact that our experimental system features a harmonic potential rather than a constant force. Moreover the light mass of lithium means that the amplitude of Bloch oscillations can be over many lattice sites even in the tight-binding regime, so the local force can significantly change without violating semiclassical assumptions. Thus our experiment features not only an externally imposed tunneling modulation but also a parametric force modulation via the position space micromotion over a Bloch/drive period. It should be noted that we were successfully able to delay the turning around by applying a frequency chirp to the modulation, enabling further pumping against a force gradient. This is shown in the chirp data of figure 4.2. This can be roughly understood as compensating for the average change in force per pumping cycle.

At this point it is simplest to model the dynamics numerically by integrating differential equations. Explicitly, the Hamiltonian we consider is given by

$$H = \frac{p^2}{2m} + \frac{V_0}{2} [1 + \alpha \sin(\omega t + \varphi)] \cos(2k_L x) + \frac{1}{2} m \omega_0^2 x^2 - Fx. \quad (4.9)$$

Here  $\omega_0 = 2\pi \times 15.5$  Hz is the magnetic harmonic potential frequency. The semiclassical dynamics are then described by

$$\dot{x} = \frac{2J [V_0(1 + \alpha \sin(\omega t + \varphi))] d}{\hbar} \sin(kd), \quad \dot{k} = F - m\omega_0^2 x. \quad (4.10)$$

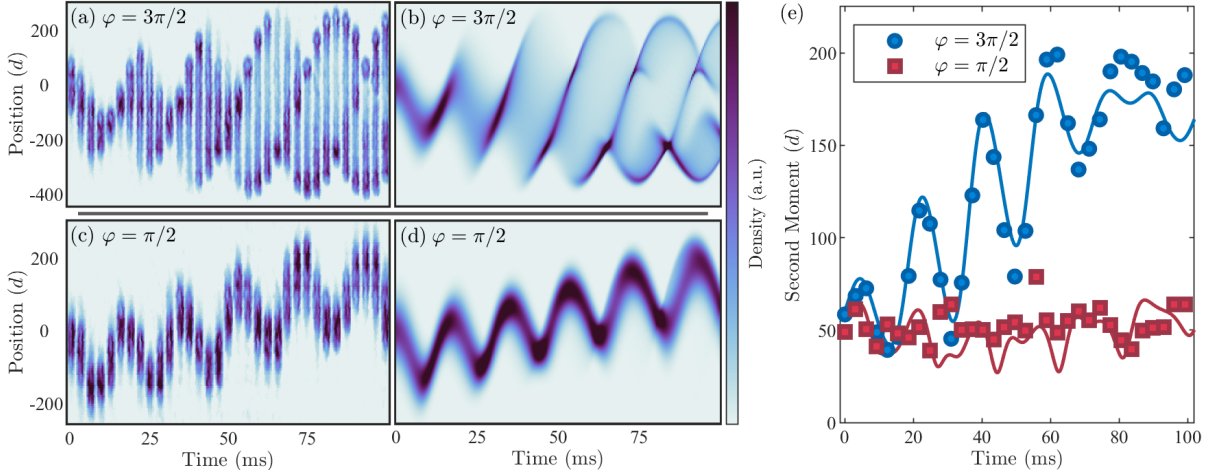


Figure 4.3: (a) and (c) Time traces of the cloud evolution for drive phases of  $\varphi = \pi/2, 3\pi/2$ . (b) and (d) Corresponding semiclassical simulations. The  $\pi/2$  drive yields stable wavepacket transport with minimal deviations in the spatial width. At  $3\pi/2$ , we instead observe a rapid oscillation dephasing and significant expansion after just a couple drive cycles. The standard deviation of the distributions is plotted in (e), with fairly good agreement between experiment and theory.

For simulations, we approximate  $J = 4\Delta$  and calculate  $\Delta$  numerically from the instantaneous lattice depth. The lines in figure 4.2 are computed using this simulation technique and demonstrate excellent agreement.

A phenomenon we did not anticipate was the observation of strong asymmetry in the spatial moment dynamics with respect to drive phase. As shown in figure 4.3, the opposite phases of  $\pi/2$  and  $3\pi/2$  yield drastically different dynamics. In the first case, the wavepacket stays compact and the most prominent short time behavior is simply stroboscopic directed transport. At the opposite phase, there is no center-of-mass transport at all; instead the cloud rapidly broadens and largely enters a bimodal distribution with some interesting oscillatory structure. While the semiclassical equations (4.10) are typically intended to only describe the center-of-mass dynamics for an appropriately constructed wavepacket, here we find that treating them as essentially Hamilton's equations leads to a quantitatively correct description of the spatial moment dynamics. We sample a Gaussian weighted ensemble of initial conditions to simulate the evolution of a classical

phase-space density under the equations (4.10), and then construct a density which is plotted in panels (b) and (d) of figure 4.3. We find that it almost exactly reproduces the measured quantum squared wavefunction density visually (in both cases!), and quantitatively it closely matches the observed spatial spread behavior. We take the parameters of the Gaussian weighting to be  $\sigma_x = 60d$  and  $\sigma_k = 0.1k_L$ ; the  $\sigma_k$  is larger than one would expect for BEC, but this is because we believe there to be inhomogeneous forces broadening the distribution during the adiabatic lattice ramping.

While the theory works nicely here for modeling purposes, it is rather unsatisfying in providing a deeper, physical understanding for why the curvature produces such a drastic changes. For this, we return to the discussion at the outset of this chapter and investigate the underlying semiclassical phase space structure. Namely, we can use the Poincaré section technique to understand the stroboscopic properties of the system. I will refrain from using the word Floquet here because the semiclassical equations are nonlinear and Floquet typically refers to linear system analysis. First I will note that the equations of motion (4.10) are actually that of a parametrically modulated pendulum with coordinate and momentum swapped. This becomes a bit more transparent by deriving the second order equation for  $k$  as

$$\ddot{k} = -\frac{2J [V_0(1 + \alpha \sin(\omega t + \varphi)) m\omega_0^2 d]}{\hbar} \sin kd. \quad (4.11)$$

Clearly this has the form  $\ddot{\theta} = -\omega_{\text{eff}}^2(t) \sin \theta$  which is the pendulum equation of motion, but with the angle represented by quasimomentum. Note that the curvature is critical here, and without it  $k$  simply follows the acceleration theorem. The phase space topology of a pendulum is that of a cylinder, and the extended axis here is position in place of angular momentum. For the experiment where we remain on one side of the harmonic potential, this corresponds to the regime of purely rotating solutions which means that

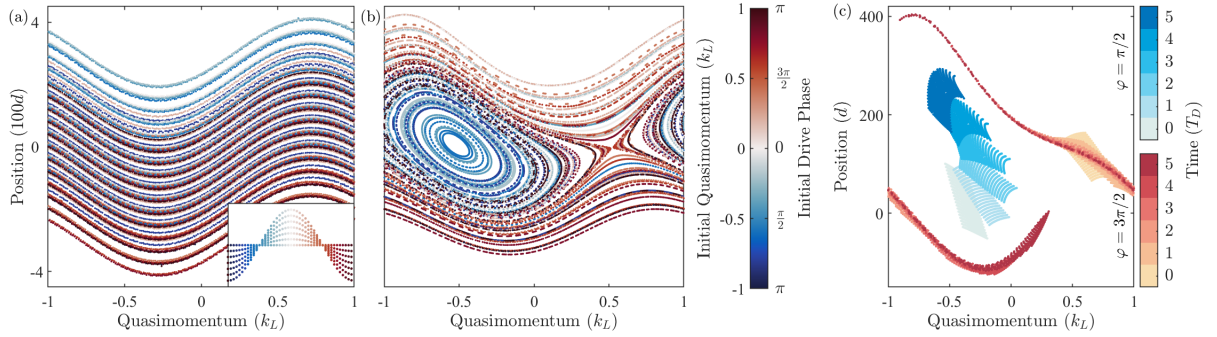


Figure 4.4: Poincaré sections for amplitude modulated atoms in (a) homogeneously and (b) inhomogeneously tilted lattices. In the former case at finite detuning, the quasimomentum repeatedly wraps around the Brillouin zone and this can be understood in terms of the perturbative arguments given at the end of section 4.1. The sign of detuning characterizes the direction in which the trajectories wrap around the Brillouin cylinder. On resonance (inset), the trajectories unwrap for linear spatial transport yielding the profile of (4.8). In the presence of curvature, two fixed points of different stabilities leads to a separatrix-like feature with a region of stroboscopic trajectories which do not wrap the cylinder. (c) Stable wavepacket transport and rapid spreading observed in the data can be visualized through the flow of trajectories around the different fixed points in this Poincaré map.

the compact variable winds only in one direction in continuous time (the distinction of continuous time is important), i.e. the angular momentum of the pendulum does not change sign. Further details about the parametrically driven pendulum can be found in [43, 44, 45].

Let us first consider the case where the curvature  $\omega_0$  vanishes. We hope here to gain insight into the structure of super Bloch oscillations, that is oscillatory transport over many periods at finite detuning and linear transport on Wannier-Stark resonance. As can be seen in figure 4.4, the stroboscopic dynamics are quite simple and should be understood in analogy to the arguments of the previous section. At small nonzero detuning, the quasimomentum shifts each cycle and there will be an oscillatory spatial profile as the phase between drive and Bloch oscillation evolves according to (4.8). Topologically, these stroboscopic trajectories all wrap around the Brillouin zone once, with the winding direction dictated by the sign of the detuning (in regard to the previous paragraph, note

that the Poincaré orbits can wind in different directions while the true continuous time trajectories wind in a single direction for purely rotating solutions). These are both incontractible loops on an infinite cylinder and topologically distinct from each other. In order to go from one configuration to the other as the detuning is swept, there must be some “topological” transition on resonance where these Poincaré trajectories unwrap from the cylinder, corresponding to the fact that the quasimomentum exactly maps back to itself after a Bloch period in this situation. Here we get exactly the linear transport profile predicted by (4.8). Importantly, this means we have fixed points (specifically lines of fixed points for all  $x$ ) appearing at two points in the Brillouin zone  $k = \pm 0.5$ , or alternatively for two drive phases  $\varphi = \pi/2, 3\pi/2$ . In these two cases of near resonant and resonant driving, one can interpret the presence of the near resonant modulation as providing the tunneling/dispersion to the stroboscopic dynamics, and the detuning as generating a stroboscopic force. For instance, we can start with the baseline case of a static Bloch Hamiltonian with no drive where the Poincaré map is trivial, and associate that with the trivial continuous time evolution of fixed particles on a lattice. Then the addition of a resonant drive in the former system leads to delocalized stroboscopic dynamics in analogy with the effect of introducing a hopping term to these fixed particles. Similarly, introducing the detuning to this driven system localizes the Poincaré dynamics to a super Bloch localization length just as adding in the force localizes the static tunneling particles to a Wannier-Stark length.

Now we turn on the curvature  $\omega_0$ . A special position now emerges where the fixed point is preserved, namely where the drive frequency is on resonance with the local force. What we see from the panel (b) of figure 4.4 is that the fixed points at opposite sides of the Brillouin zone have differing stabilities, namely one is a center with trajectories orbiting around it and the other is a saddle point with both a stable and unstable axis. This induces a separatrix-like feature to the Poincaré section. Far away from the

local Wannier-Stark resonance we get curves similar to those for a finite detuning and homogeneous force with trajectories that wind around the Brillouin zone in one direction or the other. However, now we need to interpolate the conditions by simply moving along position space, and the presence of fixed points enable this topological transition along the Brillouin cylinder. In particular in the separatrix region, one finds new orbits which are contractible on the surface of the phase-space cylinder, distinct from anything in the case of a homogeneous force.

How do these Poincaré sections enable us to understand the experimentally observed dynamics? For the  $\varphi = \pi/2$  drive with stable wave-packet transport, we model that as an ensemble of initial conditions beginning near the stable fixed point. Indeed the stability of the fixed point enables the wavepacket to remain compact in real space, and the flow of trajectories around the fixed point explains the observed steady spatial transport. Here the BEC is largely in a region of Poincaré orbits which are contractible on the phase space cylinder. On the contrary, the  $\varphi = 3\pi/2$  data is an ensemble starting out near the saddle point. This saddle point is surrounded by orbits of all 3 topological classes identified, and the diverging axis clearly leads to the rapid spatial expansion. Furthermore, the tendency for the wavefunction to bunch up near the edges is a result of the trajectories of the winding orbits to be confined to sufficiently far distances/detunings from the special resonance point. This is all summarized in panel (c) of figure 4.4.

Let me conclude this chapter with a brief outlook for future avenues along this experimental concept line. One possibility is adding in additional modulations (for instance a different frequency amplitude of force modulation) to make the semiclassical dynamics more chaotic. I believe it would be interesting to study how the structures observed here are modified for quasiperiodic versus commensurate driving. The effects of modulated interparticle interactions on SBOs leading to dynamical stability has been previously explored theoretically [46], and our Feshbach resonances could allow for study of this; some

---

work has been done on photon-assisted tunneling in amplitude-modulated tilted lattices with significant interactions [47]. Finally, there is always the goal of engineering a non-zero Berry curvature using Floquet engineering to realize effects of anomalous velocity, making the semiclassical dynamics more rich.

# Chapter 5

## Investigation of the Many-Body Quantum Kicked Rotor

Up to this point, we have limited ourselves to sinusoidal drive waveforms and single-particle dynamics. Another class of periodic driving involves kicked systems where the drive waveform is a regular train of sharply peaked pulses. Here we will discuss perhaps the most famous example, the delta kicked rotor, which exhibits a rich range of physical phenomena both classically and in the quantum world. Our experimental focus is on systems of many rotors coupled by interparticle interactions which probes at the understanding of thermalization and localization in many-body condensed physics.

The arXiv preprint version of this work is displayed in Appendix F [3].

### 5.1 Diffusive Chaos in the Classical Kicked Rotor

First I will review here the basic physics of the classical problem. Boris Chirikov introduced the so-called standard or Chirikov map around 1970 [48, 49], and a very nice overview of the kicked rotor is given in [50]. The physical model one can consider is a

pendulum with gravity sharply turned on at periodic intervals  $T$ . A classical pendulum Hamiltonian can be written as

$$H_{\text{pend}} = \frac{L^2}{2I} + mgR \cos(\theta). \quad (5.1)$$

Here we have pendulum radius  $R$ , momentum of inertia  $I = mR^2$  and angular momentum  $L = I\dot{\theta}$ . Dividing by a factor  $I$  and using the relabeling  $\dot{\theta} \rightarrow p$  and  $\theta \rightarrow x$ , we find the rotor Hamiltonian

$$H_{\text{rotor}} = \frac{p^2}{2} + k \cos x. \quad (5.2)$$

Here we defined  $k = g/R$ . We now consider  $\delta$ -function kicks of the potential occurring at periodic intervals  $T$ , so we multiply the potential term by  $\sum_n \delta(t - nT)$ . Taking time  $t$  to be normalized to this period and multiplying the entire Hamiltonian by  $T^2$ , we can write down the kicked rotor Hamiltonian

$$H_{\text{KR}} = \frac{p^2}{2} + K \cos x \sum_n \delta(t - n). \quad (5.3)$$

Here we defined  $K = kT$ . This is typically taken as the starting point when discussing kicked rotor dynamics. Given an initial condition  $x(t = 0) = x_0$  and  $p(t = 0) = p_0$ , we can integrate the dynamics explicitly. Let  $x_n$  and  $p_n$  denote the position and momentum right before the  $(n + 1)$ th kick (so at time  $t = n$  from the left). Then we have

$$p_{n+1} = p_n + K \sin x_n, \quad x_{n+1} = x_n + p_{n+1}. \quad (5.4)$$

This is the so-called standard map. One can take the phase space to lie on a torus (obvious for position since its an angle, but also this means that adding  $2\pi$  to  $p$  leaves

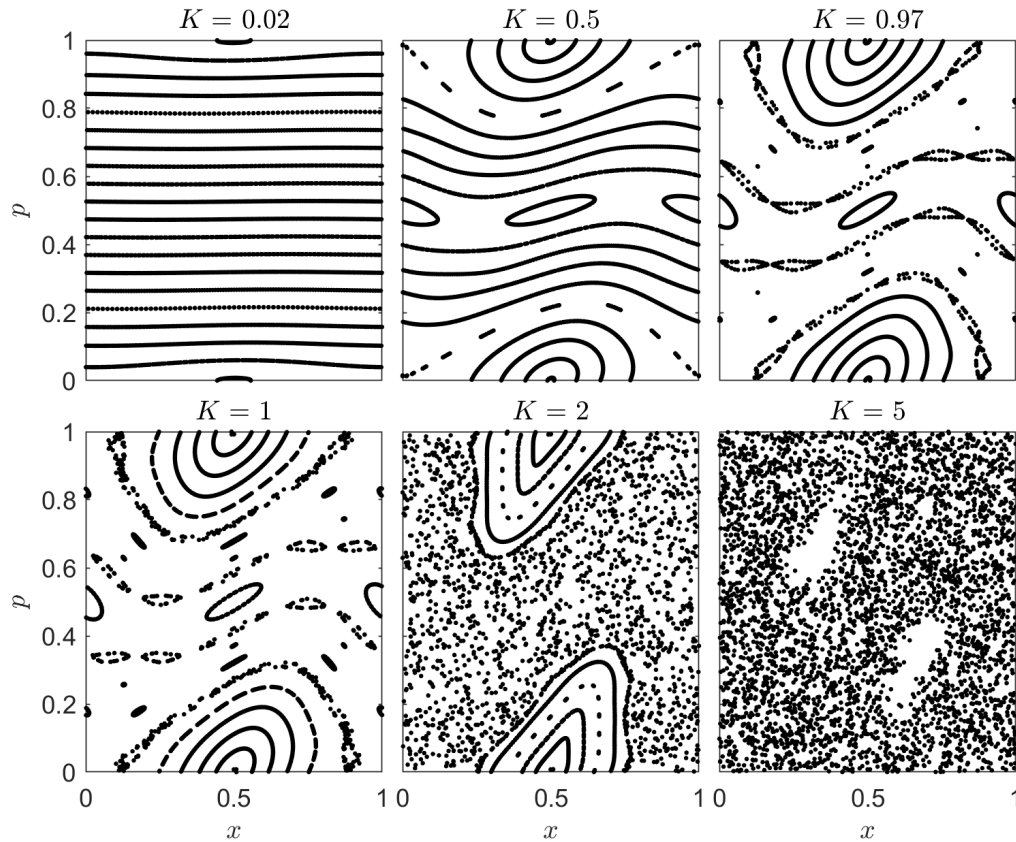


Figure 5.1: Poincaré sections for the standard map (5.4). At small  $K$ , the curves are simply distorted versions of a free particle and the motion is bounded. As  $K$  increases, a transition to chaos gradually occurs as the KAM tori are destroyed and the dynamics become ergodic on the torus. The simulations here are over 200 kicks and taken with 20 initial conditions for  $x = 0$  and  $p$  ranging from 0 to  $2\pi$ .

the map invariant). One can easily simulate the dynamics for varying  $K$  which is shown in figure 5.1. The small  $K$  behavior is understood in terms of the KAM theorem. Integrable Hamiltonians such as that of the free-particle have phase spaces which are densely covered by  $n$ -dimensional invariant tori where  $n$  is the number of degree of freedom. For small nonintegrable perturbations, the KAM theorem predicts that the invariant tori are not destroyed but rather distorted. Eventually for strong enough perturbations the KAM theorem breaks down and nonintegrability generically leads to chaotic behavior. It has been shown that the last KAM tori is destroyed at a critical value of  $K \approx 0.971635\dots$

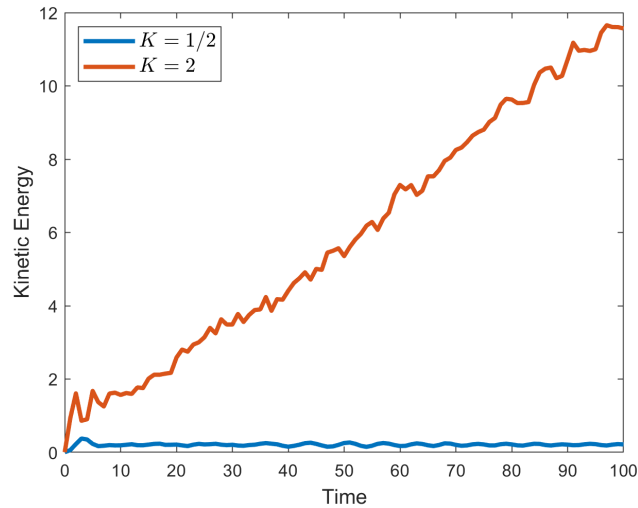


Figure 5.2: Energy of the classical kicked rotor in the weak and strong kicking regimes. For small  $K$ , the presence of invariant tori means that the motion in the phase space is bounded with an upper limit on the absolute momentum. As the motion becomes more and more chaotic, what one observes is a transition to diffusive energy growth where the momentum is ergodic and can increase along the entire real line.

The main observation relevant to our experiments from the classical kicked rotor is that the transition to chaos and ergodicity is accompanied by a transition to diffusive energy growth. This is depicted in figure 5.2. For sufficiently large  $K > 4$ , it is expected that the diffusion constant defined by  $p^2 \sim Dt$  is given approximately by  $D \approx K^2/4$ . The details of the transition between the two regimes I leave to the Scholarpedia article and references there within. The main difference we find in the quantum version of this problem is that the onset of chaos is associated with a different phenomenon, namely dynamical localization.

## 5.2 Localization in the Quantum Kicked Rotor (QKR)

Now we seek to understand the quantum dynamics of the Hamiltonian (5.3). A number of theorists contributed to our theoretical understanding of the problem includ-

ing Chirikov, Shepelyansky, Prange, Izrailev, Grepel, Fishman and others; their early works showed that chaos in the quantum kicked rotor was associated with the phenomena of dynamical localization, and further that this dynamical localization could be mapped onto the phenomena of Anderson localization in disordered crystals [51, 52, 53, 54, 55]. This was confirmed experimentally by Raizen in [56] using the atom-optics version of the QKR, to be shortly discussed. Since then this atom-optics rotor platform has been studied rather extensively in experiment in the single-particle regime, realizing things phenomena such as accelerator modes, fractional quantum resonances, and higher dimensional localization with quasiperiodic drives [57, 58, 59, 60, 61, 62, 63, 64, 65, 66].

First we will cover the mapping of the atom-optics to the delta QKR to establish experimental relevance with our experiment. We consider noninteracting atoms subjected to  $T$ -periodic square pulses of an optical lattice with duration  $\tau$ . We write the Hamiltonian as

$$H = \frac{p^2}{2m} + \frac{V_0}{2} \cos(2k_L x) \sum_n f_\tau(t - nT). \quad (5.5)$$

Here  $f_\tau(t)$  denotes a function which is 1 on the interval  $t = 0$  to  $t = \tau$  and 0 everywhere else; one can also model more realistic pulse shapes, for instance the Gaussian assumed in [56]. One critical difference between the classical and quantum case is that we have an intrinsic scale set by Planck's constant, so rather than just a single variable parameter  $K$  characterizing the kick strength, we should also have an effective Planck's constant  $\hbar$ . To reach the desired form, we multiply (5.5) by  $4k_L^2 T^2/m$  and make the following mapping for the canonical coordinates

$$\phi = 2k_L x, \quad \rho = -i\hbar \partial_\phi. \quad (5.6)$$

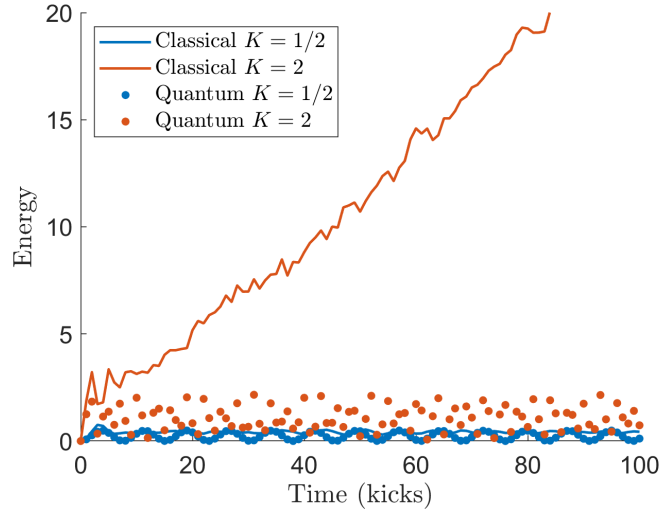


Figure 5.3: Localization of the QKR. In both classically chaotic and integrable regimes, the quantum rotor saturates to a finite value at long times.

with the following parameters

$$\tilde{k} = \frac{4\hbar k_L^2 T}{m} = 8\omega_R T, \quad K = \frac{2k_L^2 T V_0 \tau}{m} = \frac{\tilde{k} V_0 \tau}{\hbar 2}. \quad (5.7)$$

In addition we let  $\tau \rightarrow 0$  while keeping  $V_0 \tau$  finite to map the square pulses to  $\delta$ -functions.

Normalizing time  $t$  again to the period  $T$  we finally find

$$H = \frac{\rho^2}{2} + K \cos \phi \sum_n \delta(t - n). \quad (5.8)$$

One can check that the canonical commutation relation is

$$[\phi, \rho] = i\tilde{k}. \quad (5.9)$$

Indeed this Hamiltonian (5.8) is the same form as the classical delta-kicked rotor (5.3) and so the mapping of our experiment to theoretical model is made explicit. The dynamically localized quantum evolution under this Hamiltonian is shown in Fig.5.3, and contrasted

to the diffusion in the classical kicked rotor case.

One should note the reduction of 3 experimentally relevant parameters  $V_0, \tau, T$  to 2 in the theoretical model  $\hbar, K$ . This reduction is made under the condition that  $V_0\tau$  is finite while  $\tau$  vanishes, as we see that only the product  $V_0\tau$  emerges in the expression for  $K$  (5.7). In practice,  $^7\text{Li}$ 's light mass actually makes the condition of small  $\tau$  challenging. Physically employing the  $\delta$ -function approximation is assuming we are in the Raman-Nath diffraction regime where kinetic energy is ignorable over the duration of the pulse, which is approximately expressed by the condition  $2\sqrt{V_0 E_R}\tau/\hbar \ll 1$  [67]. For the experiments presented later with  $\tau = 0.3 \mu\text{s}$  and  $V_0 = 64E_R$ , this parameter is approximately 0.76 (there is an ambiguity of a factor  $2\pi$  in defining the condition [68], which would reduce the parameter to 0.12). Either way, this suggests that the system is in between the Raman-Nath and Bragg diffraction regimes, and thus finite-pulse-width effects require careful investigation. One can probe the effects of pulse length duration via simulations, as shown in Figure 5.4. We find that generically the effect of larger  $\tau$  is to localize the distribution at a lower energy, though the magnitude of this effect appears to depend on  $K$ .

One way to think about this effect is that if the kinetic energy plays an important role over the course of the kick, the non-zero momentum states will traverse a significant fraction (if not more than 1) of a lattice site during the pulse. In the classical picture, the particle then feels an averaged, weaker “kick”. A rough estimate aside from the Raman-Nath condition is that given by considering the motion of the lowest non-zero momentum state  $2mv_R$ , with  $v_R = \hbar k_L/m$  the recoil velocity. For reference,  $v_R \approx 53.6\text{nm}/\mu\text{s}$ , so that a particle moving at  $2v_R$  moves 6% of a lattice spacing in 300 ns. For the experiments discussed here, we typically use an effective  $\tau = 300$  ns, which is roughly composed of 200 ns rise and falls of the beam intensity with a 100 ns hold at the peak. While 6% may not seem so significant, we should be aware that higher momentum modes may be excited

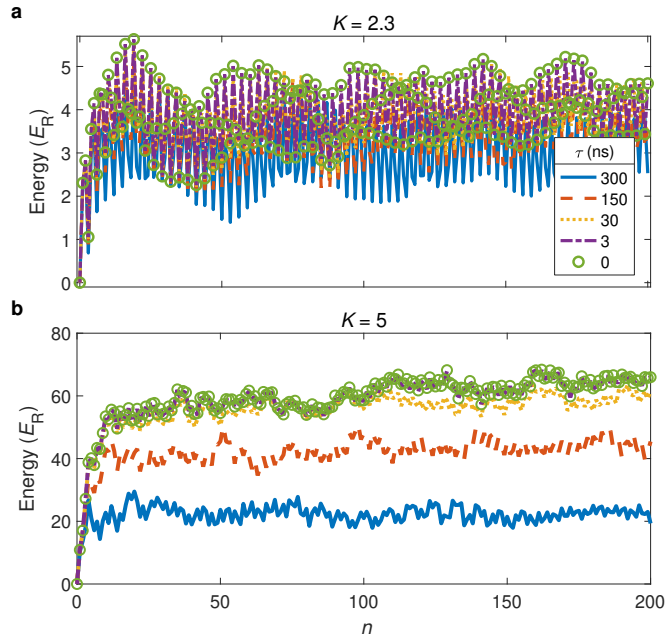


Figure 5.4: Simulations of energy versus number of kicks  $n$  for varying effective pulse widths  $\tau$  at a fixed stochasticity parameter  $K$ . In general, the effect of long pulse durations is to reduce the localization energy, though.

in the localized state and will potentially experience a more strong averaging of the potential. The finite pulse duration can be thought of as leading to an effective kicking strength which decays with increasing momentum, causing even the classical phase space to localize above a certain momentum [69]. This is an important consideration in probing quantum dynamical localization which occurs in the classically chaotic regime. For our parameters, the estimate given in [69] for the momentum boundary between classically chaotic and integrable regions due to pulse width is roughly  $\pm 33.2k_L$ , which is much larger than any excitation we observe in our localization experiments (in some other cases considering resonances to be discussed this may play a role). Thus we do not expect that the finite pulse duration qualitatively affects the quantum nature of the dynamical localization physics we study.

Just like the classical problem, we can formulate the stroboscopic solution as a map.

We need the following two propagators to construct the 1-cycle evolution operator

$$U_{\text{kick}} = \exp\left(-i\frac{K \cos \phi}{\hbar}\right) \quad (5.10)$$

$$U_{\text{free}} = \exp\left(-i\frac{\hbar q^2}{2}\right). \quad (5.11)$$

Here  $q$  is the momentum quantum wave number (I avoid using  $k$  since we already have  $K$  and  $\hbar$ ). The 1-cycle evolution operator is simply  $U = U_{\text{free}}U_{\text{kick}}$ . Given an initial wavefunction  $\psi$ , one can simply apply (5.10) and (5.11) repeatedly to find the energy after  $N$  kicks. A common way to do this is to Fourier transform the wavefunctions between momentum and position space between applications of the two propagators. For a true rotor which has a compact angular variable, one has a quantized angular momentum variable. For the atom-optics/kicked particle case where position is on the entire real line, one can establish equivalence by noting the Bloch's theorem ensures that only momentum states separated by a reciprocal lattice vector are coupled, and thus quasimomentum is conserved. Thus one can simply solve the quantized rotor problem for varying quasimomentum independently, which can be more numerically efficient, and then average over an appropriate quasimomentum sampling. To model finite square pulse dynamics, one can instead compute the band energies  $\mathcal{E}_{nq}$  by diagonalizing the following Hamiltonian whose matrix elements are given in momentum space by

$$H_{j,j'}(q) = \frac{\hbar^2}{2}(q+j)^2\delta_{j,j'} + \frac{KT}{2\pi}\delta_{j,j\pm 1}. \quad (5.12)$$

Here  $q$  denotes a quasimomentum in the first Brillouin zone and  $j$  is an integer. Once

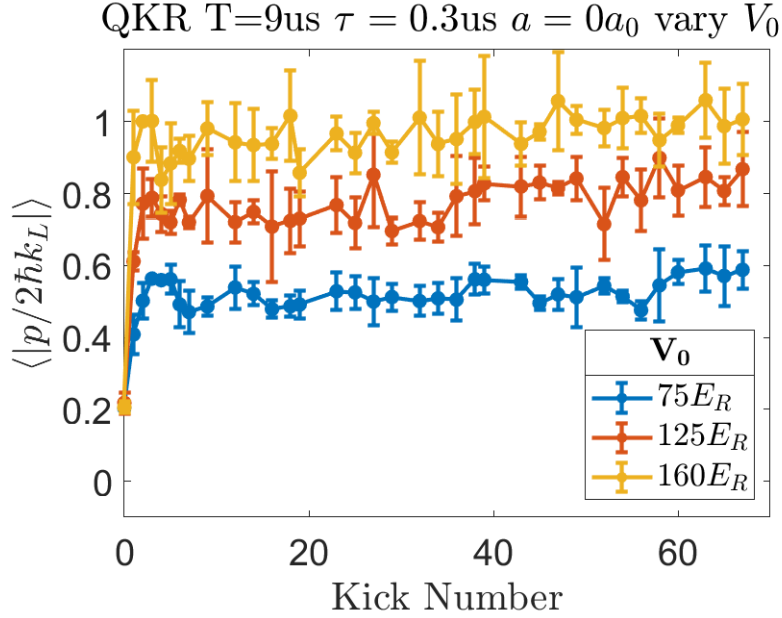


Figure 5.5: Noninteracting kicked rotor experiments demonstrating dynamical localization dynamics with a saturation in the measured energy. Here, the absolute value of the momentum was used as a proxy for the energy as it was less noisy. The momentum space localization length increases with increasing kicking strength, which is related to the dependence of the classical diffusion coefficient on  $K$ .

the band energies are computed, the relevant propagators to switch between are

$$U_{\text{pulse}}(q) = \exp\left(-i \frac{\mathcal{E}_{nq}}{\hbar} \frac{\tau}{T}\right) \quad (5.13)$$

$$U_{\text{free}}(q) = \exp\left(-i \frac{\hbar k(q+j)^2}{2} \frac{T-\tau}{T}\right). \quad (5.14)$$

Alternatively, one can employ split-step propagation techniques discussed in section A.1 to model more accurate pulse shapes.

Finally before moving onto the main topic of this section which is many-body effects, it is important to inspect that our noninteracting experiment reproduces the same localization effects. The experimental procedure up to preparation of a non-interacting BEC follows exactly as outlined before in section 3.2. However, now rather than ramp up the lattice depth adiabatically, the traps are snapped off and the optical lattice is

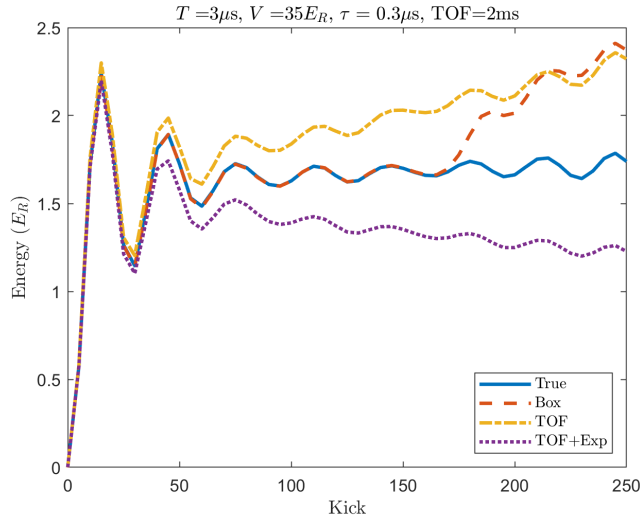


Figure 5.6: Modeling of kicked rotor energy measurement via a TOF. Different assumptions about the appropriate time in conversion from position to momentum can affect the perceived trends. Assumptions of discrete momentum occupations (box method) can be useful but are also prone to error.

repeatedly, periodically pulsed on for brief periods of time  $\tau$ . The atoms are allowed to evolve completely freely in between kicks. Finally, to measure the absorbed energy we use a time-of-flight (TOF) to convert momentum to position spread and compute the variance. The results are shown in Fig. 5.5, with a clear dynamical localization plateau emerging for varying kick strengths.

An important aspect in analyzing this data is that the duration of the kicking is around  $600\mu\text{s}$ , which is not small compared to our typical TOF times of 2-3ms. Thus the position space motion during the experiment will not necessarily be negligible and will tend to have a systematic effect of causing the energy to be overestimated as a result of broader initial spatial distributions. One approach is to try to measure the distribution at multiple TOF times and fit to a standard  $\sqrt{\sigma_x^2 + \sigma_p^2 t^2}$  curve to try to account for the changing  $\sigma_x$ , but we did not find great success with this method which still ignores the tendencies for certain correlations to establish. An alternative method is to alter the time used to calculate the position to momentum conversion by including

part of the kicking duration. For a given set of kicking parameters, we modeled this with noninteracting split-step simulations (see section A.1) including the TOF expansion in order to determine the most appropriate position to momentum conversion factor. An example is shown in Fig. 5.6, but in general we do not find that any single scheme is appropriate in all situations. The best conversion factor for each set of experimental parameters is instead determined on a case by case basis using these simulations.

### 5.3 Prethermalization and Delocalization in the Interacting Kicked Rotor

The dynamical localization of noninteracting QKRs is well-known to be a realization of Anderson localization in momentum space [53, 54]. Anderson localization [55] is a generic wave phenomena where randomness leads to a suppression of transport. In the simplest form of the problem, one can consider a single-particle hopping on the sites of a 1D lattice with the chemical potential on each site randomly drawn from the interval  $[-W, W]$ .  $W$  is called the disorder strength, and in 1D systems  $W \neq 0$  leads to energy eigenstates which are exponentially localized in space (in contrast to typical delocalized Bloch waves for  $W = 0$ ). In the Floquet analysis of the kicked rotor problem, the hopping is facilitated by the kicks between discrete momentum modes, and the phase accumulated over a period  $T$  for the different momentum modes generates a pseudo-random sequence of numbers playing the role of the disordered on-site energies.

Since around 2006, the phenomenon of many-body localization (MBL) as an avenue for escaping thermalization and preserving memory of local information has been a hot topic [70, 71, 72, 73, 74, 75, 76, 77, 78]. The detailed phenomenology underlying the MBL phase is beyond the scope of this thesis, but at its most simplified level MBL is the per-

sistence of Anderson localization in the presence of many-particle interactions. Naturally then one is led to ask whether an analogue of MBL also exists for the dynamical localization problem in the context of the QKR. Indeed recent theoretical work suggests that there may exist regimes of few-body and many-body QKR Hamiltonians which exhibit such a many-body dynamically localized (MBDL) states [79, 80, 81, 82, 83]. There is a reasonably long list of other numerical/theoretical studies suggesting a dynamical delocalization effect by interactions [84, 85, 86, 87, 88, 89, 90, 91, 92]. Many are mean-field treatments based on the Gross-Pitaevskii equation, which in 1D and taken with periodic boundary conditions on a single lattice site seem to unambiguously lead to a subdiffusive (sublinear) energy delocalization at long times. The applicability of such results to real experiments is questionable though, due to possible scattering and dynamical instabilities leading to large condensate depletion fractions.

In this section, I will present the first experimental probe of the effects of interactions on dynamical localization in the QKR model. The experimental sequence largely follows what has been previously discussed. The key difference however is that these experiment are performed in the vicinity of Li's magnetic Feshbach resonance as opposed to near the zero scattering length crossing. While the BEC is held in the optical dipole trap, we slowly ramp the field over tens of ms to vary the scattering length of the condensate. Once the ramp is completed, the optical dipole trap is then turned off and the lattice beams begin to repeatedly pulse. Two potential mechanisms as a consequence of interactions can be immediately identified. The first is a simple mean-field shift which locally winds the phase of the condensate based on the real-space density; we estimate that this effect is not dominant as the time-scale is expected to be around a ms while we are able to observe interaction based effects in around  $100 \mu\text{s}$ . Ultimately we believe the primary interaction based mechanism present in the data is elastic collisions between the discretely occupied momentum modes [93, 94, 95, 96, 97]. This is because such a process depends

additionally on the relative velocity between condensates and thus happens much faster than the mean-field dynamics. The expectation is that such scattering processes take atoms out of the condensate wavefunction and into unoccupied momentum modes in an energy-conserving halo. These modes are outside of the mean-field description and present a challenge for accurate modeling of a dynamical many-body bosonic system in 3 spatial dimensions.

The main result of this work is presented in Fig. 5.7A. While a noninteracting sample exhibits dynamical localization, saturating around a finite energy for over 800 kicks, interacting samples clearly demonstrate the destruction of the dynamically localized plateau with increasing scattering length. At the intermediate interaction strength ( $a = 240a_0$ ), we observe an initial saturation to the same energy as non-interacting samples, suggesting the existence of a reasonably long-lived prethermal state. Prethermalization behavior is typically associated with a separation of time-scales [98], that is a rapid initial relaxation to the prethermal quasi-equilibrium, followed by a “long” persistence at this state before eventual thermalization. Here we indeed resolve such behavior, with an initial classical diffusion breaking to a prethermal dynamically localized state in a few kicks, which is then sustained till about 300 kicks before heating ensues. In contrast, the  $760a_0$  trace exceeds this localized energy after around 100 kicks; whether a quasiequilibrium dynamical state is truly established in this stronger-interacting sample is less clear. The shaded region indicates a localization energy  $E_{\text{loc}}$  (and subsequently a momentum space localization length  $k_{\text{loc}}$  by assuming an exponentially localized distribution  $\sim e^{-k/k_{\text{loc}}}$ ) characterizing the dynamical plateau, which we estimate by averaging over the noninteracting data points for  $n \geq 100$ . We can then use this estimate to characterize other features of behavior in the system. We note that the energy measurements presented here are quite challenging to extract, and thus we used an adaptive ROI generation procedure to reduce noise on the results, which is described in full detail in the methods section

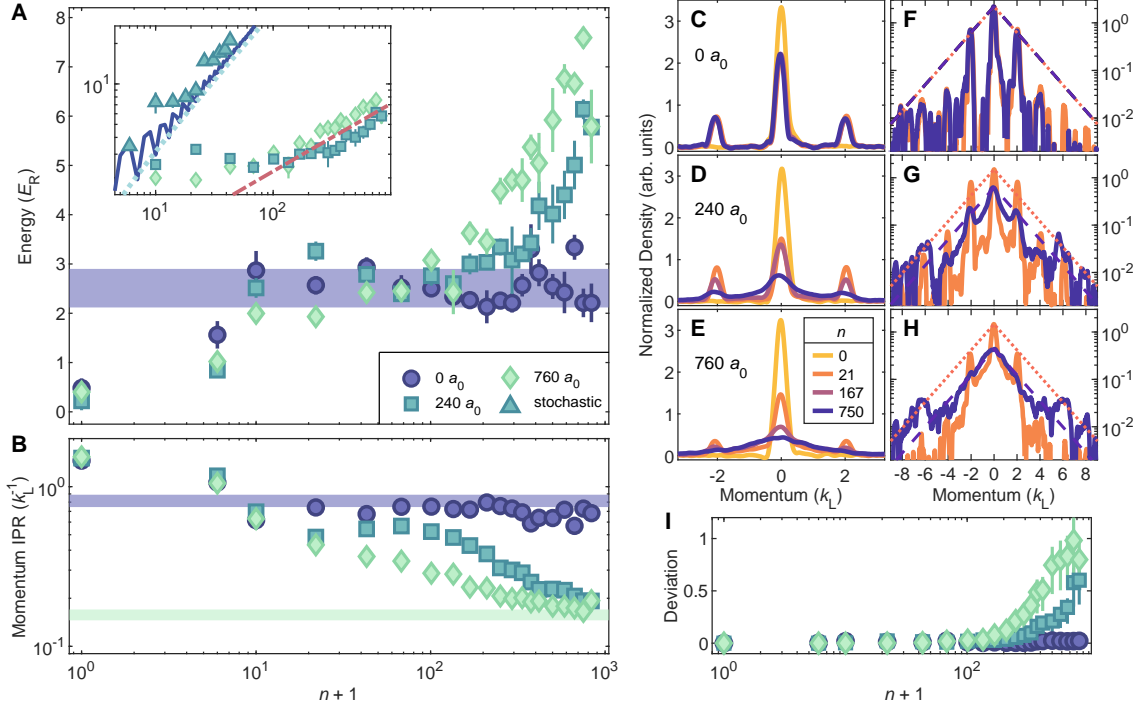


Figure 5.7: **Observing the interaction-induced emergence of quantum chaos.** (A) Energy versus kick number for varying  $a$ . Blue horizontal shaded region indicates the measured single-rotor localization energy of  $E_{loc} = 2.5(4)E_R$ . Here  $V_0 = 64E_R$ ,  $T = 1.2 \mu\text{s}$  and  $\tau = 300 \text{ ns}$  ( $K \approx 2.3$  and  $\tilde{k} \approx 1.5$ ). The inset contrasts interaction-induced delocalization and anomalous diffusion with classical diffusion caused by a sequence of random offsets from the average kick spacing  $T$  drawn uniformly from the interval  $[-T/4, T/4]$ . The solid curve is noninteracting quantum theory and the dotted line is a diffusion curve  $4Dn/\tilde{k}^2$  with  $D \approx 0.19$  extracted from the classical standard map [49]. The red dot-dashed line is a subdiffusive  $\sqrt{n}$  law serving as a guide to the eye. (B) Momentum-space IPR with transverse dimensions integrated out. The shaded regions are predictions for two exponentially localized distributions with  $1/e$  localization length  $k_{loc} = \sqrt{E_{loc}} \approx 1.6(1)k_L$ . (C-E) Normalized smoothed momentum space densities at various  $n$ . (F-H) The same densities on a logarithmic scale. The orange dotted and purple dashed lines are exponentially localized curves  $\exp(-k/k_{loc})$  with amplitudes normalized to match the peak of the measured distributions at the given  $n$ . (I) Deviation from exponential localization over time based on integrated ratio between measured and exponential distributions with error bars computed from uncertainty in  $k_{loc}$ .

of [3].

Fig. 5.7B shows one other aspect of the same evolution, plotting the momentum space inverse participation ratio (IPR) versus kick number. The IPR characterizes the “number” of states over which the system is distributed, thereby also probing how collisional momentum redistribution washes out the originally discrete momentum modes, a process less easily inferred from energy measurements. For a wavefunction  $\psi(x)$  of a 1-dimensional continuous variable  $x$ , the IPR in the  $x$ -space is given by  $\int_{\mathcal{D}} |\psi(x)|^4 dx$ , where  $\mathcal{D}$  indicates the relevant domain on which  $x$  is defined. While the  $240a_0$  data exhibit a clear steady-state behavior for 100 kicks, the  $760a_0$  IPR decreases monotonically for almost the entire experiment. The shaded regions provide comparisons to two potential exponentially localized distributions. The blue shaded region is obtained by numerically computing the IPR for the momentum space distribution  $\exp(-|k|/k_{\text{loc}}) \sum_j \exp(-(k - 2k_L j)^2/w^2)$ , which models a Gaussian comb with an exponential envelope. This is a reasonable expectation for a finite-size, localized noninteracting condensate occupying only discrete momentum modes. The width parameter  $w$  is measured from fitting the  $n = 0$  noninteracting condensate and takes into account the momentum-space resolution of the TOF given the finite condensate spatial extent. The width of the region is based on Monte Carlo simulation of uncertainty in  $k_{\text{loc}}$ , where the resulting distribution is fit to a Gaussian to extract the mean and standard deviation. The green shaded region is calculated analytically for a pure exponential distribution of infinite extent and is given by  $1/4k_{\text{loc}}$ . Taking into account the finite width of the imaging region changes the distribution normalization and leads to the following correction factor  $(1 - \exp(-2k_0/k_{\text{loc}}))/(1 - \exp(-k_0/k_{\text{loc}}))^2$ ; here  $k_0 \approx 9.85k_L$  is the half-width of our images which yields a negligible correction factor of  $\approx 1.006$ . The width of the region is computed through linearized error propagation. Since these shaded regions bound the IPR delocalization, it is not obvious that there is an accompanying loss of exponential localization directly from this metric, which will be

discussed later.

As already mentioned, the three-dimensional nature of scattering in our system means that momentum-space IPR should really be defined in all 3 dimensions for the experiment. However, since the imaging system naturally integrates out one dimension in our measurement of the atomic density, computing such a metric would require reconstruction of the full atomic density through appropriate symmetry assumptions (assuming cylindrical symmetry one can use the inverse Abel transform). Instead since we are largely interested in some effective axial dynamics along the kicking direction, we simply integrate out the remaining transverse dimension in the image, before normalizing, squaring and then integrating to compute what we call the projected IPR. Additionally, I found that to compute this particular metric it was necessary to smooth the data so that background fluctuations would not dominate at the lower values of the metric. I found this was also the case when the IPR was calculated in two dimensions. The metric would tend to converge to a solution as the smoothing parameter was increased. This smoothing is really only helpful for this metric and not the energy, since typical smoothing protocols tend to be moment-conserving. Aside from the smoothing, we found the the IPR tends to be a much more consistent metric than the energy, and much less sensitive to things like ROI choice. Overall the IPR shows similar trends to the energy, namely a much clearer finite duration plateau for the  $240a_0$  data than the  $760a_0$  trace. However, both still significantly depart from the noninteracting values at long times in agreement with an interaction-induced delocalization.

A second key result of these measurements is that the observed delocalizing dynamics clearly exhibit anomalous diffusion: it appears that even interacting quantum kicked rotors absorb energy much more slowly than classical rotors. The inset of Fig. 5.7A compares the nature of the observed interaction-induced subdiffusive delocalization with linear energy growth in the classically chaotic model. We experimentally simulate clas-

sical dynamics by adding stochastic fluctuations to the kicking period  $T$ , making use of the known sensitivity of dynamical localization to timing noise [99]. More generally, it is known that dynamical localization can be sensitive to a variety of forms of decoherence [100, 101, 102]. In general, this noise causes a subdiffusive heating which approaches classical linear diffusion as the strength of the fluctuations increases. The triangles in the inset show our kicked BEC with the interval between kicks randomized. The dark blue line is a noninteracting simulation, and the light blue dotted line is a diffusion curve from fitting the corresponding classical kicked rotor map. In contrast, the slope of energy increase for the two interacting samples at long times is clearly much smaller. In particular, the red dashed line is a  $\sqrt{n}$  law serving as a guide to the eye. From fitting the data, we typically measure diffusive exponents in the range  $[0.4, 0.6]$ . For reference, 1D Gross-Pitaevskii simulations on a ring [89] predict  $\alpha \in [0.5, 0.8]$ , though a direct quantitative comparison to theory is challenging due to the high depletion of the condensate and the three-dimensional nature of the experiment. Theoretical studies of the effect of local nonlinearity on real-space Anderson localization instead suggest  $\alpha \in [0.3, 0.4]$  [103, 104], but the long-range nature of contact interactions in momentum space similarly complicates comparison.

For further insight into the dynamics of kicked interacting quantum systems we examine the evolution of the momentum distribution, shown in Figs. 5.7C-E. We observe a clear distinction between the noninteracting samples, which settle at a sharply-peaked dynamically-localized momentum distribution, and the interacting samples, which gradually smear out in momentum space due to scattering. Plotting these same densities on a logarithmic scale in Fig. 5.7F-H illuminates the destruction of dynamical Anderson localization by assessing the departure from exponentially-localized Floquet states. The smeared-out lower-energy modes actually appear to maintain the expected localization length, and thus do not trivially indicate a departure from exponential localization. This

observation is also reflected in the fact that two predictions based on exponentially localized distributions bound the measured IPR in Fig. 5.7B. Instead, the departure from exponential localization manifests in the emergence of increased relative population in the tails of the distribution. It is interesting to note that recent theory suggests that even MBDL phases are expected to exhibit universal power-law decaying tails [105]. In Fig. 5.7I we quantitatively characterize the overall deviation from exponential localization, revealing a break time near 200 kicks for both interaction strengths. These findings provide a second experimental signature of the destruction of the dynamically localized state by interactions, now both at the level of macroscopic observables and squared wavefunctions.

The plotted localization metric in Fig. 5.7I is  $\int_{-k_0}^{k_0} \max[r(k) - 1, 0] dk / 2k_0$ . Here,  $r(k) = |\psi(k)|^2 / \exp(-k/k_{\text{loc}})$  is the ratio of the measured axial density denoted  $|\psi(k)|^2$  and an exponential localization envelope. Here the maximum of  $|\psi(k)|^2$  is set to unity. Taking the maximum of  $r(k) - 1$  and 0 ensures that the result is only sensitive to regions of the distribution which decay more slowly than exponentially. That is, it interprets 0 as “at least exponentially” localized with respect to a given localization length, and thus characterizes departures from a given dynamically localized state in the traditional sense of exponentially localized wavefunctions. We note however that the system remaining exponentially localized but with a larger localization length would result in a non-zero value for this metric, which motivates the direct inspection of the distributions in Figs. 5.7F-H. The reported values and errorbars are extracted by propagating a Gaussian uncertainty in the measured  $k_{\text{loc}}$  through a Monte-Carlo simulation. We find that the resulting distributions interpolate between sharply peaked at 0 with a rapid fall-off when well-localized, to positively skewed with non-zero peak in the delocalized regime. We empirically find that a log-normal distribution fits the Monte Carlo result well, and we use this fit to extract the data reported in Fig. 5.7I. In particular, the markers indicate

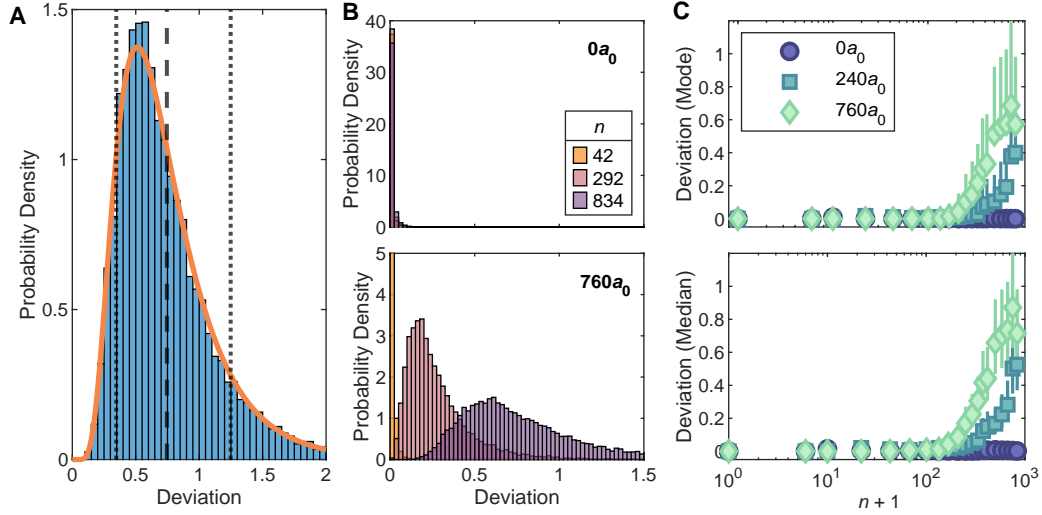


Figure 5.8: **Characterizing Monte Carlo distributions for deviation from exponential localization.** (A) Distribution for the  $760a_0$  data in Fig. 2 at  $n = 500$ . Orange line indicates the fit to a log-normal distribution. Vertical dashed line indicates the mean, and the vertical dotted lines surrounding it indicate the interquartile range reported as the errorbars. (B) Evolution of the distribution over time for non-interacting and interacting samples. Note the difference in y-scale. The  $n = 42$  trace in the lower panel is cut-off vertically for visual clarity on the larger  $n$  distributions. (C) Alternative characterizations of the exponential localization deviation in terms of the mode and median of the simulated distributions (indicated by the markers, the errorbars are left as the interquartile range), as opposed to the mean shown in the main text Fig. 2I.

the mean of the distribution and the errorbars represent the interquartile range containing the central 50% of the distribution.

Because these distributions are significantly not normal, it is important to check the distributions explicitly. In Fig. 5.8, we show further details on the Monte Carlo simulated distributions. The distributions are generated by computing the defined deviation parameter for  $10^4$  values of  $k_{\text{loc}}$  drawn from a Gaussian centered at  $1.58k_L$  and with standard deviation  $0.12k_L$ . An example distribution for a sample which has delocalized is shown in Fig. 5.8A, clearly showing the skewed probability densities we obtain from this procedure. The solid orange line indicates the log-normal distribution fit we use to extract parameters such as the mean and interquartile range of the distribution. We

note that the use of a log-normal distribution here is only motivated empirically as a systematic method to determine such quantities.

In Fig. 5.8B, we contrast how these simulated distributions evolve in time for localized noninteracting samples and delocalizing interacting ones. In the noninteracting case, the distributions are extremely sharply peaked at 0 and are relatively unchanging in time, agreeing with the expectation of dynamical localization. In the latter however, the distribution is only peaked at 0 for short times indicative of the finite duration prethermal plateau we report, and gradually shifts away to non-zero values as the sample heats up. Importantly, at the later times the  $760a_0$  distribution has essentially vanishing probability density at 0 deviation, allowing us to confidently claim observation of departure from exponential localization. In Fig. 5.8C, we confirm that the reported behavior of deviation over time in Fig. 5.7I would not qualitatively change if we instead used the median or mode of the distribution instead of the mean.

To supplement the dynamical delocalization signals shown in Fig. 2 and demonstrate that this is not a particularly fine-tuned phenomena in the kicking parameter space, in Fig. 5.9 we show the same metrics for a larger kicking period  $T = 2.2 \mu\text{s}$ . The overall picture is unchanged, as the interacting samples show starkly different behavior from the noninteracting traces, departing from the localized value of each metric after a variable break time. Here the energy delocalization is obscured slightly as the different interaction strengths seem to initially localize to different energies. We attribute this partly to Thomas-Fermi expansion which reduces both the effective lattice depth experienced by the condensate and the initial kinetic energy of the sample, though we do not entirely rule out the possibility of different early-time prethermal behavior across interaction strengths. The correlation between localization length and quasimomentum spread is observed in noninteracting numerics. The different-colored shaded regions indicate our best estimates for the different localization energies at the 3 interaction strengths by

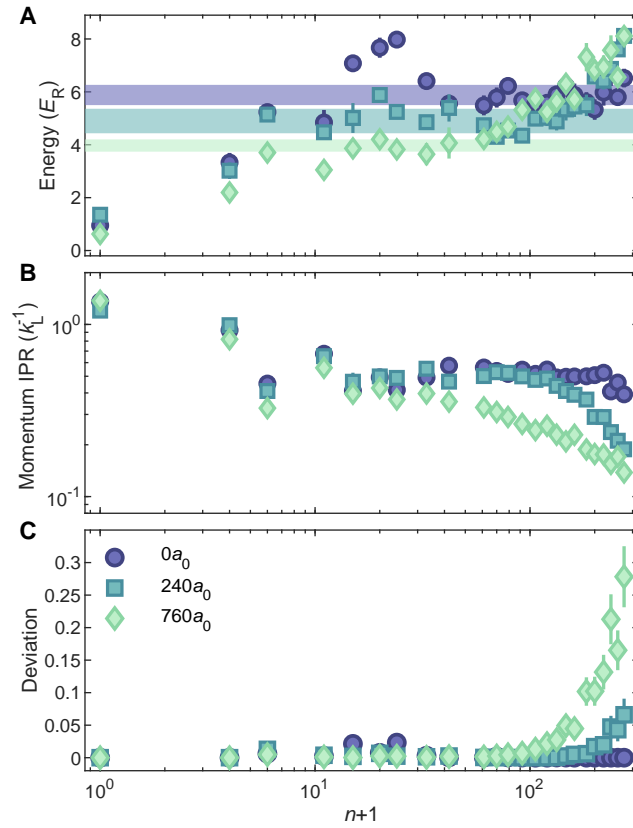


Figure 5.9: **Interaction-induced delocalization for a different set of kicking parameters.** The kick parameters are  $V_0 = 70 E_R$ ,  $T = 2.2 \mu\text{s}$  and  $\tau = 300 \text{ ns}$  ( $K \approx 4.6$  and  $\hbar \approx 2.8$ ). The (A) energy, (B) 1D momentum-space IPR and (C) deviation from exponential localization over time for varying scattering lengths. In A, the shaded regions indicate the extracted initial localization lengths for the three interaction strengths which we use for computing C.

computing the mean energy (and standard deviation) over windows of  $n$  where the data are minimally changing. These values are used to compute the exponential localization deviation in Fig. 5.9C. We do note a small trend visible at the end of the noninteracting traces; numerics suggest that this is consistent with variations in the localization length that occur over time for certain kicking parameters.

## 5.4 Time Reversal with Quantum Resonances

Outside of dynamical localization, the second characteristic feature of the QKR model is the presence of quantum resonances. Ignoring quasimomentum, such resonances happen whenever the quantized momentum states wind a rational phase relation with respect to each other between kicks, which simply corresponds to when  $\tilde{k} = 2\pi q$  where  $q$  is rational. This behavior can be interpreted as an atomic Talbot effect, which in its original conception corresponds to the phenomena where a plane wave of light diffracted off a periodic grating ultimately re-images itself a distance away called the Talbot length. For the kicked rotor we can define a Talbot time which corresponds to when each integer momentum state winds an integer multiple of  $2\pi$  phase between kicks (so that the free evolution becomes the identity), which by inspection corresponds to the condition  $q = 2$  or alternatively in atomic units gives a Talbot time  $T_T = h/4E_R$ ; for  ${}^7\text{Li}$  we have  $T_T \approx 9.95\mu\text{s}$ . This is the fundamental quantum resonance and has been extensively explored [57, 66, 106, 107, 108, 109, 110, 111, 112, 113, 114], both from the fundamental and applied perspective.

Here in particular I will focus on extensions of previous work investigating the use of the fundamental quantum resonance for time-reversal [109, 110, 107]. The essential idea is because the free evolution drops out of the map, if one is able to flip the sign of the kicking then that becomes equivalent to time-reversal. This can be done either by

spatially shifting the kicking lattice by half a period, or alternatively utilizing the fact that the wavefunction will undergo a spatial  $\pi$ -phase shift after a half-Talbot period. While such a protocol works exactly for a perfect 0 quasimomentum initial plane wave, in reality finite quasimomentum spread will decay the return fidelity. This then realizes the famous Loschmidt echo

$$F = \left| \langle \psi | U_2^\dagger U_1 | \psi \rangle \right|^2, \quad (5.15)$$

where  $U_1$  and  $U_2$  are time-evolution operators differing by some perturbation. This notion of Loschmidt echo time-reversal was originally conceptualized in trying to understand how time-reversible classical microscopic mechanics could lead to a time-irreversible statistical mechanics [115]. Of the many deep theoretical concepts that emerges from such a question, one is the notion of exponential sensitivity to initial conditions for chaotic systems which is manifest in this Loschmidt protocol. That is, while in principle the deterministic nature of mechanical laws should enable perfect time-reversal, in practice some error (whether from not perfect isolation of an experiment or numerical error in a computation) will always prevent such reversibility for a chaotic (many-body) system. This is more complicated in quantum mechanics due to linearity and unitarity of time-evolution, but nevertheless  $F$  serves as a key metric for understanding the emergence of irreversibility under Hamiltonian evolution.

In Fig. 5.10, we probe the effects of contact interactions on this QKR Loschmidt protocol. Due to technical limitations on our ability to ramp currents (magnetic fields) to manipulate the Feshbach resonance, we do not switch the sign of the scattering length  $a$ . Instead here we opt for the interpretation that the interactions are an additional perturbation along with the kinetic energy distinguishing  $U_1$  and  $U_2$ . This leads to a non-monotonic behavior in  $F$ . For smaller  $a$ , we perhaps surprisingly find that  $F$  actu-

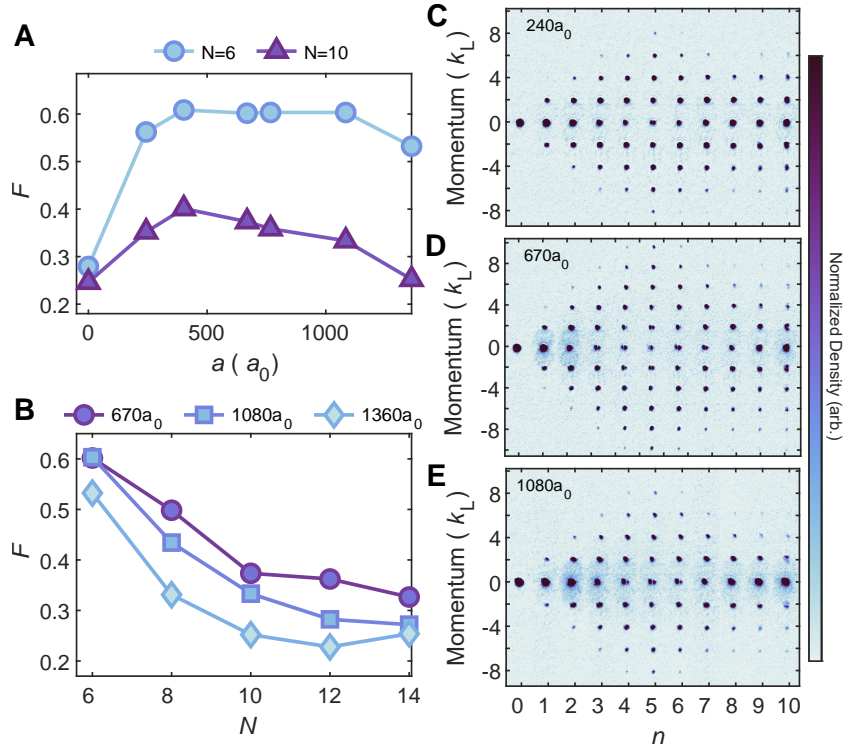


Figure 5.10: **Effect of interactions on reversibility in Loschmidt echo experiments.** (A) Measured Loschmidt echo fidelity  $F$  for a range of scattering lengths  $a = [0, 1500] a_0$  for  $N = 6$  (blue circles) and  $N = 10$  (purple triangles), where  $N$  indicates the total number of kicks; a first set of  $N/2$  kicks propagates the system *forward* in time and a second time-reversal set of  $N/2$  kicks propagates it *backwards*. (B) Measured fidelity  $F$  at three different interaction strengths as a function of total number of kicks  $N$  in a Loschmidt echo experiment. (C-E) Averaged absorption images of a BEC after the first  $n$  kicks of an  $N = 10$  Loschmidt echo protocol, for three different  $a$ .

ally increases, which we attribute to Thomas-Fermi expansion and thus a corresponding reduction of the kinetic energy. We suspect that kinetic energy serves as the primary perturbation from exact reversal in this regime, and that the interaction effects are simply encoded in a changing initial state. While this is a more trivial interaction-induced effect, eventually for large enough  $a$  we see that  $F$  begins to decrease. We interpret this as a crossover between kinetic energy and interactions being the dominant deviation from perfect time-reversal, and thus this latter regime we take as an actual many-body effect on QKR Loschmidt echo. In Fig. 5.10B, we show how the fidelity decays with increasing number of kicks  $N$  in the Loschmidt protocol, and indeed find that at the larger interaction strengths the fidelity appears to decay faster (though eventually saturating at some non-zero value). Here the fidelities are extracted by performing a double Gaussian fit around the central mode, with a narrower Gaussian counting atom remaining in the zero-momentum condensate and a broader one counting a scattered fraction. In Fig. 5.10 we plot the population in the narrower Gaussian, though this will systematically tend to reduce the fidelity; further details on such systematics are discussed in the supplementary of [3]. Extracting an accurate measure of the many-body Lyapunov exponent is an interesting direction for future work.

Closely related to the concept of Loschmidt echo is the out-of-time-ordered correlator (OTOC). The OTOC is instead defined by

$$F' = \langle \psi | \hat{W}_t^\dagger \hat{V}^\dagger \hat{W}_t \hat{V} | \psi \rangle. \quad (5.16)$$

Here I'll take  $\hat{V}$  and  $\hat{W}$  to be local unitary operators (though one can consider Hermitian and/or global operators as well), and  $\hat{W}_t = \hat{U}_t^\dagger \hat{W} \hat{U}_t$ . Essentially, this defines an experiment where we act upon the initial state with  $\hat{V}$ , then propagate forward in time to act with  $\hat{W}$ , then propagate back in time to act with  $\hat{V}^\dagger$ , then propagate forward in

time to act with  $\hat{W}^\dagger$  and finally propagate back and measure the overlap with the initial state. For  $\hat{V}$  and  $\hat{W}$  being local operations, these operators should commute for no time-propagation and the initial fidelity should be unity. However, if there are interactions between the local degrees of freedom, then the local operator will spread outward from its initial starting point over the system, which is a process formally described by the Heisenberg representation  $\hat{V}(t) = \hat{U}^\dagger \hat{V} \hat{U}$ . As both  $\hat{V}$  and  $\hat{W}$  spread, eventually they may overlap and fail to commute, causing  $F$  to decay from 1. This tells us deeply about the rate at which information propagates through a many-body quantum system, as well as how local quantum information (which famously cannot be destroyed) is eventually “lost” in the sense of being inaccessible due to scrambling across the large number of degrees of freedom in a many-body system. OTOCs are an extremely rich subject which I am not an expert in, but a good starting reference for the discussion here is [116]. I’ll note here that OTOCs in the context of QKR have been theoretically studied in looking at out-of-time momentum correlations for the purpose of understanding Lyapunov exponents [117]; this is another potential interesting area of future exploration, though here I’ll just outline some preliminary calculations framed more toward experimentally studying operator propagation in the single-particle spreading.

In the QKR framework, I will take the local degrees of freedom as the discrete momentum modes excited by the kicking. One possibility for local operations on these momentum modes is simply applying a phase. That is here I will consider the operations

$$\hat{V} = e^{-i\varphi_1|0\rangle\langle 0|} \quad (5.17)$$

$$\hat{W} = e^{-i\varphi_2|k_0\rangle\langle k_0|}. \quad (5.18)$$

Here  $\varphi_1$  and  $\varphi_2$  are the phases we will apply to the 0 and  $k_0$  momentum modes respectively. Once again we need to work on resonance in order to perform time-reversal

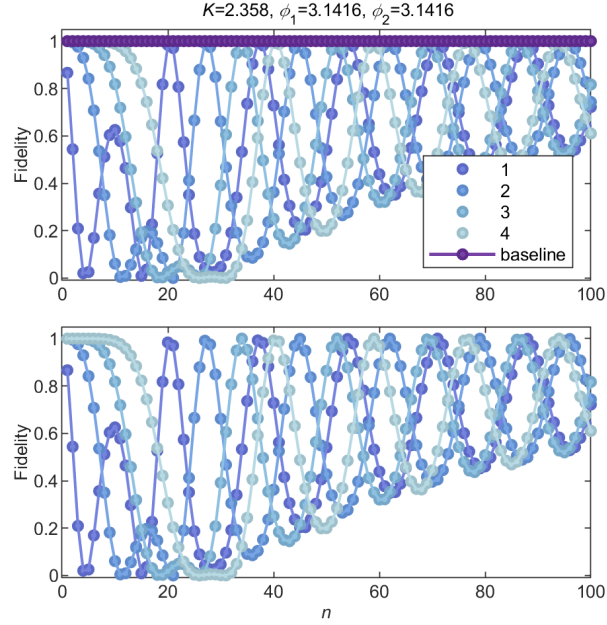


Figure 5.11: Numerically simulated OTOC scheme (both panels are the same here). The markers are the simulated points, and the lines are from Eq. (5.19). The legend labels  $k_0$ , and baseline is a run where no pulses are applied, confirming that the result is trivially unity for the perfect scenario of an initial 0 momentum plane wave under reversal kicking protocol. Plotted here is actually  $F'^2$ .

operations. It turns out if we consider a perfect plane-wave initial state  $|\psi\rangle = |0\rangle$ , we can straightforwardly derive a result for  $F'$  after  $n$ -kicks given by

$$F'_n = 1 + 4 \left( e^{-i\varphi_1} - 1 \right) \sin^2 \left( \frac{\varphi_2}{2} \right) \mathcal{J}_{k_0}^2 \left( nK/\bar{k} \right) \left[ 1 - \mathcal{J}_{k_0}^2 \left( nK/\bar{k} \right) \right]. \quad (5.19)$$

Here  $\mathcal{J}_{k_0}$  is a Bessel function of order  $k_0$ . I derive this in detail Appendix C. There are a few checks to make sure this form makes sense. First is there is a leading term 1 which we expect the formula to reduce to if we make the problem trivial in anyway. One trivial case is to not kick  $K = 0$ ; since I consider  $k_0 \neq 1$  then  $J_{k_0}(0) = 0$  and so we get  $F'_n = 1$ . Similarly, if I either make  $\varphi_1$  ( $\varphi_2$ ) equal to 0, then  $\hat{V}$  ( $\hat{W}$ ) becomes an identity operator which always commutes, and then we see that  $F'_n = 1$ . On the other hand, we expect the biggest signal if we apply the maximum phase of  $\pi$ , and indeed

we see that the amplitude of the Bessel function oscillation will be largest for such a  $\pi$ -phase shift. Because we are looking at how operators that are separated by  $k_0$  sites, it makes sense that the oscillations are governed by Bessel functions of order  $k_0$ , and these Bessel functions are to the second and fourth power corresponding to interference across multiple legs of the forward and backward time propagation. To these last couple point, I do believe it is a bit of a result of the fact that we start with the initial  $|0\rangle$  state, and if instead an arbitrary superposition is considered then I believe different order Bessel functions should emerge.

I benchmark this analytical formula with numerical calculation in Fig. 5.11. The results match essentially perfectly (error on the order  $10^{-16}$ ), which is expected since Eq. (5.19) is an exact result. Ultimately the goal is to realize a similar measurement in experiment. Here, utilizing techniques of momentum space lattices [118] will likely be critical for implementing these local momentum site operations. In Fig. 5.12, I show the effects of momentum spread on the described OTOC protocol. The first major point is that the fidelity decays rapidly even in the case that either  $\hat{V}$  or  $\hat{W}$  because then the system is undergoing an imperfect Loschmidt echo due to the kinetic energy. To correct the remaining results for this effect, we normalize the actual OTOC fidelity curves to the baseline Loschmidt curve as done in a recent experiment [119]. Indeed this restore the early time dynamics to be quite similar to the prediction of the simple theory. We do see however that the speed of information propagation in the system does seem to slow down (at least initially), as indicated by the fact that the numerics lag behind the analytic prediction in terms of their initial departure from unity. However, eventually this normalization procedure appears to totally breakdown and the remaining points seem to go all over the place, even surpassing the maximum physical fidelity value of 1.

The indication of Fig. 5.12 is promising if one can achieve a sufficiently cold sample. However while in Fig. 5.12 the OTOC fidelity  $F'$  itself was averaged, in our experiment

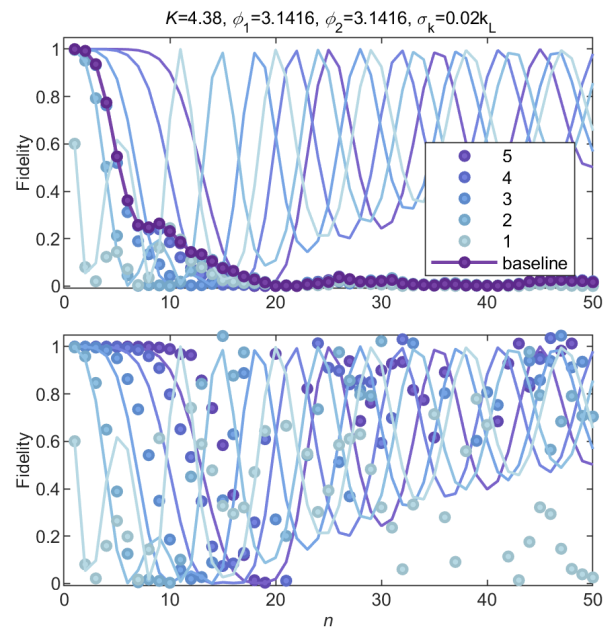


Figure 5.12: Numerically simulated OTOC scheme averaged over a Gaussian ensemble of quasimomentum. The numerical data (markers) in the top plot is directly measured, and in the bottom plot is normalized to the baseline run. The solid lines are still from Eq. (5.19). Plotted here is actually  $F'^2$ .

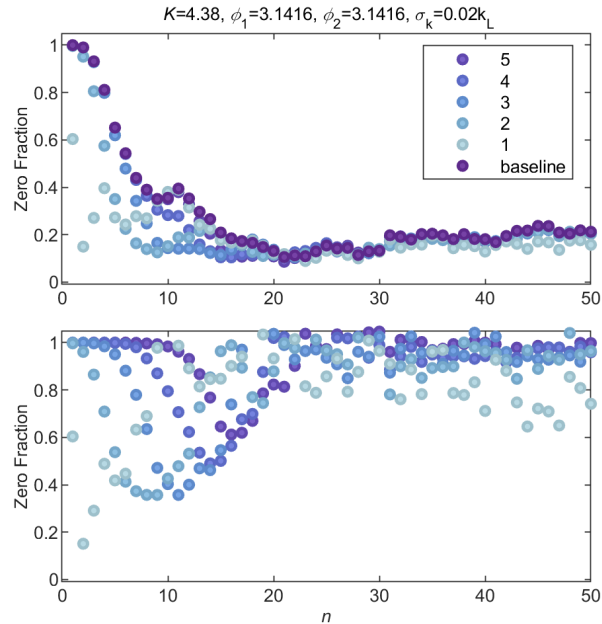


Figure 5.13: Numerically simulated OTOC scheme averaged over a Gaussian ensemble of quasimomentum. The numerical data (markers) in the top plot is directly measured, and in the bottom plot is normalized to the baseline run. The solid lines are still from Eq. (5.19).

one really only has access to a density which gives information about  $F'^2$ . To model this, we should instead perform a quasimomentum average over  $F^2$ . This is done in Fig. 5.13. We indeed find that such an averaging procedure produces a result which follows the analytic form much less, but nevertheless indicates that it takes time for the operator information to spread through the system as evidenced by the different initial departure times from unity for the varying  $k_0$ . Ultimately this shows that it should be possible to measure some notion of operator spreading in the QKR time reversal experiments.

These calculations serve as just the very simple entrance into the realm of OTOCs for this experiment. An ultimate goal of course would be to investigate scrambling at the many-body level which is not shown here at all, but as a first step experimentally reproducing the above numerical calculations would be great progress. Ultimately, one may also want to study this sort of physics experimentally away from the regime of

quantum resonance, for instance trying to obtain a new probe of an MBDL state. It's not so clear whether such a thing might be achievable in these kicked cold atom set-ups where the reversal procedure already fails. In the next section, I will discuss mappings of QKR to spin chains which may offer alternative insights into exploring these possibilities.

## 5.5 Many-body Dynamical Localization (MBDL) in Kicked XXZ Chains

To conclude this chapter, I will briefly conclude with some theoretical/numerical investigations of 1D kicked spin chains. Given the novelty of potentially realizing an MBDL state which stabilizes interacting driven matter without any disorder, it makes sense to explore different potential models for realizing such physics, especially models which may make connections with systems away from the traditional QKR experiments of quantum gases in pulsed optical lattices. It was theoretically noted previously that the single and few-particle QKR dynamics had a connection to an XXZ spin chain kicked by a quadratic magnetic field [120, 121]. As a brief review, the XXZ spin chain is defined by

$$H_{\text{XXZ}} = J \sum_j (S_j^x S_{j+1}^x + S_j^y S_{j+1}^y + \Delta S_j^z S_{j+1}^z) \quad (5.20)$$

$$= J \sum_j \left( \frac{1}{2} [S_j^+ S_{j+1}^- + \text{h.c.}] + \Delta S_j^z S_{j+1}^z \right). \quad (5.21)$$

This a generalized version of the traditional Heisenberg model  $\sum_j \mathbf{S}_j \cdot \mathbf{S}_{j+1}$ , where an anisotropy parameter  $\Delta$  control the relative coupling between the  $z$ -direction with respect to the other two. The XX interaction represents a spin-flip process between nearest-neighbor spins. Here I'll consider the spin-1/2 case with  $S^{x,y,z} = \sigma^{x,y,z}/2$  where  $\sigma$  indicates

the Pauli-matrices. In the limit  $\Delta = 0$ , it is known that a Jordan-Wigner transformation converts this into a noninteracting fermion problem [122]. Roughly, spin-ups correspond to the presence of a fermion and the raising and lowering operators become annihilation and creation operators (though in detail one has to consider non-local string operators which counts the number of spin-flips to the left of the current site). In the single spin-flip/particle case, it is then clear that the XX interactions play a similar role to the lattice kicking in the single-particle QKR; the former hops spin-flips between spatial sites, and the latter hops the particle from momentum site to momentum site.

To bring in the equivalent of kinetic energy, we add in a quadratic magnetic field. In particular, we will consider the following Floquet map

$$U_{\text{kickedXXZ}} = e^{-i\mathbf{k}H_{\text{quad}}/4} e^{-iKH_{\text{XXZ}}/4\mathbf{k}} \quad (5.22)$$

$$H_{\text{quad}} = \sum_{j=(1-L)/2}^{(L-1)/2} (j + \beta)^2 \sigma_j^z \quad (5.23)$$

$$H_{\text{XXZ}} = \sum_{j=(1-L)/2}^{(L-1)/2} (\sigma_j^x \sigma_{j+1}^x + \sigma_j^y \sigma_{j+1}^y + \Delta \sigma_j^z \sigma_{j+1}^z). \quad (5.24)$$

Here  $L$  is the length of the chain,  $\beta$  plays the role of quasimomenta (which also helps eliminate a reflection symmetry about the chain center), and  $\mathbf{k}$  and  $K$  are used as model coefficients for comparison with QKR. The evolution conserves the total magnetization  $M = \langle \sum_j \sigma_j^z \rangle$ , and thus sectors with different  $M$  evolve independently from each other. To study this model, we rely on exact diagonalization methods on modest system sizes up to  $L = 14$ . These proceed straightforwardly by explicitly constructing the relevant Hamiltonians, computing their matrix exponential, multiplying to get the Floquet operator and then using Matlab's diagonalization package. Time-dynamics can be computed by repeated iteration of the Floquet operator. Throughout we consider open boundary conditions. We take  $L$  to be even or odd depending on the circumstance.

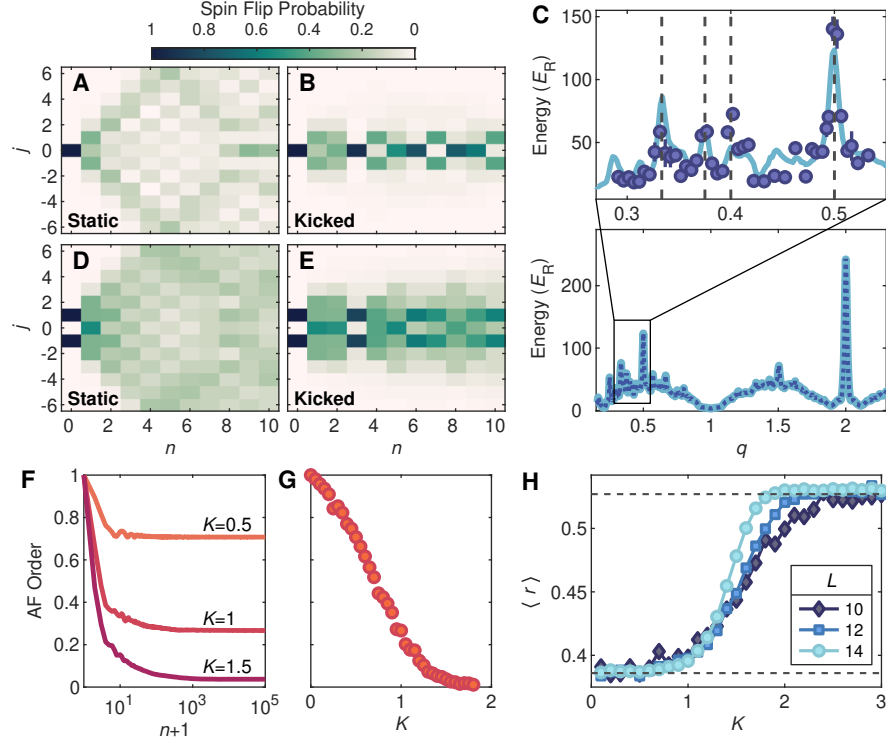


Figure 5.14: **Kicked-rotor dynamics and many-body dynamical localization in kicked spin chains.** (A-B) Calculated single-spin-flip evolution for static and kicked spin-1/2 XXX chains of length  $L = 13$  for  $K = 2.4$ ,  $\bar{k} = 1.5$  and  $\beta = 0$ . (C) Spin chain quantum resonance spectroscopy (solid) demonstrating equivalence to QKR (dashed) in the single spin-flip sector with  $K = 3\bar{k}$ ,  $L = 51$  and averaging over a Gaussian ensemble of  $\beta$ . Energy is after 10 kicks. Zoomed-in panel compares experimental measurements on the atomic quantum kicked rotor to predictions of spin chain numerics. Dashed vertical lines indicate  $q = 1/3, 3/8, 2/5$ , and  $1/2$ . (D-E) The same as A-B but with 2 spin flips. (F) Time average of the staggered magnetization  $\langle \sum_j (-1)^j \sigma_j^z \rangle / L$  versus kick number, starting from an initial Néel state with  $\bar{k} = 1$ ,  $L = 12$ ,  $\beta = 0.1$  and varying  $K$ . (G) Staggered magnetization in the infinite-time limit versus  $K$ , for the same parameters as panel F. (H) Gap-ratio statistic of the  $M = 0$  sector at  $\bar{k} = 1$  for varying  $L$  averaged over 100 values of  $\beta$ . Dashed lines indicate predictions of the Poisson ( $\langle r \rangle \approx 0.386$ ) and circular-orthogonal ensemble ( $\langle r \rangle \approx 0.527$ ) [123].

In Fig. 5.14, we examine the kicked XXX chain where  $\Delta = 1$ . Working first in the single spin-flip sector  $M = 1 - L/2$ , we see in Figs. 5.14A-C the phenomena of dynamical localization and quantum resonance clearly, and in fact the correspondence is exact up to boundary effects [120]. In the inset, we take an experimental point of view and compare the numerically computed spin-chain fractional resonances with our experimental data, where we see good agreement. In Figs. 5.14D-E, we similarly show the evolution of 2 spin-flips ( $M = 2 - L/2$ ) which also demonstrates a localization behavior in contrast to the case without kicking.

Moving into the many-body regime, we consider the  $M = 0$  sector where there are  $L/2$  spin flips ( $L$  even), corresponding to the same number of interacting Jordan-Wigner fermions. A standard protocol that has emerged in the experimental study of MBL is to prepare an initial Néel state (or charge density wave in the language of particles) where each site has an alternating spin direction  $|\psi\rangle = |\uparrow\downarrow\uparrow\downarrow\dots\rangle$ . In a thermal, delocalized phase, one expects the anti-ferromagnetic ordering/pattern to be destroyed during evolution; if it persists, then one takes this as a signature of some type of many-body non-ergodicity. The anti-ferromagnetic order parameter is  $AF = \langle \sum_j (-1)^j \sigma_j^z \rangle / L$ , which is 1 for the Néel state and is expected to decay to 0 in a thermalized state. We plot the evolution of the time average of this observable out to  $n = 10^5$  in Fig. 5.14G, where for sufficiently small  $K$  the order persists at a substantial nonzero value. The time average of an observable  $O$  is straightforwardly defined as  $\langle O \rangle_n = \left( \sum_{i=1}^n \langle \psi | U_{\text{kickedXXZ}}^{\dagger i} O U_{\text{kickedXXZ}}^i | \psi \rangle \right) / n$ . The long-time limit can be computed from the diagonal ensemble as  $\lim_{n \rightarrow \infty} \langle O \rangle_n = \sum_{\alpha} |c_{\alpha}|^2 \langle \psi_{\alpha} | O | \psi_{\alpha} \rangle$ . Here  $c_{\alpha} = \langle \psi_{\alpha} | \psi \rangle$  are the coefficient of the initial state  $|\psi\rangle$  in the basis of the many-body Floquet states  $|\psi_{\alpha}\rangle$  obtained from diagonalization of the Floquet map  $U_{\text{kickedXXZ}}$  [124]. We confirmed that for this set of parameters, the long-time limit agreed with the time-averaged value at around  $n = 10^4$ .

A traditional and more theoretical probe of an MBL state is the use of the gap-ratio statistic  $\langle r \rangle$  [73, 123]. This is defined as  $r_\alpha = \min(\delta_\alpha, \delta_{\alpha+1}) / \max(\delta_\alpha, \delta_{\alpha+1})$ , where  $\delta_\alpha = \epsilon_{\alpha+1} - \epsilon_\alpha$  is the quasi-energy gap and  $\epsilon_\alpha$  are the quasi-energies. It is important that the  $\epsilon_\alpha$  are ordered in the interval  $[-\pi, \pi]$  prior to extracting the gaps and gap-ratios. To compute  $\langle r \rangle$  in Fig. 5.14G, we average  $r_\alpha$  over the  $M = 0$  sector as well as for 100 values of  $\beta$  drawn from a normal distribution of standard deviation 0.1. We see that it undergoes a transition from an integrable Poissonian value at small interactions  $K$  to the thermal prediction of Gaussian/circular orthogonal ensembles. Indeed we see that as the system size is scaled up, the transition between these two plateaus gets sharper but remains at a finite value. A detailed finite-size scaling analysis remains to be performed to extract the critical properties of this transition, but this is a great indication that an MBDL state should exist in this model of XXZ spin chains kicked by a quadratic magnetic field. Other possibilities for future work include simulating more specific models which may be realized in a number of other quantum simulator platforms [125, 126, 127].

# Appendix A

## Numerical TDSE Simulation with Time-Splitting Spectral Methods

In this appendix, I will discuss a common technique for simulating the time evolution of the Schrodinger (and Gross-Pitaevskii) equation. The method is called time-splitting, pseudospectral (TSSP) method and is useful for its ease of implementation. This technique was useful for many of the numerical simulations shown throughout this thesis (and many others not shown), and at the end of this appendix I will show some calculations for the planned interferometry experiments. I wrote a separate guide which outlines the technique along with code which can be found in my Citadel folder under the path `theorynumerics/integrators/TDSEtutorial.mlx`. A detailed review of GPE solving techniques is given in [128]. One can also look at the following publications from the numerical integration packages WavePacket and GPESLab for additional discussions [129, 130].

## A.1 Time-Splitting Spectral Integration

Our goal is to calculate  $\psi(x, t)$  obeying either time-dependent Schrodinger or Gross-Pitaevskii equations given in (2.11) and (2.9). For any numerical solution, we need to discretize both space and time. We assume we are given an initial condition  $\psi(x, t_0)$ , and then our times are just defined as  $t_n = t_0 + ns$  for integer  $n$  and small time step  $s$ ; we will discuss what constitutes small later. We similarly define a spatial mesh of width  $L$  and spacing  $h$  such that the positions are located at  $x_j = x_0 + jh$  with  $x_N - x_0 = L$  for some integer  $N$ . In this chapter I will stick to 1 spatial dimension. For multiple spatial dimensions one should of course define higher dimensional meshes, but no different in form than what we have already defined for  $x$ . The complexity of generalizing a specific integration routine to higher dimensions often depends on the specific algorithm, but for TSSP it is trivial. For TSSP, we will also employ periodic boundary conditions

$$\psi(x_0) = \psi(x_L). \quad (\text{A.1})$$

This means that we have  $N$  points in our spatial mesh. Our initial condition defines

$$\psi_j^0 = \psi(x_j, t_0). \quad (\text{A.2})$$

Throughout the subscript denotes the spatial coordinate and the superscript the time coordinate. The problem of numerically integrating differential equations comes down to figuring out how to treat derivatives. For the time-derivative, we know the general solution for a time-dependent Hamiltonian is given by

$$\psi(t) = \mathcal{T} \exp\left(-\frac{i}{\hbar} \int_{t_0}^t H(t') dt'\right) \psi(t_0). \quad (\text{A.3})$$

Here  $\mathcal{T}$  denotes time-ordering. For a time-independent problem, the integral is trivial. However, the challenge is typically computing a matrix exponential for  $H$  which will involve non-commuting position and momentum operators. This necessarily forces us to approximate and consider breaking up the evolution into a bunch of small time-steps. In the case of time-dependent Hamiltonian, we have to break up the time-integration anyway. Thus instead of (A.3), our problem in time-discretized form becomes

$$\psi^{n+1} = \exp\left(-\frac{i}{\hbar} \int_{t_0}^{t_0+s} H(t') dt'\right) \psi^n \quad (\text{A.4})$$

Here since  $s$  is small, we can use standard approximations for the numerical integration and the problem becomes more or less about repeated matrix multiplication. To proceed, it becomes useful to decide how we will handle the spatial derivatives in  $H$ . The two simplest methods are finite-difference and Fourier transform. Before proceeding to TSSP which uses the latter, I think it is instructive to discuss the former. Finite difference roughly just means using the discrete approximation to the derivative

$$\left. \frac{\partial \psi}{\partial x} \right|_{x=x_j} \rightarrow \frac{\psi_{j+1} - \psi_j}{h} \quad (\text{A.5})$$

For the second derivative, we have

$$\left. \frac{\partial^2 \psi}{\partial x^2} \right|_{x=x_j} \rightarrow \frac{\psi_{j+1} - 2\psi_j + \psi_{j-1}}{h^2}. \quad (\text{A.6})$$

The Hamiltonian in the position basis can be expressed explicitly as a tridiagonal matrix with

$$H_{\text{FD}}(t) = \begin{pmatrix} \frac{\hbar^2}{mh^2} + V_{j-1}(t) & -\frac{\hbar^2}{2mh^2} & 0 & \dots \\ -\frac{\hbar^2}{2mh^2} & \frac{\hbar^2}{mh^2} + V_j(t) & -\frac{\hbar^2}{2mh^2} & \ddots \\ 0 & -\frac{\hbar^2}{2mh^2} & \frac{\hbar^2}{mh^2} + V_{j+1}(t) & \ddots \\ \vdots & \ddots & \ddots & \ddots \end{pmatrix} \quad (\text{A.7})$$

This is an  $N - 1 \times N - 1$  matrix (based on how I defined the grid, one should let  $j$  run from 1 to  $N - 1$ ) and supports solutions with Dirichlet boundary conditions; for periodic boundary conditions, one has an  $N \times N$  matrix by adding a row/column for either  $j = 0$  or  $j = N$  and adding a factor  $-\hbar^2/2mh^2$  on the top right and bottom left corner entries. For really large matrices, it can still be challenging to matrix exponentiate (A.7) despite its tridiagonal nature. The simplest approximation for (A.4) expanding the exponential to first order and using a midpoint approximation on the integral is then

$$\psi^{n+1} = \left( 1 - \frac{i}{\hbar} H_{\text{FD}}^{n+1/2} s \right) \psi^n. \quad (\text{A.8})$$

Recall  $H_{\text{FD}}^n$  is a 2D matrix and  $\psi^n$  is a 1D vector. This is the so-called Forward Euler method (alternatively one might see the term forward-time centered-difference or FTCS), but it should basically never be used since it is well-known to be unconditionally unstable, something that can easily be shown using Von Neumann stability analysis [131]. An alternative is to instead evolve the equation backward

$$\left( 1 + \frac{i}{\hbar} H_{\text{FD}}^{n+1/2} s \right) \psi^{n+1} = \psi^n. \quad (\text{A.9})$$

This is stable but obviously not unitary (doesn't preserve normalization). What one resorts to then to resolve this is combining the two methods in the midpoint Crank-Nicolson which is given by

$$\left(1 + \frac{i}{\hbar} H_{\text{FD}}^{n+1/2} \frac{s}{2}\right) \psi^{n+1} = \left(1 - \frac{i}{\hbar} H_{\text{FD}}^{n+1/2} \frac{s}{2}\right) \psi^n. \quad (\text{A.10})$$

With the use of the finite-difference representation for the Hamiltonian, this is called Crank-Nicolson Finite Difference method (CNFD). This is a semi-implicit, semi-explicit method. Namely at one step we explicitly evolve forward in time by matrix multiplication (forward-Euler), and in the second step we have to implicitly solve a matrix equation (backward-Euler). Explicit methods are nice because they tend to be easier to implement in practice and the steps are less computationally complex, however they typically require smaller time-steps for stability. Implicit methods are typically harder to implement and solve at each step since you need to solve a system of equations, but they have the benefit of allowing for longer time steps. For the backwards Euler step, I typically use Matlab's simple backslash command for solving linear systems. The generalization of CNFD to GPE is not trivial (specifically the CN discretization is complicated by the nonlinearity) and as far as I know inferior to TSSP (discussed below) in most relevant cases to us. Before that, a final important note about integration schemes using the finite-difference method is the Courant-Friedrichs-Lewy (CFL) condition. Its related to causality and basically limits the propagation of numerical information on the mesh to some characteristic "speed" in the wave equation. My understanding is that normally one does this for hyperbolic PDE's of which the Schrodinger equation is not, but one can nevertheless derive a similar condition for stable propagation [132]

$$\frac{\hbar^2}{s} \geq \frac{2\hbar}{m}. \quad (\text{A.11})$$

Now we move onto spectral split-step methods (TSSP) which utilize two main ideas. The first is solving a derivative equation by spectral/Fourier transform. Under Fourier transform, a derivative becomes multiplication of an imaginary quantity. So the kinetic energy term of the Hamiltonian maps as

$$-\frac{\hbar^2}{2m} \frac{\partial^2 \psi}{\partial x^2} \rightarrow \frac{\hbar^2 k^2}{2m} \tilde{\psi}. \quad (\text{A.12})$$

Here  $\tilde{\psi}$  denotes the Fourier transform of the position space wavefunction  $\psi$ . Hopefully this is a familiar result from introductory quantum mechanics. On its own, this isn't immediately helpful because this just shifts the problem to the potential energy terms. The second part of TSSP is then time-splitting, where we split the evolution of the Hamiltonian into different steps for the kinetic and potential energy. This is based on the Baker-Campbell-Hausdorff (BCH) formula

$$e^X e^Y = e^Z, \quad Z = X + Y + \frac{1}{2} [X, Y] + \frac{1}{12} [X, [X, Y]] + \dots \quad (\text{A.13})$$

For our problem,  $X$  is the kinetic energy term (multiplied by the time step) and  $Y$  is the potential energy term (integrated over the time step). It is clear that all the higher order commutator terms are of size  $\mathcal{O}(s^2)$ . Thus for small enough time-step  $s$ , we have the first-order Lie splitting

$$\exp\left(-\frac{i}{\hbar} \int_{t_0}^{t_0+s} H(t') dt'\right) \approx \exp\left(-\frac{i}{\hbar} \frac{p^2}{2m} s\right) \exp\left(-\frac{i}{\hbar} \int_{t_0}^{t_0+s} V(x, t') dt'\right). \quad (\text{A.14})$$

In between applications of these operators, we can take Fourier transforms to move between position and momentum space so that the operators are diagonal. The problem can be solved completely explicitly. The first order algorithm is given in space-time

discretized form by

$$\phi_j = \exp\left(-\frac{i}{\hbar}V_j^{n+1/2}s\right)\psi_j^n \quad (\text{A.15})$$

$$\tilde{\psi}_l^{n+1} = \exp\left(-i\frac{\hbar k_l^2}{2m}s\right)\tilde{\phi}_l. \quad (\text{A.16})$$

Here  $\phi$  is just an intermediate vector in the time-splitting and tilde's denote discrete Fourier transform. As a clarification, TSSP really refers to discrete sine transforms rather than complex exponentials so I'm abusing terminology a bit, but for relevant cases I would almost always recommend using exponentials over sines unless there are physical reasons to impose hard-wall boundary conditions. After (A.16), an inverse Fourier transform is of course needed to start the next step. One can implement these Fourier transforms trivially with any standard FFT package (using FFT assumes periodic boundary condition). We also require defining a momentum grid  $k$  as well. For a review of discrete Fourier transforms see [133]. The  $N$ -point meshes for periodic boundary conditions and a spatial grid spacing  $h$  is given by

$$x_j = x_0 + jh, \quad x_N - x_0 = L \quad (\text{A.17})$$

$$k_l = -\frac{\pi}{h} + \frac{2\pi}{N}l, \quad k_N - k_0 = \frac{2\pi}{h}. \quad (\text{A.18})$$

Here I assume  $N$  is even, and specifically FFT tends to perform fastest for  $N = 2^M$  with integer  $M$ .  $j$  and  $l$  are both integers, which can be taken to run from 0 to  $N - 1$  or 1 to  $N$  (because of periodic boundary conditions); this means one should avoid duplicating  $x_0(k_0)$  and  $x_N(k_N)$  in the meshes. The latter choice fits well with MATLAB indexing.  $x_0$  is a free choice (this is fine by Fourier transform shift theorem), but typically one takes the momentum mesh to be symmetric about 0. Finally, one last thing to keep in mind is that when one takes a Fourier transform, the ordering of the resulting vector will be

from  $N/2$  to  $N - 1$  and then 0 to  $N/2 - 1$ . The easiest thing to do is to apply the `fftshift` function to the  $k$  vector.

The algorithm in (A.15) and (A.16) is the lowest-order splitting which is only first-order in time. Typically for GPE equation, it is better to use the second-order Strang splitting, which only requires one extra diagonal matrix multiplication (or vector element-wise multiplication). The algorithm splits the position evolution further into two steps surrounding the momentum evolution. I will write it here explicitly for GPE equation with interaction coefficient  $g$ :

$$\phi_j = \exp\left[-\frac{i}{\hbar}\left(V_j^{n+1/4} + g|\psi_j^n|^2\right)\frac{s}{2}\right]\psi_j^n \quad (\text{A.19})$$

$$\tilde{\xi}_l = \exp\left(-i\frac{\hbar k_l^2}{2m}s\right)\tilde{\phi}_l \quad (\text{A.20})$$

$$\psi_j^{n+1} = \exp\left[-\frac{i}{\hbar}\left(V_j^{n+3/4} + g|\xi_j|^2\right)\frac{s}{2}\right]\xi_j. \quad (\text{A.21})$$

This Strang splitting method is unconditionally stable, spectral order in space and 2nd order in time. It preserves normalization by construction and many other important properties except for energy at the discretized level [128]. For TDSE, just set  $g = 0$ . In higher dimensions, the generalization is trivial and just requires changing the state vectors to higher dimensional arrays; the steps are still just element-wise multiplication and fast Fourier transforms. In higher dimensions, memory costs become problematic but this is a generic issue for any algorithm.

## A.2 Floquet-Bloch Atom Interferometry

A major upcoming experiment these techniques have allowed us to begin understanding quantitatively is continuously-trapped atom interferometry with Floquet-Bloch

bands. For an example of the potential that trapping in lattices provides for enhancing interferometer sensitivity, see [134]. The idea for Floquet-Bloch interferometry is similar to previous work with Bloch oscillations coupling the lowest two sub-bands of a bichromatic superlattice [135]; a theoretical discussion of the concept can be found in [136]. The scheme falls under the category of Landau-Zener-Stuckelberg(-Majorana) (LZS) interferometry, and the general theoretical overview can be found in [137, 138]. The idea is to take a two level system and perform a parameter sweep such that the levels repeatedly cross, leading to repeated Landau-Zener tunneling events which produce an interferometric signal in the level populations. The prototypical example is a two-level atom in an AC field with the detuning sinusoidally modulated.

In the context of optical lattices, periodicity of the band structure in quasimomentum allows Bloch oscillations to accomplish LZS interferometry; in practice though, a force that couples the lowest band gap will couple every other gap as well, and so generically the problem needs to be modified to see Stuckelberg interferometry. In the case of [135], appropriately adjusting the superlattice can produce two well-isolated bands. For our experiment, we can in principle use the Floquet band gap engineering discussed in section 3.2 to engineer a similar situation where there are only two relevant bands.

The first step to such a Floquet-Bloch interferometer was already demonstrated in section 3.2, namely coherent, controllable beam-splitting of an atomic wavepacket into two spatially-separated bands. Choosing a modulation index which splits the wavepacket fairly evenly and then continuing the experiment for a second half Bloch period would ultimately allow for demonstration of interference using Floquet-Bloch-Zener beam-splitting. By varying a parameter in the region between the two resonantly coupled quasimomenta, one should be able to observe a fringe in the relative population between the two bands after the recombination event. From a modeling perspective, the cleanest way to do this would be to turn off the force when the atoms reach the Brillouin zone edge

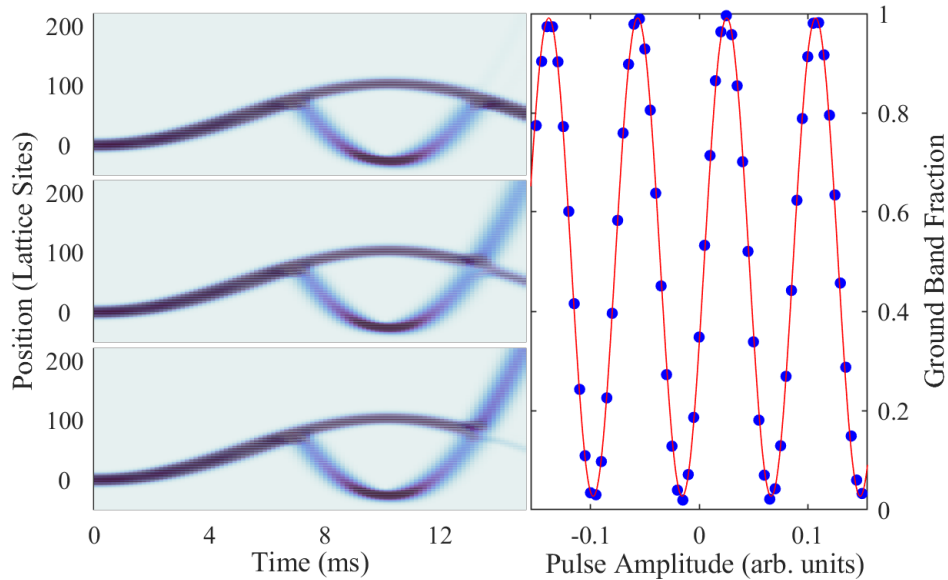


Figure A.1: Simulated Floquet-Bloch-Zener-Stuckelberg interference measurement. The three left panels show evolution of the squared wavefunction for three different values of the amplitude of a force pulse

for a variable hold time  $t_{\text{hold}}$ , at which the phase would just wind with respect to  $t_{\text{hold}}$  at a frequency given by the static lattice band gap. Unfortunately because our experiments force is generated by a harmonic potential and the wavepackets must be spatially separated, this is challenging to do nicely.

An alternative is to apply a small change in the applied force, an experiment which would begin to more closely mimic one of the ultimate goals of such an interferometer as a force sensor. By varying the amplitude of the pulse, one can in principle precisely compute the expected phase winding by integrating the difference in band energies over the quasimomentum traversed over the course of the pulse. The concept is demonstrated in figure A.1, where a Floquet-Bloch interferometer with a spatially homogeneous force and applied force pulse is simulated. On the left, we can qualitatively observe a strong change in the output band populations by varying the amplitude of the force pulse and imaging in position space. The fringe is shown on the right, with a near-unity contrast for a fairly realistic initial cloud spread. In this case the solid red line is a simple sinusoidal

fit, though one could in principle attempt to track both the change in phase due to the pulse as well as potential accumulation of Stuckelberg phases at the Landau-Zener transition points. This could be important for real applications of the interferometer, but not so much in a proof-of-concept experiment demonstrating phase coherence of the beam-splitting operations.

Ultimately a critical challenge for the current experimental setup is that the force is not spatially uniform. Within the concept of a scheme as illustrated in figure A.1, this will rapidly degrade the contrast as one tries to attain larger sensitivity by increasing enclosed space-time area as the different band populations will not reach the recombination point at the same instant. Within the context of a proof-of-concept, it is likely ideal to simply seek large lattice depths where the band motion is minimal and then band-map to read out. Real application likely require either upgrading the magnetic forcing architecture to apply homogeneous forces (anti-Helmholtz pairs), switching to a uniform field and utilize accelerating lattice techniques, or finding interferometer loops which eliminate the differential shifts of the two bands. One such loop can be accomplished by coupling to the second excited band as shown in [18]; the atoms transfer to an equal and opposite force on the opposing side of the harmonic trap, and if the drive sequence is engineered so that both arms make this transfer then there will be multiple wavepackets reaching the recombination point at exactly the same time.

# Appendix B

## Fringe Removal for Absorption Images

In this appendix, I discuss techniques for reducing fringes in our cold atom absorption images. This had been previously implemented with a slightly different algorithm, but we recently found this method to be unreliable and incredibly slow for larger data sets with hundreds of images (taking around 10 minutes to process). The “new” algorithm is now able to achieve similar or better fringe removal while taking only around a second of processing time for comparably sized image libraries. Actually when I implemented my own version of the “old” algorithm, the time taken was not substantially different, and so it is possible that there is just extreme inefficiency in the image processing code of the old database. Either way, I believe the new algorithm produces marginally better results and so it is the current state-of-the-art on the  $^7\text{Li}$  experiment.

Good references on the technique are given in [139, 140, 141]. I will mainly follow [140]. A Matlab live script demonstrating this technique can be found in my folder in the Citadel under fringe.removal (avoid running it because it requires being on the same path as the data).

## B.1 Absorption Imaging

First, let us briefly review absorption imaging. To image an atom cloud, we subject it to a resonant laser pulse which eventually hits the camera sensor. The atoms effectively leave a shadow on the image seen on the camera. We call this the picture with atoms (PWA). If one had a perfectly homogeneous beam intensity, then it would be fairly easy to extract a value proportional to the atomic density from this single PWA. Namely, denoting the intensity of the PWA as  $I_{\text{PWA}}(x, y)$ , we have from Beer's Law

$$I_{\text{PWA}}(x, y) \sim e^{-OD(x,y)}. \quad (\text{B.1})$$

Here  $OD$  denotes the optical density, which is the atomic column density multiplied by a constant scattering cross section. In reality, the beam suffers from significant imperfections and aberrations on its path to the camera, which makes it quite hard to systematically and reliably extract the atomic density. In (B.1), this means there is some arbitrary prefactor with unknown  $(x, y)$  dependence which makes inverting for  $n_c$  essentially impossible.

To solve this, we employ absorption imaging where a second image is taken shortly after the atoms are no longer present in the beam path; this is called the picture without atoms (PWOA). The intensity of the PWOA measured on the camera should only differ by the Beer's law absorption factor in (B.1) so that if we divide the two we find

$$\frac{I_{\text{PWA}}(x, y)}{I_{\text{PWOA}}(x, y)} = e^{-OD(x,y)}. \quad (\text{B.2})$$

The idea of absorption imaging is then that two successive images with and without the atoms allows us to cleanly eliminate any noise in the imaging beam to measure the atomic density.

The last problem we account for is the possibility of the camera measuring light even when the laser is off due to dark currents. So after the PWOA, we take a final image called the dark image where not even the imaging beam is on. Since these dark currents supposedly equally effect the PWA and PWOA, we extract the OD experimentally as

$$OD(x, y) = -\ln \left[ \frac{I_{\text{PWA}}(x, y) - I_{\text{dark}}(x, y)}{I_{\text{PWOA}}(x, y) - I_{\text{dark}}(x, y)} \right] = -\ln \left[ \frac{A(x, y)}{R(x, y)} \right]. \quad (\text{B.3})$$

From here on out, I will just refer to the dark-subtracted PWA  $A$  and PWOA  $R$ . This is the basis of absorption imaging and how we extract all our data about the atomic cloud. Note this method should precisely eliminate all the inherent imperfections in the imaging laser. What it fails to account for though is slight deviations in the imaging beam from PWA to PWOA, for instance due to say mechanical drift slightly altering the beam path. This should be clear from the assumptions in writing down (B.2) being that the images only differed by the absorption factor. Ultimately, it is these fringes that arise from shot-to-shot instability in the imaging beam that we will try to eliminate with post-image processing techniques.

## B.2 Ideal Reference Fringe Removal Algorithm

The idea for fringe removal is that given a set of many PWOAs (say taken over the course of a long data set), we can construct for each PWA an ideal reference PWOA that minimizes the presence of fringes in the final OD by taking linear superpositions of the images in our original set. Let's first briefly go over the intuition. We might imagine that the imaging beam on any given shot is an average intensity profile with just a few main modes of variation causing fringes (which we further suppose can only vary linearly from shot-to-shot in the sense that the fringe amplitude can change but cannot

for instance translate). These variations can be present in both the PWAs and PWOAs. By compiling a large library of PWOAs, we can potentially capture all the major modes for beam intensity variation; we call these basis images. If our set of basis images span some linear vector space containing all the major possible fringes, we should ideally be able to subtract them away (this is just the essence of linear algebra). Our goal is then to just determine an algorithm for identifying the best linear combination of basis images to match each PWA.

The one major question is what if the fringes aren't linearly related to some small basis set? Then indeed the exactness of the argument presented above breaks down, and we really need an arbitrarily large set of PWOA basis images to get rid of an arbitrary variety of different fringes. This is always the case to some degree, but for the most part we can still capture a lot of the dominant fringes in our reasonably sized bases and clean up the images quite nicely in spite of this.

Let us now explore the algorithm which is just a simple least-squares regression. From taking data, we have a collection of reference PWOA images. Rather than having each reference be a 2D matrix over position  $x$  and  $y$ , we suppose that we have flattened each into a 1D vector with pixels indexed by say  $i$ ; we stack up these reference images into a 2D matrix  $R_{i,j}$  which denotes the  $i$ th pixel in the  $j$ th reference PWOA. The ordering of the pixels just need to be consistent for different reference images; the ordering of the images is totally arbitrary. Our goal is to construct for each PWA vector  $A$  an idealized reference image/vector  $R'$  which takes the form

$$R'_i = \sum_j R_{i,j} c_j. \quad (\text{B.4})$$

To determine the value of the  $c_j$ , we use a fairly standard condition that the idealized reference  $R'$  should minimize the least-squares difference with the desired PWA  $A$ . There

is a huge problem with the condition on its own, namely that our signal which is the presence of atoms produces a large discrepancy which we do not want to minimize. This forces us to minimize the quantity

$$f = \sum_i m_i (A_i - R'_i)^2, \quad (\text{B.5})$$

where  $m_i$  denotes a mask which is 0 in regions where we know atoms are and 1 everywhere else. Ultimately, we can only account for low-frequency fringes which are well-correlated over large spatial distances (at least order of cloud size if not longer). To do this for each reference image weight  $c_j$ , we have the condition

$$\frac{\partial f}{\partial c_j} = 2 \sum_i m_i \left( A_i - \sum_k R_{i,k} c_k \right) R_{i,j} = 0. \quad (\text{B.6})$$

Defining  $B_{j,k} = \sum_i m_i R_{i,j} R_{i,k}$ , we see that we have to solve the linear equation

$$\sum_k B_{j,k} c_k = \sum_i m_i R_{i,j} A_i. \quad (\text{B.7})$$

Everything in this equation is known exactly other than  $c_k$ , so one can solve by computing the singular value decomposition (SVD) of  $B$  which allows one to construct the Moore-Penrose pseudoinverse. There are a number of pre-packaged ways to do this in Matlab. It's also fine to use Matlab's `lsqminnorm` which sometimes performs faster. Moreover, by stacking the PWAs  $A$  together into a matrix just as we did for the references  $R$ , the entire computation can be done at once without looping. Once the  $c_j$  are found, the  $R'$  are trivially constructed and (B.3) can be re-used replacing  $R \rightarrow R'$ .

An example of the fringe removal is shown in figure B.1. The top row displays raw images which feature strong fringe as can be seen in the wavy features prominent in the background. The middle row contains the fringe-removed images using the technique

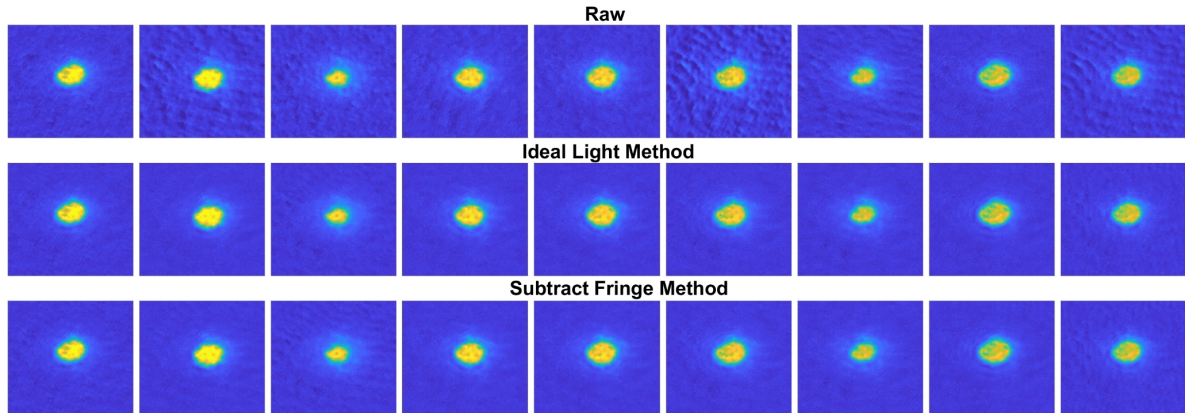


Figure B.1: Example of fringe removal on BEC absorption images. Top row are raw images computed from (B.3). Middle row contains fringe removed images obtained from the ideal reference light method that results from solving (B.7). The improvement in the image quality is blatantly evident. The third row is obtained from the former fringe removal algorithm implemented in the lab which attempts to subtract away the fringes from each PWA-PWOA pair.

discussed in this section. In this case, the data set was 44 images large (44 each of PWA, PWOA and dark) and the computation on my laptop took less than a quarter second. The improvement in the image noise is substantial and qualitatively apparent. The background optical density is clearly a lot more smooth and the atomic density is completely preserved. This becomes extremely important for experiments where the atoms become highly spread out and the ratio between peak density of the clouds and the amplitude of background fluctuations is not  $\gg 1$ .

In the last row I show similarly fringe removed images using the formerly employed technique on the  $^7\text{Li}$  experiment. It also involves trying to achieve an ideal reference image, but instead of constructing the ideal reference image from an in principle arbitrary superposition of the reference set (for instance the PWOA initially associated with that PWA can have 0 weight in the constructed reference), it tries to explicitly identify the fringes in the PWOA reference set and then appropriately subtract away the fringes from each PWA-PWOA pair. Overall, I would argue that the essence of the techniques

is largely the same.  $B$  is still a fundamental object in the latter calculation. If you subtract away the mean PWOA image from  $B$ , what you obtain is the covariance matrix of the masked reference set. The statement is then that the fringe basis vectors are exactly the singular vectors of the covariance matrix. Because both methods amount to this, they should take close to the same computational time. The only major difference in the methods is what to do with the SVD, which in the latter method involves some subtle arguments about the origin of the fringes to appropriately perform the subtraction. Ultimately I find that to make the latter algorithm inferior given what I believe to be rather comparable performance. Some more detail about the calculation can be found in the live script.

I want to quickly comment on principal component analysis (PCA). This is discussed in [141] as well as used in the old algorithm. PCA is an example of a low-rank approximation which is used to describe variation in data while reducing the dimension of the data linearly. The reason to use such a method goes back to the intuition discussed at the start of the section. If one suspects that most of the fringes can indeed be accounted for by just a few primary basis fringes, then we do not need to store a massive library of fringe vectors. When we compute the SVD, we can just keep the first “few” basis vectors which correspond to the largest singular values. Where to take this cut-off is a bit of an art rather than a science as far as I can tell. The rank reduction of PCA may be useful if it is ever decided that the best scenario is to keep a massive library of thousands of reference images. Within my limited tests in the scope of this fringe removal application, I did not observe any qualitative improvements by performing PCA or not.

One last interesting technique was implemented in [142]. The idea is that a primary nonlinear effect one might be worried about is translation of fringes by a pixel or two in any direction. Given that area scales as the square of the linear dimension length, it could require a lot of time to acquire enough images to account for all these small variations.

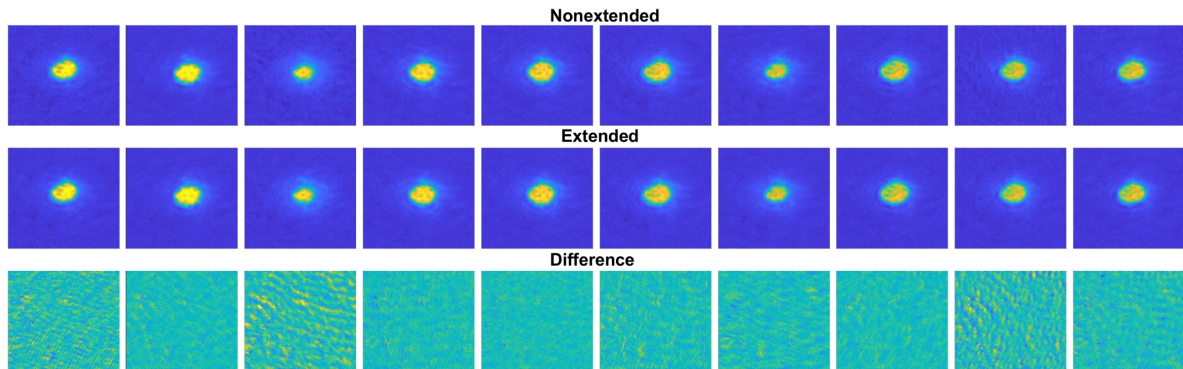


Figure B.2: Comparison of fringe removal for the normal and extended reference sets. Overall the improvement appears minor, but the extended set appears better when there are clearly fringes visible in the normal set. The third row shows the difference in optical density and makes this a bit more clear (OD scale is  $\pm 0.1$ ).

The idea is then to simulate these shifts by actually shifting the reference images by pixels one way or another to get a much larger, extended reference set. The same calculations can then be done with this extended set and the hope is to see a significant improvement.

Implementation for our data is shown in figure B.2. Qualitatively, it is clear that when the unextended reference set does a good job, the extended basis is almost identical. However it does seem that in the cases where fringes are still largely visible in the unextended basis, the extended basis does a good job further smoothing them over. While the improvement is minor and likely not critical for many applications in the group, it could be largely beneficial exactly in the cases where fringe removal itself is pivotal. Finally in figure B.3, a further comparison of the fringe removal methods is shown displaying the variation in OD of the background pixels. Indeed this plot confirms that the extended basis provides a slight improvement as compared to the plain fringe removal techniques with an unextended basis.

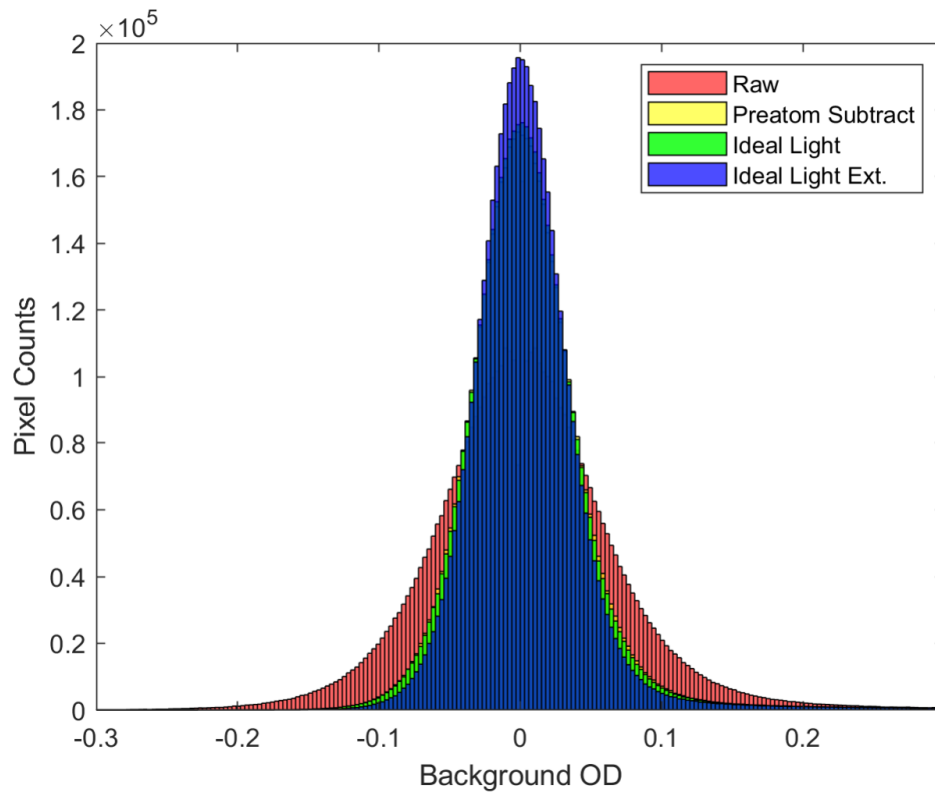


Figure B.3: Histograms of OD in the background region of absorption images for different fringe removal procedures. The raw clearly has the widest spread and thus the largest noise. Both the fringe subtraction and ideal reference construction method perform comparably. The extended basis indeed further reduces the noise.

# Appendix C

## Derivation of Ideal QKR OTOC

Here we want to calculate the kicked rotor OTOC exactly at quantum resonance  $\langle \hat{W}_t^\dagger \hat{V}^\dagger \hat{W}_t \hat{V} \rangle$  with

$$\hat{V} = e^{-i\phi_1|0\rangle\langle 0|} = 1 + (e^{-i\phi_1} - 1) |0\rangle\langle 0| \quad (\text{C.1})$$

$$\hat{W} = e^{-i\phi_2|k_0\rangle\langle k_0|} \quad (\text{C.2})$$

$$\hat{U}^n = e^{-inK \cos \hat{x}/\hbar} \quad (\text{C.3})$$

$$\hat{W}_t = \hat{U}^{n\dagger} \hat{W} \hat{U}^n. \quad (\text{C.4})$$

We'll consider the initial state  $|\psi_0\rangle = |0\rangle$ . I'll be using the Jacobi-Anger expansion

$$e^{iA \cos \hat{x}} |j\rangle = \sum_m i^m J_m(A) e^{im\hat{x}} |j\rangle = \sum_m i^m J_m(A) |j+m\rangle. \quad (\text{C.5})$$

Before beginning the calculation we should set some expectations. This OTOC tries to measure how two well-separated local unitaries,  $\hat{V}$  at site 0 and  $\hat{W}$  at site  $k_0$ , overlap and commute as a result of time-evolution under kicked rotor evolution at resonance ( $\hbar = 4\pi$ ) over  $n$ -kicks,  $\hat{U}^n$ . It will mean the operators remain completely commuting and

0 will mean the operators are non-commuting. Our answer should then reduce to 1 when  $n = 0$ . Further, if either  $\phi_1$  or  $\phi_2$  is 0, then either  $\hat{V}$  or  $\hat{W}$  is simply the identity and the OTOC must reduce to 1 at all times. Because these unitaries have a well-defined distance of  $k_0$  and because the coupling of sites at a fixed distance is governed by a Bessel function of order the distance as given by the above expansion, we expect the evolution to be dominated by terms of  $J_{k_0}(nK/\bar{k})$ . Naively we can expect these processes to enter at even orders depending on how many times in the 4 legs of propagation the operator traveled and understanding that pairs of legs need to "interfere" to produce an output (for instance how  $\hat{W}_t$  causes  $\hat{V}$  and  $\hat{V}^\dagger$  to not cancel).

Now we start the calculation. The application of the first  $\hat{V}$  operator  $\hat{V}$  on the initial state is trivial since it ends up just contributing a global phase, i.e.  $\hat{V}|0\rangle \sim |0\rangle$  which I

will add back in at the end. Then we have

$$\hat{W}_t \hat{V} |0\rangle = e^{inK \cos \hat{x}/\hbar} e^{-i\phi_2 |k_0\rangle \langle k_0|} \sum_m i^m J_m(-nK/\hbar) |m\rangle \quad (\text{C.6})$$

$$= e^{inK \cos \hat{x}/\hbar} \left[ \sum_m i^m J_m(-nK/\hbar) |m\rangle + i^{k_0} (e^{-i\phi_2} - 1) J_{k_0}(-nK/\hbar) |k_0\rangle \right] \quad (\text{C.7})$$

$$= \sum_{r,m} i^{m+r} J_m(-nK/\hbar) J_r(nK/\hbar) |m+r\rangle \quad (\text{C.8})$$

$$+ i^{k_0} (e^{-i\phi_2} - 1) J_{k_0}(-nK/\hbar) \sum_r i^r J_r(nK/\hbar) |k_0+r\rangle$$

$$= \sum_l i^l \left( \sum_m J_m(-nK/\hbar) J_{l-m}(nK/\hbar) \right) |l\rangle \quad (\text{C.9})$$

$$+ i^{k_0} (e^{-i\phi_2} - 1) J_{k_0}(-nK/\hbar) \sum_r i^r J_r(nK/\hbar) |k_0+r\rangle$$

$$= \sum_l i^l J_l(0) |l\rangle + i^{k_0} (e^{-i\phi_2} - 1) J_{k_0}(-nK/\hbar) \sum_r i^r J_r(nK/\hbar) |k_0+r\rangle \quad (\text{C.10})$$

$$= \sum_l i^l \delta_{l,0} |l\rangle + i^{k_0} (e^{-i\phi_2} - 1) J_{k_0}(-nK/\hbar) \sum_r i^r J_r(nK/\hbar) |k_0+r\rangle \quad (\text{C.11})$$

$$= |0\rangle + i^{k_0} (e^{-i\phi_2} - 1) J_{k_0}(-nK/\hbar) \sum_r i^r J_r(nK/\hbar) |k_0+r\rangle \quad (\text{C.12})$$

$$= |0\rangle + (e^{-i\phi_2} - 1) J_{k_0}(-nK/\hbar) \sum_r i^r J_{r-k_0}(nK/\hbar) |r\rangle. \quad (\text{C.13})$$

Clearly, this makes sense; if we set  $\phi_2 = 0$ , the second term vanishes and we have perfectly echoed the state. Now applying  $\hat{V}^\dagger$

$$\hat{V}^\dagger \hat{W}_t \hat{V} |0\rangle = [e^{i\phi_1} + (e^{i\phi_1} - 1) (e^{-i\phi_2} - 1) J_{k_0}^2(nK/\hbar)] |0\rangle$$

$$+ (e^{-i\phi_2} - 1) J_{k_0}(-nK/\hbar) \sum_r i^r J_{r-k_0}(nK/\hbar) |r\rangle. \quad (\text{C.14})$$

I'll slowly calculate  $\hat{W}_t$  one step at a time. First applying a forward time evolution

$$\begin{aligned} \hat{U}^n \hat{V}^\dagger \hat{W}_t \hat{V} |0\rangle &= [e^{i\phi_1} + (e^{i\phi_1} - 1) (e^{-i\phi_2} - 1) J_{k_0}^2(nK/\bar{k})] \sum_m i^m J_m(-nK/\bar{k}) |m\rangle + \\ &\quad (e^{-i\phi_2} - 1) J_{k_0}(-nK/\bar{k}) \sum_{r,m} i^{r+m} J_{r-k_0}(nK/\bar{k}) J_m(-nK/\bar{k}) |r+m\rangle. \end{aligned} \quad (\text{C.15})$$

Using the same trick to go from (8) to (12) we have

$$\begin{aligned} \hat{U}^{n\dagger} \hat{V}^\dagger \hat{W}_t \hat{V} |0\rangle &= [e^{i\phi_1} + (e^{i\phi_1} - 1) (e^{-i\phi_2} - 1) J_{k_0}^2(nK/\bar{k})] \sum_m i^m J_m(-nK/\bar{k}) |m\rangle \\ &\quad + (e^{-i\phi_2} - 1) J_{k_0}(-nK/\bar{k}) i^{k_0} |k_0\rangle. \end{aligned} \quad (\text{C.16})$$

Next we have

$$\hat{W}_t^\dagger \hat{U}^{n\dagger} \hat{V}^\dagger \hat{W}_t \hat{V} |0\rangle = [e^{i\phi_1} + (e^{i\phi_1} - 1) (e^{-i\phi_2} - 1) J_{k_0}^2(nK/\bar{k})] \sum_m i^m J_m(-nK/\bar{k}) |m\rangle + i^{k_0} C |k_0\rangle \quad (\text{C.17})$$

$$C = [(1 - e^{i\phi_1}) (1 - e^{i\phi_2}) + 2 (e^{i\phi_1} - 1) (1 - \cos \phi_2) J_{k_0}^2(nK/\bar{k})] J_{k_0}(-nK/\bar{k}). \quad (\text{C.18})$$

Finally applying the last  $\hat{U}^{n\dagger}$ ,

$$\hat{W}_t^\dagger \hat{V}^\dagger \hat{W}_t \hat{V} |0\rangle = [e^{i\phi_1} + (e^{i\phi_1} - 1) (e^{-i\phi_2} - 1) J_{k_0}^2(nK/\bar{k})] |0\rangle + C \sum_m i^{k_0+m} J_m(nK/\bar{k}) |k_0+m\rangle. \quad (\text{C.19})$$

Finally, we can arrive at the OTOC result by looking for the  $|0\rangle$  amplitude (I will multiply

by  $e^{-i\phi_1}$  to recover the phase from the initial  $\hat{V}$  action):

$$\langle \hat{W}_t^\dagger \hat{V}^\dagger \hat{W}_t \hat{V} \rangle = \langle 0 | \hat{W}_t^\dagger \hat{V}^\dagger \hat{W}_t \hat{V} | 0 \rangle \quad (\text{C.20})$$

$$= 1 + (1 - e^{-i\phi_1}) (e^{-i\phi_2} - 1) J_{k_0}^2(nK/\bar{k}) + e^{-i\phi_1} C J_{-k_0}(nK/\bar{k}). \quad (\text{C.21})$$

Once again, we can see that the baseline case with no butterfly operator  $\phi_2 = 0$  yields just the first term and thus perfect time-reversal regardless of the choice in  $\phi_1$ ; the same happens if instead  $\phi_1 = 0$  as well. If we plug in  $C$  we get

$$\langle \hat{W}_t^\dagger \hat{V}^\dagger \hat{W}_t \hat{V} \rangle = 1 + 2(1 - e^{-i\phi_1}) (\cos \phi_2 - 1) J_{k_0}^2(nK/\bar{k}) + 2(1 - e^{-i\phi_1}) (1 - \cos \phi_2) J_{k_0}^4(nK/\bar{k}). \quad (\text{C.22})$$

Finally using the trig identity  $2 \sin^2 x = 1 - \cos(2x)$ , we have

$$\langle \hat{W}_t^\dagger \hat{V}^\dagger \hat{W}_t \hat{V} \rangle = 1 + 4(e^{-i\phi_1} - 1) \sin^2\left(\frac{\phi_2}{2}\right) J_{k_0}^2(nK/\bar{k}) [1 - J_{k_0}^2(nK/\bar{k})]. \quad (\text{C.23})$$

# Appendix D

## Probing non-exponential decay in Floquet-Bloch bands (preprint)

This appendix contains the arXiv version of the non-exponential decay work discussed in Chapter 3.

## Probing non-exponential decay in Floquet-Bloch bands

Alec Cao, Cora J. Fujiwara, Roshan Sajjad, Ethan Q. Simmons, Eva Lindroth, and David Weld\*

**Abstract:** Exponential decay laws describe systems ranging from unstable nuclei to fluorescent molecules, in which the probability of jumping to a lower-energy state in any given time interval is static and history-independent. These decays, involving only a metastable state and fluctuations of the quantum vacuum, are the most fundamental nonequilibrium process, and provide a microscopic model for the origins of irreversibility. Despite the fact that the apparently universal exponential decay law has been precisely tested in a variety of physical systems [1], it is a surprising truth that quantum mechanics *requires* that spontaneous decay processes have non-exponential time dependence at both very short and very long times [2, 3]. Cold-atom experiments both classic [4] and recent [5] have proven to be powerful probes of fundamental decay processes; in this paper, we propose the use of Bose condensates in Floquet-Bloch bands as a probe of long-time non-exponential decay in single isolated emitters. We identify a range of parameters that should enable observation of long-time deviations, and experimentally demonstrate a key element of the scheme: tunable decay between quasienergy bands in a driven optical lattice.

**Keywords:** ultracold atoms, nonequilibrium dynamics, spontaneous decay, non-Markovian dynamics.

## 1 Introduction

Given the ubiquity of exponential decay, it is surprising that quantum mechanics requires that decay processes to a continuum with a ground state exhibit non-exponential long-time dynamics [2, 3, 6–9]. Classic experiments on the subject include negative results from studies of  $^{56}\text{Mn}$  nuclear decay tests [1] and an indirect observation claimed in investigations of  $^8\text{Be}$  scattering phase shifts [10]. More recently, a variety of physical systems ranging from integrated photonics [11] to Feshbach molecules [12] have emerged as platforms for the exploration of non-exponential decay. Extensive

\* Corresponding author: **David Weld, Alec Cao, Cora J. Fujiwara, Roshan Sajjad, Ethan Q. Simmons:** Physics Department, University of California, Santa Barbara, CA USA. **Eva Lindroth:** Department of Physics, Stockholm University, AlbaNova University Center, Stockholm, Sweden.

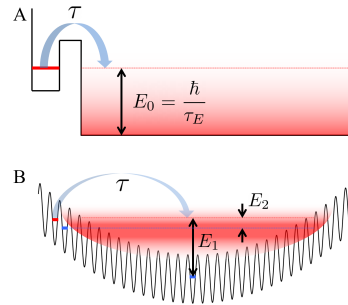


**Figure 1:** A) Schematic of a potential in which non-exponential decay is expected.  $\tau$  is the decay time of the exponential part of the tunneling process, and  $\tau_E = \hbar/E_0$  is the timescale associated with the energy of the decay product. B) Schematic of proposed optical lattice experiment probing non-exponential decay.  $E_1$  and  $E_2$  are different possible characterizations of the decay product energy.

theoretical work has been directed toward non-exponential decay of autoionizing resonances in atomic systems [13–15] and laser-induced ionization effects [16, 17], though this remains at the frontier of experimental feasibility.

Negative ions are often considered in this context, in part due to their simple structure: there is usually only one bound state and a few resonances which simplify the study of laser-induced negative ion photodetachment [16]. Another reason [3, 15] is the possibility of finding broad resonances decaying with a very small energy release which, as discussed below, should result in a deviation at an earlier time when more is left of the parent. On the experimental side however, negative ions also pose certain difficulties, especially due to the low target densities available. To our knowledge, no experiments on non-exponential decay in negative ions have been reported.

In a very different physical context, cold atoms in optical lattices can also serve as a probe of decay dynamics [18], as shown for example in two seminal experiments. The quantum Zeno effect was first detected using cold sodium atoms in an accelerated optical lattice [4]; more recently, non-Markovian long-time dynamics were observed in an optically dense ensemble of lattice-trapped atoms driven by

an applied microwave field [5, 19]. These results demonstrate the promise of degenerate gases in optical lattices for observing long time modifications to memoryless exponential decay in an ensemble of single emitters.

Here we propose the use of ultracold non-interacting  $^7\text{Li}$  Bloch oscillating in a tilted modulated optical lattice to directly observe long-time non-exponential interband decay. A schematic of the proposed setup and its relationship to an idealized decay process is presented in Figure 1. While the proposed experiments can in principle be performed in unmodulated lattices (in close analogy to Ref. [4] and to pioneering experiments in optical lattice Stückelberg interferometry [20]), we will show that signatures of non-exponential long-time evolution can be greatly enhanced using recently developed tools of Floquet engineering for modification and mapping of band structure [21, 22].

The proposed platform for the exploration of non-exponential decay has several unique advantages. Most important is the extreme tunability afforded by the use of flexible Floquet engineering techniques. Another key advantage, arising from the choice of atomic species, is the presence of broadly Feshbach-tunable interactions in  $^7\text{Li}$ . In this work we emphasize the ability to access the single-emitter regime by tuning the scattering length to zero. However, the ability to work at arbitrary scattering length may also enable future systematic study of the effects of interactions on spontaneous decay.

In Section 2 of this manuscript, we review a heuristic explanation for non-exponential decay based on a simple analysis of the survival probability and the Breit-Wigner energy distribution. We present numerical calculations of the emergence of non-exponential behavior as a result of imposing a lowest energy bound, revealing decay rate and decay energy as key parameters for experimental observation. In Section 3, we discuss the details and feasibility of the proposed experiment. In particular we experimentally demonstrate the use of Floquet engineering to engineer the band gap and tune the decay rate, a key step on the path to realization of long-time non-exponential decay of an isolated emitter. Section 4 offers conclusions and outlook.

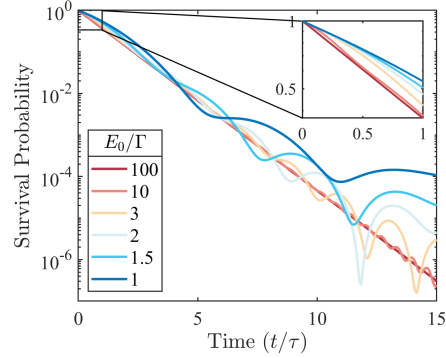


**Figure 2:** Emergence of non-exponential decay due to truncation of the energy distribution. The survival probability is plotted versus time for various values of  $E_0$ , as indicated in the legend. The ground state energy is set to 0.  $\hbar$  is set to 1 with time measured in lifetimes  $\tau$  and energy in linewidths  $\Gamma$ . The inset highlights the largest deviations in the first lifetime.

## 2 Origins of non-exponential decay

We begin by recalling a heuristic argument for non-exponential decay which makes no reference to the particular form of the unstable state or decay mechanism [8]. Given some initial state  $|\psi_0\rangle$  with Hamiltonian  $H$ , the survival or undecayed amplitude  $A(t)$  can be calculated as the overlap of the initial state with the time evolved state  $\exp(-iHt/\hbar)|\psi_0\rangle$ . For a continuous spectrum, the time evolved state can be expanded over the complete set of energy eigenstates  $|\phi_E\rangle$  as

$$e^{-iHt/\hbar}|\psi_0\rangle = \int dE |\phi_E\rangle \langle\phi_E|\psi_0\rangle e^{-iEt/\hbar}. \quad (1)$$

Taking the overlap of Eq. 1 with  $|\psi_0\rangle$  and recognizing the initial density of states as  $\rho(E) = |\langle\phi_E|\psi_0\rangle|^2$ , the survival amplitude is the Fourier transform

$$A(t) = \int_{-\infty}^{\infty} dE \rho(E) e^{-iEt/\hbar}. \quad (2)$$

The survival probability is  $A^2$ . A simple assumed form for the energy distribution  $\rho(E)$  is a Lorentzian or Breit-Wigner distribution:

$$\rho(E) = \frac{\Gamma}{2\pi} \frac{1}{(E - E_0)^2 + (\frac{\Gamma}{2})^2}, \quad (3)$$

where  $E_0$  is the mode and  $\Gamma$  is the linewidth. Inserting Eq. 3 into Eq. 2 and squaring yields the familiar result of exponentially decaying survival probability with decay rate  $1/\tau = \Gamma/\hbar$ .

*Non-exponential* decay at long times arises from including in this simple argument the fact that real systems necessarily have a lowest energy state, requiring either a truncation of  $\rho(E)$  or a bounding of the integral in Eq. 2 from below. This alters the form of the survival probability from a pure exponential, giving rise to corrections at long time scales. Fig. 2 shows the non-exponential population dynamics which result from imposing such a lower energy bound. The absolute square of  $A(t)$  is plotted for varying values of the decay product energy  $E_0$ , demonstrating a clear change from almost purely exponential behavior when  $E_0$  is many linewidths away from the ground state to large oscillations and strongly non-exponential dynamics for small values of  $E_0$ . Here the ground state energy is set to 0. This slower than exponential decay at very long times is well understood theoretically [8, 23], but poses a major challenge for experimental observation due to the small scale of the deviations (note the logarithmic  $y$  axis of Fig. 2) and the many half-lives elapsed before their onset. However, the inset of Fig. 2 reveals that significant non-exponential behavior arises even within the first lifetime when the truncation occurs within a few linewidths of the distribution peak. The scale of these deviations is on the order of 10%, which should be readily accessible to detection.

It is instructive to compare these results to the prediction of Ref. [3] that the timescale  $\tau_L$  for long time deviations is approximately given by

$$\tau_L \simeq 3\tau \log(E_0\tau/\hbar) = 3\tau \log(E_0/\Gamma), \quad (4)$$

where  $E_0$  is the energy released in the decay. Intuitively, this indicates that  $\tau_L/\tau$  (or  $E_0/\Gamma$ ) cannot be much larger than unity in order for there to be a significant remaining population to exhibit non-exponential behavior. In Fig. 3, we map out the numerical integration of Eq. 2 for the range of  $E_0/\Gamma = 0.2 - 10$ . We also plot the results of Eq. 4. While the prediction is qualitatively correct, for  $E_0/\Gamma \approx 2 - 3$  it somewhat overestimates the onset time; there is clear non-Markovian behavior even within the first time constant. Note the logarithmic scale of the color bar. Overall, though, Fig. 3 confirms the intuitive result of Eq. 4 that minimizing the decay product energy with respect

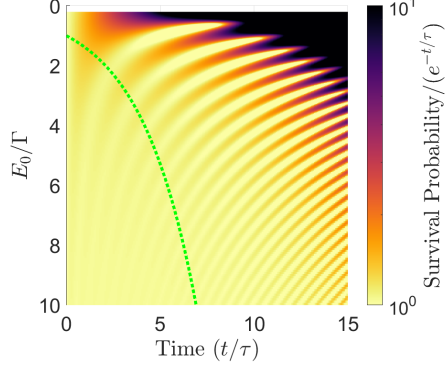


**Figure 3:** Non-exponential population dynamics as a function of time and the ratio  $E_0/\Gamma$ . Note that the survival probability color map is normalized to an exponential law in time, with black indicating an order of magnitude population excess with respect to the exponential decay prediction. Dotted green line is the prediction for the onset of non-exponential decay as given by Eq. 4.

to the decay rate yields the largest signal for non-exponential behavior.

In passing, we note that *short-time* deviations from exponential decay arise from a related but distinct mechanism: the finite expectation value of energy leading to a survival probability with initially vanishing time derivative [24]. This phenomenon underlies the quantum Zeno effect, which was also first realized experimentally with cold atoms [25].

### 3 Probing non-exponential decay in modulated optical lattices

The experimental probe of non-exponential decay we propose here is based on Bloch oscillations of an ultracold atom ensemble through partially avoided band crossings in modulated optical lattices. Our experimental platform consists of a Bose condensate of  $10^5$   $^7\text{Li}$  atoms in a far-red-detuned ( $\lambda = 1064$  nm) optical lattice. Interatomic interactions can be eliminated entirely using the shallow zero-crossing below  $^7\text{Li}$ 's broad magnetic Feshbach resonance [26]; this crucially allows us to probe the fundamental question of non-exponential decay of a single emitter. The lattice induces an energy band structure, shown in Figure 4, which can be probed with Bloch oscillations induced by

an applied tilt of the harmonic magnetic confinement. In fact the high tunneling rate of  ${}^7\text{Li}$  enables spatial resolving of different band populations *in situ* without the use of band maps or time-of-flight imaging [22]. Time-periodic modulation of the lattice depth enables the creation of hybridized Floquet-Bloch bands [21] with a drive-dependent band structure; as argued below this is a key capability for realistic observation of non-exponential decay.

We begin by considering the use of Bloch oscillations in an *undriven* lattice as a probe of decay dynamics. In such an experiment, the atoms are adiabatically loaded into the ground band of the lattice, then undergo Bloch oscillations due to the applied force from the inhomogeneous magnetic potential. Ignoring the field curvature, the main correction to the single-band approximation for the Wannier-Stark problem comes from tunneling between adjacent bands. As the atoms traverse the edge of the Brillouin zone, they have a chance to “decay” by tunneling across the first band gap once per Bloch cycle. The feasibility of observing long-time deviations from exponential decay in such an experiment can be quantitatively estimated using a Landau-Zener model of interband tunneling [27]. Semiclassically, the probability of tunneling across the  $n$ th band gap  $\Delta_n$  in a single Bloch cycle is

$$P_n = \exp\left[-\frac{\pi^2}{2} \frac{\Delta_n^2}{\hbar f_B \frac{\partial}{\partial q} |\mathcal{E}_n - \mathcal{E}_{n-1}|}\right], \quad (5)$$

where  $f_B$  is the Bloch frequency and  $\mathcal{E}_n$  is the dispersion of the  $n$ th band in the free particle limit, indexed with  $n = 0$  as the ground band. The derivative with respect to the undimensionalized quasimomentum ( $q = k/k_L$  and  $k_L = 2\pi/\lambda$ ) is evaluated at the point of avoided crossing. By modeling the decay as a discrete process happening once per Bloch cycle and then taking a continuum limit, the effective tunneling rate across the  $n$ th band gap is approximated as

$$\frac{1}{\tau} \approx f_B \log\left(\frac{1}{1 - P_n}\right). \quad (6)$$

In a shallow lattice, tunneling between all excited bands is large and we can treat them as a continuum, so we need only focus on tunneling across the first band gap. In calculating the probability  $P_1$  to tunnel out of the ground band, we have  $\frac{\partial}{\partial q} |\mathcal{E}_1 - \mathcal{E}_0| = 4 E_R$  evaluated at the Brillouin zone edge  $q = 1$ , where the recoil energy is  $E_R =$

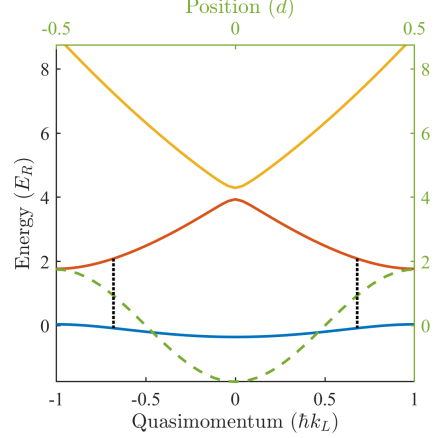


**Figure 4:** Band structure of a  $3.5 E_R$  deep undriven optical lattice. Solid lines are the lowest three energy bands. Dashed line overlays the lattice potential in position space (top axis). Dotted black line depicts the drive hybridization scheme used in Figure 5, ignoring coupling to higher bands.

$\hbar^2 k_L^2 / 2m$  with  $m = 7$  amu. Eqs. 5 and 6 reveal two important parameters for optimizing the decay rate of static Bloch oscillations: the band gap  $\Delta_1$  and the Bloch frequency  $f_B$ . These cannot be tuned arbitrarily, though the band gap is minimized for low lattice depths and the Bloch frequency is maximized for large magnetic field gradients. Our experiment can reliably achieve Bloch frequencies  $f_B \approx 100$  Hz and minimum usable lattice depths of around  $1 E_R$ , yielding  $\Delta_1 \approx 0.5 E_R$ . Inserting these values into Eqs. 5 and 6 reveals that the resulting tunneling probability will be minimal:  $P_1 \sim 10^{-5}$ , leading to a decay time  $\tau \sim 10^3$  s. Clearly more tunability is needed to reach a regime where the predicted long-time deviations from exponential decay can be observed. One route could be to use the much stronger gradients attainable in accelerating lattices, but this intrinsically limits the attainable measurement time as the atoms leave the region of interest. A more flexible possibility is the use of Floquet engineering to tune the bandgap.

Thus motivated, we consider the addition of time-periodic lattice depth modulation to the experimental protocol outlined above. Resonant coupling of two static bands by such a modulation generically creates a hybrid quasienergy band structure featuring at least one new gap, of a size

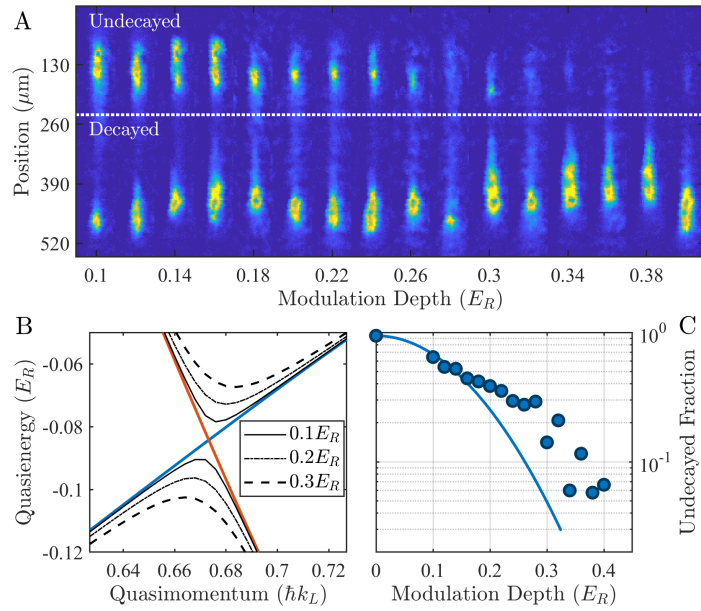


**Figure 5:** Experimental demonstration of Floquet-tunable decay. A) Images of a sample of cold lithium atoms after a single Landau-Zener tunneling event during a Bloch oscillation in a quasienergy band. The "undecayed" upper cloud are those that remain in the ground band of the corresponding undriven system. The lattice depth is  $3.5 E_R$ , the modulation frequency is 55 kHz, and the Bloch frequency is 27.8 Hz. B) Calculated quasienergy band structure around the avoided crossing for different modulation depths (indicated in legend). Note the drive-tunable gap. C) Undriven ground band fraction as a function of drive strength. Solid theory line is calculated from Eq. 5.

determined by drive strength rather than lattice depth [21]. Fig. 5B shows calculated quasienergy band structure near such a gap, for several different values of the drive strength. Tunneling across this tunable gap during a Bloch oscillation in a modulated lattice can realize a much more controllable decay process, in which the decay time can be tuned independently of lattice depth and potential tilt.

To demonstrate this central element of the proposed realization of non-exponential decay, we have experimentally measured tunable Landau-Zener decay in a Floquet-engineered quasienergy band structure. Fig. 5 presents an experimental measurement of the Landau-Zener decay probability of Eq. 5 across a Floquet-tunable band gap as a function of drive strength, for the case of resonant driving between the lowest two energy bands. Images of the two spatially resolved band populations after half a Bloch period in the amplitude modulated lattice are shown in panel 5A, and the calculated band crossing in the quasienergy picture is shown in panel 5B. The spatial separation between “decayed” and “undecayed” populations is a consequence of position-space Bloch oscillations in the two different band dispersions [22]. Plotting the fraction of undecayed atoms that remain in the ground band, we measure a tunable decay in qualitative agreement with the Landau-Zener tunneling theory of Eq. 5, as shown in panel 5B. Deviations of the data from theory may be the result of uncertainty in the lattice depth or inhomogeneity of the force. Note that in this case, it is actually the atoms that *fail* to undergo the tunneling event which correspond to the decayed population. To obtain a decay rate then, we must actually subtract Eq. 5 from 1. In any case, these results demonstrate the capacity to use lattice modulation to tune the tunneling probability over a wide range, including an enhancement of roughly four orders of magnitude over the tunneling probability in a static band for equivalent conditions. Crucially, this allows  $\Gamma$  to approach our achievable Bloch frequencies of up to 100 Hz, allowing for reasonable experimental run times and detectable non-exponential dynamics.

## 4 Conclusion

We have proposed a measurement of non-exponential decay of individual emitters which is based on interband tunneling of cold atoms dur-

ing a Bloch oscillation in a Floquet-engineered quasienergy band. A simple theoretical treatment of expected dynamics indicates that deviations from exponential decay should be measurable. Preliminary experimental tests of the proposed tunable decay mechanism demonstrate widely tunable decay rates and the feasibility of the underlying concept. These results lay the groundwork for realizing a new experimental probe of universal non-Markovian evolution, and open up new possibilities for exerting quantum control over an irreducible element of non-equilibrium quantum dynamics.

## Acknowledgements

We thank Andrey Kolovsky, Toshi Shimasaki, and Peter Dotti for useful discussions, and Jeremy Tanlimco and Jared Pagett for experimental assistance. EL acknowledges support from the Knut and Alice Wallenberg Foundation and from the Swedish Research Council (2016-03789). DW is grateful for hospitality provided by the guest researcher program of the Wallenberg Centre for Quantum Technology, and acknowledges support from the National Science Foundation (CAREER 1555313), the Army Research Office (PECASE W911NF1410154 and MURI W911NF1710323), and the University of California’s Multicampus Research Programs and Initiatives (MRP19-601445). DW and RS acknowledge support from the UCSB NSF Quantum Foundry through Q-AMASE-i program award DMR-1906325.

## References

- [1] E. B. Norman, S. B. Gazes, S. G. Crane, and D. A. Bennett, *Phys. Rev. Lett.* **60**, 2246 (1988).
- [2] J. J. Sakurai and J. Napolitano, *Modern Quantum Mechanics*, Addison-Wesley, 1994.
- [3] P. Greenland, *Nature* **335**, 298 EP (1988).
- [4] S. Wilkinson et al., *Nature* **387**, 575 (1997).
- [5] L. Krinner, M. Stewart, A. Pazmiño, J. Kwon, and D. Schneble, *Nature* **559**, 589 (2018).
- [6] L. Khalfin, *JETP* **6**, 1371 (1957).
- [7] R. Winter, *Phys. Rev.* **123**, 1503 (1961).

## NON-EXPONENTIAL DECAY IN FLOQUET-BLOCH BANDS

- [8] L. Fonda, G. C. Ghirardi, and A. Rimini, Reports on Progress in Physics **41**, 587 (1978).
- [9] P. Knight, Phys. Lett. A **61**, 25 (1997).
- [10] N. G. Kelkar, M. Nowakowski, and K. P. Khemchandani, Phys. Rev. C **70**, 024601 (2004).
- [11] A. Crespi et al., Phys. Rev. Lett. **122**, 130401 (2019).
- [12] F. Pepe, P. Facchi, Z. Kordi, and S. Pascazio, Phys. Rev. A **101**, 013632 (2020).
- [13] C. A. Nicolaides and D. R. Beck, Phys. Rev. Lett. **38**, 683 (1977).
- [14] S. Druger and M. Samuel, Phys. Rev. A **30**, 640 (1984).
- [15] C. A. Nicolaides and T. Mercouris, Journal of Physics B: Atomic, Molecular and Optical Physics **29**, 1151 (1996).
- [16] K. Rzazewski, M. Lewenstein, and J. H. Eberly, Journal of Physics B: Atomic and Molecular Physics **15**, L661 (1982).
- [17] A. M. Ishkhanyan and V. P. Krainov, Laser Physics Letters **12**, 046002 (2015).
- [18] M. Holthaus, Journal of Optics B: Quantum and Semiclassical Optics **2**, 589 (2000).
- [19] M. Stewart, L. Krinner, A. Pazmiño, and D. Schneble, Phys. Rev. A. **95**, 4512 (2017).
- [20] S. Kling, T. Salger, C. Grossert, and M. Weitz, Phys. Rev. Lett. **105**, 215301 (2010).
- [21] C. J. Fujiwara et al., Phys. Rev. Lett. **122**, 010402 (2019).
- [22] Z. A. Geiger et al., Phys. Rev. Lett. **120**, 213201 (2018).
- [23] K. Urbanowski, The European Physical Journal D **54**, 25 (2009).
- [24] L. Khal'fin, JETP **8**, 106 (1968).
- [25] M. Fischer, B. Gutiérrez-Medina, and M. Raizen, Phys. Rev. Lett. **87**, 040402 (2001).
- [26] S. E. Pollack et al., Phys. Rev. Lett. **102**, 090402 (2009).
- [27] M. Glück, A. R. Kolovsky, and H. J. Korsch, Physics Reports **366**, 103 (2002).

# Appendix E

## Transport controlled by Poincaré orbit topology in a driven inhomogeneous lattice gas (preprint)

This appendix contains the arXiv version of the Poincaré transport work discussed in Chapter 4.

Transport controlled by Poincaré orbit topology in a driven inhomogeneous lattice gas

Alec Cao, Roshan Sajjad, Ethan Q. Simmons, Cora J. Fujiwara, Toshihiko Shimasaki, and David M. Weld  
 Department of Physics, University of California, Santa Barbara, California 93106, USA

In periodic quantum systems which are both homogeneously tilted and driven, the interplay between drive and Bloch oscillations controls transport dynamics. Using a quantum gas in a modulated optical lattice, we show experimentally that inhomogeneity of the applied force leads to a rich new variety of dynamical behaviors controlled by the drive phase, from self-parametrically-modulated Bloch epicycles to adaptive driving of transport against a force gradient to modulation-enhanced monopole modes. Matching experimental observations to fit-parameter-free numerical predictions of time-dependent band theory, we show that these phenomena can be quantitatively understood as manifestations of an underlying inhomogeneity-induced phase space structure, in which topological classification of stroboscopic Poincaré orbits controls the transport dynamics.

Spatially periodic quantum systems exhibit an oscillatory response to static forces [1, 2]. Any applied modulation can interact with Bloch oscillations, resulting in phenomena ranging from super-Bloch dynamics [3] to high-harmonic generation [4]. In this work, we experimentally explore the consequences of breaking the position-independent character of Bloch oscillations with an inhomogeneous field, which qualitatively transforms the phase space structure of the system and generates an array of new transport phenomena. The recently-observed position-space character of Bloch oscillations [5] plays a key role, admixing an intrinsic self-parametric modulation to all Bloch oscillators.

The experiments we describe use a quantum gas in an optical lattice. Cold-atom experiments have long provided a flexible platform for exploring Bloch oscillations and related fundamental features of transport in crystals [3, 5–10]. Modulated effective electric fields have been used to investigate Wannier-Stark ladder resonances [11], modulation-assisted tunneling [12, 13], coherent spatial mode manipulation [14], and super Bloch oscillations [3], complementing related theoretical studies [15–20], and parametric lattice modulation has been applied to the study of quantum ratchet behavior [21] and large Floquet-Bloch oscillations in hybridized bands [22].

An overview of the experimental context of driven-lattice transport appears in Fig. 1: modulating the lattice depth near the Bloch frequency gives rise to an asymmetric parametrically-varying “convective” group velocity and net transport during a Bloch cycle. The experiments begin with an optically-trapped Bose-Einstein condensate (BEC) of  $10^5$   $^7\text{Li}$  atoms adiabatically loaded into a 1D optical lattice with lattice spacing  $d = 532$  nm, laser wave vector  $k_L = \pi/d$ , and recoil energy  $E_R = \hbar^2 k_L^2 / 2m$ , with  $m$  the mass of  $^7\text{Li}$ . Interatomic interactions are set to zero by Feshbach tuning. The condensate starts in the crossed optical dipole trap at a position away from the center of a harmonic potential created by external electromagnets, so that when the dipole trap beams are abruptly turned off the atoms feel an inhomogeneous force and begin Bloch oscillating. All comparisons with theory are based on a Gaussian ensemble of spatial width

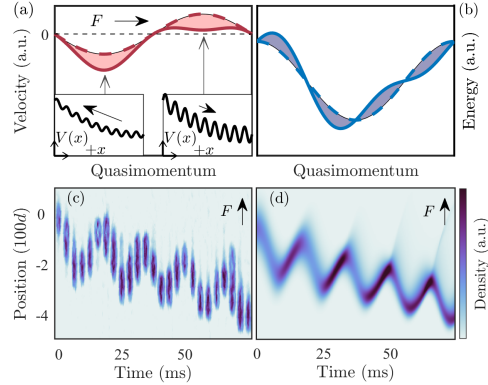


FIG. 1. Transport in a modulated lattice. (a) Comparison between convective (solid) and static (dashed) group velocity for a Bloch-oscillating ensemble with resonantly-modulated tunneling. Shaded area indicates net spatial motion over a cycle. Insets show exaggerated real-space potential, with tunneling indicated by the length and direction of the arrow. (b) Corresponding convective (solid) and static (dashed) energy bands. (c) Ordered sequence of absorption images demonstrating transport against an applied force by a chirped adaptive drive (details in text). (d) Theoretically predicted density evolution under the same conditions as (c).

$\sigma_x = 50d$  and momentum width  $\sigma_k = .1k_L$ ; this non-Heisenberg-limited  $\sigma_k$  is associated with the BEC experiencing inhomogeneous axial forces and consequent momentum broadening during the adiabatic lattice load. At  $t_0 = 9.3$  ms the BEC reaches the edge of the Brillouin zone and we begin sinusoidal modulation of the lattice beam intensity. Following the removal of the optical dipole trap, the system is described by the Hamiltonian

$$H = \frac{p^2}{2m} + \frac{V(t)}{2} \cos(2k_L x) + \frac{1}{2} m \omega^2 x^2 - Fx. \quad (1)$$

The magnetic trap frequency is  $\omega = 2\pi \times 15.5$  Hz, with initial local force  $F = \hbar/T_B d$  and Bloch period  $T_B =$

arXiv:2006.01612v1 [cond-mat.quant-gas] 2 Jun 2020

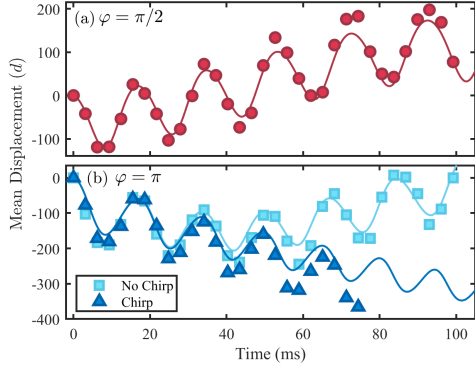


FIG. 2. Directed Floquet-Bloch transport in an inhomogeneous force field. (a) Measured (points) and numerically predicted (line) mean atomic position as a function of time for a drive phase  $\varphi = \pi/2$ . The applied force points towards larger positive displacements. (b) Similar measurements (points) and numerical theory (lines) for an initial drive phase  $\varphi = \pi$ . A time-invariant drive frequency yields epicyclic motion due to force inhomogeneity (squares). An adaptive drive using a frequency chirp suppresses this behavior and extends the range of transport (triangles, and images in Fig. 1c).

16.75 ms. The time-varying lattice depth  $V(t)$  is

$$V(t) = \begin{cases} V_0 [1 + \alpha \sin(\varphi)], & -t_0 < t < 0 \\ V_0 [1 + \alpha \sin(\omega_D t + \varphi)], & t \geq 0. \end{cases} \quad (2)$$

For all runs, the drive frequency is  $\omega_D = 2\pi \times 53.56$  Hz; in the case of chirped driving, this is the frequency at  $t = 0$ . The modulation depth is held at  $\alpha = 0.24$  with average lattice depth  $V_0 = 4.3 E_R$ . Due to the drive and the force inhomogeneity, the angular Bloch frequency  $\omega_B = 2\pi/T_B$ , drive period  $T_D = 2\pi/\omega_D$ , and tunneling  $J$  are all potentially time-varying quantities. The critical parameter we manipulate to drive different dynamical behaviors is the initial drive phase  $\varphi$ .

Fig. 2 shows data taken for drive phases experimentally found to be optimal for long-range pumping of the BEC both with and against the applied force. The results demonstrate pumping of the BEC over 200 lattice sites in just 5 Bloch cycles; the large increase in magnitude of transport rate as compared to Ref. [3] can be attributed mainly to the low mass of  ${}^7\text{Li}$ . We observe optimal pumping along the direction of applied force at  $\varphi = \pi/2$ ; as discussed below, this disagrees starkly with a theoretical description based on a homogeneous effective electric field, which predicts optimal transport along the direction of force for  $\varphi = 0$  and optimal transport against the force for  $\varphi = \pi$ .

The observed dynamics are highly asymmetric in drive phase. Modulating at  $\varphi = 3\pi/2$ , exactly out of phase

with the experimentally observed optimal condition for force-aligned pumping, does not produce directed transport. In experiments with a modulation phase of  $\varphi = \pi$ , the cycle-averaged velocity actually changes sign, as shown in Fig. 2b. This phenomenon is similar to super Bloch oscillations, though here the evolving relative phase between drive and Bloch oscillation does not result from a static detuning, but instead from a self-parametric modulation due to the spatial variation in Bloch frequency. Put differently, the force inhomogeneity eliminates the possibility of a global Wannier-Stark resonance, giving rise to slow oscillatory transport as a natural dynamical mode.

An adaptive driving protocol can recover directed monotonic pumping against an applied force even without a true Wannier-Stark resonance. Figs. 2b and 1c show experimental measurements of transport produced by an adaptive drive which includes a chirped drive frequency. Intuitively, the chirp can be understood as stroboscopically maintaining the local Wannier-Stark resonance condition for a set of unevenly spaced ladders, or alternatively as optimizing the cycle-averaged spatial transport sketched in Fig. 1a by accounting for the average change in  $\omega_B$  per cycle. These data were taken with a chirp rate of 115 Hz/s, causing an increase of  $\omega_D$  by  $2\pi \times 2.15$  Hz each drive cycle. While here a linear chirp is shown to be effective for a linearly-varying force, the results suggest that higher-order, non-monotonic and piece-wise adaptive driving protocols could serve as flexible tools for engineering transport in arbitrary force landscapes.

Next we discuss a simple analytic model of directed transport for a homogeneous force; this provides a useful framework for highlighting and understanding the qualitatively new phenomena introduced by force inhomogeneity. We consider a tight-binding model in the single-band approximation. For a sufficiently low-frequency drive we can define a time-dependent ground band dispersion  $E(k, t) = -2J[V(t)] \cos(kd)$ , with tunneling  $J$  a function of the time-dependent lattice depth  $V$ , and  $k$  the quasimomentum. In the semiclassical picture, the BEC moves at the group velocity

$$v_g(t) = \frac{2J[V(t)]d}{\hbar} \sin[k(t)d], \quad (3)$$

where  $k(t)$  denotes the time-dependent quasimomentum. For weak modulation,  $J$  varies to first order in time as  $J[V(t)] \approx J(V_0) [1 - \alpha_0 \sin(\omega_D t + \varphi)]$ , with scaled modulation index  $\alpha_0 = \alpha |J'(V_0)| V_0 / J(V_0)$ ; the prime indicates partial differentiation with respect to lattice depth, and for our experimental parameters  $\alpha_0 \approx 1.15\alpha$  as computed using Mathieu parameter relations for the band edges [23]. Under this approximation, the cycle-averaged

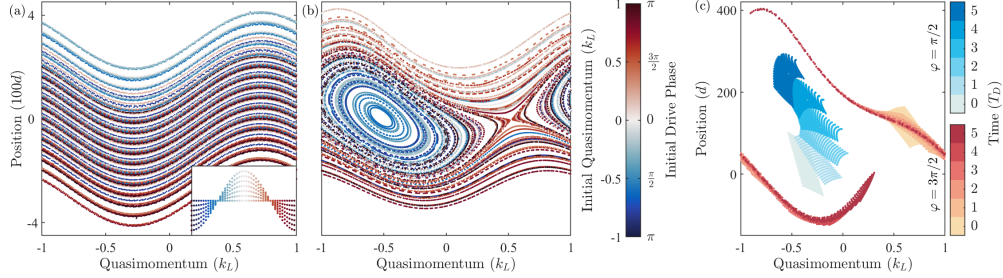


FIG. 3. Effect of the inhomogeneity-induced phase space structure on transport. (a) Stroboscopic Poincaré map for a homogeneous force at 6 Hz detuning between drive and Bloch oscillation, showing super-Bloch-like oscillations wrapping the Brillouin zone. For panels (a) and (b) an  $11 \times 11$  grid of initial conditions spanning 400 lattice sites and the whole Brillouin zone was numerically evolved and plotted stroboscopically out to  $200 T_D$  (longer than our longest experiment times). Colorbar indicates drive phase  $\varphi$ , or, equivalently, initial quasimomentum. Inset shows the stroboscopic Poincaré map on identical axes out to  $6 T_D$  for zero detuning, for a single initial position over the whole quasimomentum range; trajectories unwrap yielding linear vertical transport and two invariant quasimomenta. (b) Stroboscopic Poincaré map at the same detuning, for an inhomogeneous force matching our experimental conditions. Note the emergence of nontrivial fixed points and topologically distinct classes of orbits. (c) Short-time portrait of the evolution of an ensemble for  $\varphi = \pi/2$  (blue time) and  $3\pi/2$  (red time), yielding stable transport and rapid spreading respectively as a result of the different fixed point characteristics. The plotted sample is a  $21 \times 21$  grid spanning  $1\text{-}\sigma$  in both position and momentum. The time colorbars match the definition of  $t$  in Eq. 1 after adding .25 (blue) and .75  $T_D$  (red).

spatial transport is

$$\Delta x \approx -\frac{2\alpha_0 J(V_0)d}{\hbar} \int_0^{T_D} \sin(\omega_D t + \varphi) \sin\left(\int_0^t \omega_B(t') dt'\right) dt. \quad (4)$$

For a homogeneous force,  $\omega_B(t)$  is a constant, and thus the quasimomentum evolves as  $k(t) = (\omega_B t + \pi)/d$ . The  $\pi$  offset is introduced to match our experimental protocol. For resonant driving  $\omega_D = \omega_B$ , the average velocity is

$$\bar{v}_g = \frac{\alpha_0 v_0}{2} \cos(\varphi). \quad (5)$$

On average the atoms travel at half the characteristic velocity  $v_0 = 2J(V_0)d/\hbar$  scaled by the modulation index  $\alpha_0$  and the alignment between drive and Bloch cycles  $\cos(\varphi)$ . It is clear that  $\varphi = 0$  and  $\varphi = \pi$  yield maximum pumping down and up the potential respectively.

For small detuning between drive and Bloch frequencies, this homogeneous model predicts transport over many periods resulting from the effective evolution of  $\varphi$ . It is useful to compare and contrast these parametrically-driven dynamics to super Bloch oscillations [3]: both can be schematically understood as resulting from modulation of the Wannier-Stark length  $l = 2J/F$ , either by modulation of the numerator (this work) or the denominator (Ref. [3]). In the language of nonlinear dynamics, the distinction is between forced and parametrically-excited oscillators, and our experiment is a quantum mechanical analogue of a parametrically-excited pendulum [24–26], with angle mapped to quasimomentum and

angular momentum to position, in the regime of purely rotating solutions.

While the intuitive mechanism for Floquet-pumped transport in an *inhomogeneous* force field can still be conceptually understood with this homogeneous framework, our measurements deviate qualitatively from these predictions as  $\omega_B$  acquires parametric time dependence from the time-varying position. The observed optimal phase for force-directed pumping (Fig. 2a) is in clear disagreement with the constant-force prediction of  $\varphi = 0$ ; in fact, Eq. 5 predicts a mean velocity of zero for  $\varphi = \pi/2$ . The effect of force inhomogeneity is even more pronounced when attempting Floquet pumping against the potential gradient: as shown in Fig. 2b, we observe a rapid change of the transport direction and no symmetry between opposite-phase drives. These qualitative discrepancies are due mainly to the failure of the constant Bloch frequency approximation.

The breakdown of the theory based on a constant effective electric field motivates the search for a more complete theoretical description of driven Bloch dynamics in inhomogeneous fields. As a key result of this work, we show that the qualitatively different dynamics observed arise from a rich underlying inhomogeneity-induced phase space structure which exhibits a topological transition in the character of stroboscopic Poincaré orbits. To see this, we use a Floquet map formalism, analyzing the phase-space trajectories stroboscopically with respect to the drive. Fig. 3a shows the calculated Poincaré map for a spatially uniform force and nonzero drive detuning. Super-Bloch-like oscillatory behavior is

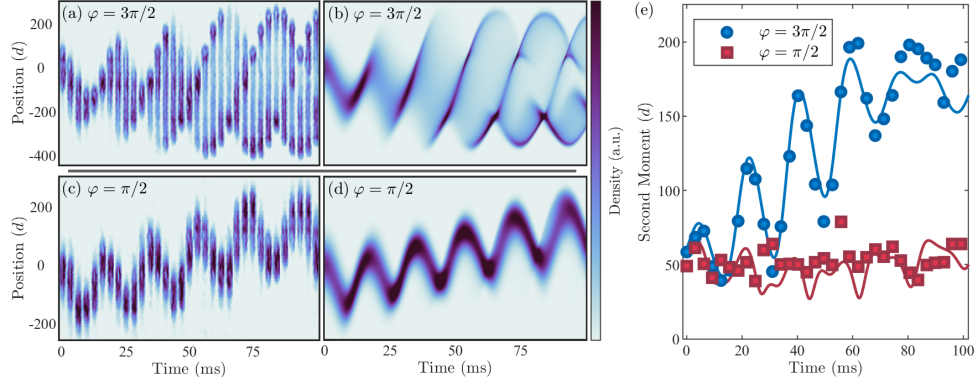


FIG. 4. Phase-dependent spatial dynamics as a probe of the stroboscopic Poincaré map. (a) and (c): Time-sequences of absorption images of an atomic ensemble subjected to drive phases of  $\varphi = 3\pi/2$  (a) and  $\varphi = \pi/2$  (c). These two phases are predicted to give rise to topologically distinct Poincaré orbits with qualitatively different transport dynamics, as shown in Fig. 3c. (b) and (d): Numerical simulations of the 1D density evolution under the same conditions as (a) and (c). The simulated density is averaged over independent, Gaussian-weighted 1D trials at varying lattice depths corresponding to transverse variation of beam intensity. (e) The second moment of the density distribution is plotted versus time for initial drive phases  $\varphi = 3\pi/2$  (circles) and  $\pi/2$  (squares). Solid lines show simulated second moment evolution, accurately capturing the asymmetric enhancement and suppression of curvature-induced monopole modes.

evident: the detuning generates a uniform quasimomentum shift for every point in phase space, and mediates the evolving phase in the sinusoidal arguments of Eq. 4, leading to an oscillatory profile of position versus quasimomentum. The sign of the quasimomentum shift is determined by whether the drive is red or blue-detuned, and the constant nature of the detuning ensures that the Floquet trajectories all wrap the phase space cylinder. On resonance, a transition occurs where all trajectories unwrap as the quasimomentum shift vanishes, and each point undergoes a vertical shift in the position direction determined by Eq. 5; this is accompanied by the emergence of two fixed lines in the map for quasimomenta corresponding to initial drive phases of  $\pi/2$  and  $3\pi/2$ . The inset of Fig. 3a shows the map for a resonant drive with starting points at only one initial position, revealing the invariant quasimomenta.

In the presence of force inhomogeneity, the fixed lines mentioned above become fixpoints where the drive meets the (position-dependent) Wannier-Stark resonance condition, yielding a strikingly different stroboscopic Poincaré map, as shown in Fig. 3b. The fixpoints near  $k = -0.5$  and  $0.5k_L$  are center-like and saddle-like respectively. Here super-Bloch-like transport breaks down and the system admits a new class of motion not present in Fig. 3a, namely regular cyclic orbits about the  $k = -0.5k_L$  fixed point. In the stroboscopic map, these orbits have a distinct topology as closed loops which do not wrap the Brillouin zone cylinder; this emerges due to the possibility of the now implicitly time-dependent

detuning changing its cycle averaged sign, something not possible in the homogeneous force case. A topologically distinct class of super-Bloch-like trajectories wrapping the Brillouin zone are observed at positions sufficiently far away from the resonance point.

The Floquet map serves as a powerful intuitive tool for understanding and predicting the results of inhomogeneity in the effective electric field. As shown in 3c, the experimental  $\varphi = \pi/2$  condition is represented by an ensemble which starts near the stable fixpoint, and the observed DC transport represents a partial cycle of the circulatory behavior in which the position spread of the ensemble is not significantly changed, approximating the motion of a rigid body. A drive phase of  $\varphi = 3\pi/2$ , in contrast, corresponds to an ensemble starting near the saddle-like fixpoint. In this case the Floquet map dynamics predict rapid divergence along the unstable axis of the fixpoint, with the ensemble stretching in phase space and splitting up among orbits confined at the positional extremes. This corresponds to a maximal violation of rigid-body-like dynamics, exhibiting oscillations and growth in higher moments of the spatial distribution.

Our experimental observations confirm these predictions of the stroboscopic Poincaré map. Fig. 4a and 4c compare experimental image sequences of BEC evolution for drive phases of  $\varphi = 3\pi/2$  and  $\varphi = \pi/2$  respectively. In the  $\varphi = 3\pi/2$  data, an initially localized distribution is observed to rapidly spread, eventually delocalizing over 600 lattice sites in a highly non-normal distribution. Here, the drive acts to amplify the

curvature-induced breathing mode, eventually splitting the cloud largely into two regions of higher density near the edge of the distribution. Note that these dynamics correspond in detail to the predicted  $\varphi = 3\pi/2$  evolution illustrated in Fig 3c. In contrast, the data for a drive phase  $\varphi = \pi/2$ , shifted by exactly  $\pi$ , reveals surprisingly stable wavepacket transport given the presence of both significant force inhomogeneity and a strong drive. In this case, the drive serves the dual role of preserving the wavefunction spatial mode and inducing transport. Both cases exhibit good agreement with numerical simulations of squared-wavefunction evolution shown in Fig. 4b and 4d. The match to theory is quantitative as well as qualitative: Fig. 4e compares the evolution of the second moment of the position distribution to numerical theory for both drive phases. For  $\varphi = 3\pi/2$ , the second moment oscillates and grows rapidly before saturating at nearly 4 times the initial value. This is in stark contrast to the  $\varphi = \pi/2$  case, in which the data display little to no variation of the second moment over the entire interval.

In conclusion, we have shown that the combination of an inhomogeneous force with periodic modulation drives rich new dynamical behaviors beyond those of a pure Bloch or super-Bloch oscillator. Good agreement with numerical calculations supports our interpretation of the inhomogeneity-induced dynamics as arising from a fundamental change in the phase space structure of the Hamiltonian giving rise to distinct topological classes of Poincaré orbits. These results point the way to a general protocol for controlling transport and density evolution with lattice amplitude modulation even in uncontrolled force environments. Potential future applications of these techniques include the generation of spatially squeezed states, new models for solid-state high-harmonic generation, and control elements for continuously-trapped atom interferometry. Since force metrology is an important use of atomic Bloch oscillations, these results have direct relevance for applications in which the force environment is both uncontrolled and inhomogeneous. Inclusion of static or modulated interatomic interactions is an exciting possible direction for future work [27, 28], as is the effect of quasiperiodic or multiple-frequency driving. Such a platform would be well-suited for exploring the correspondence between the breakdown of classical orbit regularity and non-ergodic many-body dynamics.

The authors thank Max Prichard for experimental assistance and Erich Mueller for useful discussions. DW acknowledges support from the National Science Foundation (CAREER 1555313), the Army Research Office (PECASE W911NF1410154 and MURI W911NF1710323), and the University of California's Multicampus Research Programs and Initiatives (MRP-19-601445). DW and RS acknowledge support from the UCSB NSF Quantum Foundry through Q-AMASE-i program award DMR-1906325.

- [1] F. Bloch, *Z. Phys.* **52** (1929).
- [2] C. Zener, *Proc. R. Soc. A* **145** (1934).
- [3] E. Haller, R. Hart, M. J. Mark, J. G. Danzl, L. Reichsöllner, and H. C. Nägerl, *Phys. Rev. Lett.* **104**, 200403 (2010).
- [4] S. Ghimire and D. A. Reis, *Nature Physics* **15**, 10 (2019).
- [5] Z. A. Geiger, K. M. Fujiwara, K. Singh, R. Senaratne, S. V. Rajagopal, M. Lipatov, T. Shimasaki, R. Driben, V. V. Konotop, T. Meier, and D. M. Weld, *Phys. Rev. Lett.* **120**, 213201 (2018).
- [6] M. Ben Dahan, E. Peik, J. Reichel, Y. Castin, and C. Salomon, *Phys. Rev. Lett.* **76**, 4508 (1996).
- [7] B. P. Anderson and M. A. Kasevich, *Science* **282**, 1686 (1998).
- [8] M. Gustavsson, E. Haller, M. J. Mark, J. G. Danzl, G. Rojas-Kopeinig, and H.-C. Nägerl, *Phys. Rev. Lett.* **100**, 080404 (2008).
- [9] P. M. Preiss, R. Ma, M. E. Tai, A. Lukin, M. Rispoli, P. Zupancic, Y. Lahini, R. Islam, and M. Greiner, *Science* **347**, 1229 (2015).
- [10] A. Alberti, G. Ferrari, V. V. Ivanov, M. L. Chiofalo, and G. M. Tino, *New J. Phys.* **12**, 065037 (2010).
- [11] S. R. Wilkinson, C. F. Bharucha, K. W. Madison, Q. Niu, and M. G. Raizen, *Phys. Rev. Lett.* **76**, 4512 (1996).
- [12] V. V. Ivanov, A. Alberti, M. Schioppo, G. Ferrari, M. Artoni, M. Chiofalo, and G. Tino, *Phys. Rev. Lett.* **100**, 043602 (2008).
- [13] C. Sias, H. Lignier, Y. Singh, A. Zenesini, D. Ciampini, O. Morsch, and E. Arimondo, *Phys. Rev. Lett.* **100**, 040404 (2008).
- [14] A. Alberti, V. V. Ivanov, G. M. Tino, and G. Ferrari, *Nature Phys.* **5**, 547 (2009).
- [15] D. H. Dunlap and V. M. Kenkre, *Phys. Rev. B* **34**, 3625 (1986).
- [16] Q. Thommen, J. C. Garreau, and V. Zehl, *Phys. Rev. A* **65**, 053406 (2002).
- [17] H. Korsch and S. Mossman, *Phys. Lett. A* **317**, 54 (2003).
- [18] A. Eckardt, M. Holthaus, H. Lignier, A. Zenesini, D. Ciampini, O. Morsch, and E. Arimondo, *Phys. Rev. A* **79**, 013611 (2009).
- [19] A. R. Kolovsky and H. J. Korsch, [arXiv:0912.2587](https://arxiv.org/abs/0912.2587) [quant-ph].
- [20] K. Kudo and T. Monteiro, *Phys. Rev. A* **83**, 053627 (2011).
- [21] T. Salger, S. Kling, T. Hecking, C. Geckeler, L. Morales-Molina, and M. Weitz, *Science* **326**, 1241 (2009).
- [22] C. J. Fujiwara, K. Singh, Z. A. Geiger, R. Senaratne, S. V. Rajagopal, M. Lipatov, and D. M. Weld, *Phys. Rev. Lett.* **122**, 010402 (2019).
- [23] M. Holthaus, *Journal of Physics B: Atomic, Molecular and Optical Physics* **49**, 013001 (2016).
- [24] M. Clifford and S. Bishop, *Phys. Lett. A* **201** (1995).
- [25] X. Xu, M. Wiercigroch, and P. Cartmel, *Chaos, Solitons and Fractals* **23** (2004).
- [26] D. Capecchi and S. R. Bishop, *Dynamics and Stability of Systems* **9** (1994).
- [27] P. Ribeiro, A. Lazarides, and M. Haque, *Phys. Rev. Lett.* **124**, 110603 (2020).
- [28] E. Díaz, A. G. Mena, K. Asakura, and C. Gaul, *Phys. Rev. A* **87** (2013).

# Appendix F

## Prethermal Dynamical Localization and the Emergence of Chaos in a Kicked Interacting Quantum Gas (preprint)

This appendix contains the arXiv version of the interacting quantum kicked rotor work discussed in Chapter 5.

## Prethermal Dynamical Localization and the Emergence of Chaos in a Kicked Interacting Quantum Gas

Alec Cao,<sup>1</sup> Roshan Sajjad,<sup>1</sup> Hector Mas,<sup>1</sup> Ethan Q. Simmons,<sup>1</sup> Jeremy L. Tanlimco,<sup>1</sup> Eber Nolasco-Martinez,<sup>1</sup> Toshihiko Shimasaki,<sup>1</sup> H. Esat Kondakci,<sup>1</sup> Victor Galitski,<sup>2</sup> and David M. Weld<sup>1</sup>

<sup>1</sup>Department of Physics, University of California, Santa Barbara, California 93106, USA

<sup>2</sup>Joint Quantum Institute and Department of Physics, University of Maryland, College Park, MD 20742, USA

While ergodicity is a fundamental postulate of statistical mechanics and implies that driven interacting systems inevitably heat, ergodic dynamics can be disrupted by quantum interference. Despite a quarter-century of experimental studies, the effect of many-body interactions on the resulting dynamically localized state has remained unexplored. We report the experimental realization of a tunably-interacting kicked quantum rotor ensemble using a Bose-Einstein condensate in a pulsed optical lattice. We observe a prethermal localized plateau, which survives for hundreds of kicks, followed by interaction-induced anomalous diffusion. Echo-type time reversal experiments establish the role of interactions in destroying reversibility, and a mapping to kicked spin models illustrates connections to many-body dynamical localization in spin chains. These results demonstrate a dynamical transition to many-body quantum chaos, and illuminate and delimit possibilities for globally protecting quantum information in interacting driven quantum systems.

Ergodicity breaking in quantum matter and relaxation dynamics of thermalizing phases are two aspects of a central question of non-equilibrium many-body physics: how and when do isolated quantum systems thermalize? A growing body of theoretical and experimental work suggests that the Anderson insulator can be stable against interactions, implying the existence of a non-ergodic many-body localized (MBL) phase [1, 2]. While disorder-induced MBL is often invoked as a mechanism for avoiding heating in driven systems [3], recent theoretical evidence has raised the exciting possibility of many-body *dynamically* localized (MBDL) phases which are sustained by the external drive itself in the absence of disorder [4–6]. Such phases offer a general dynamical protocol for stabilizing quantum information, complementing approaches based on drive-induced control of special quantum scar states [7]. Beyond total ergodicity breaking, observations of long-lived prethermal states [8–10] and anomalous diffusion [11, 12] across a variety of platforms pose both fundamental theoretical questions and practical alternatives for dynamical engineering of many-body systems. Both prethermalization and anomalous diffusion are features of the poorly-understood interface between chaotic and localized regimes [13], and a general predictive framework for such phenomena remains an open challenge.

The paradigmatic atom-optics quantum kicked rotor (QKR) [16] is a natural starting point for experimentally probing both quantum chaotic and non-ergodic many-body Floquet phases. While strong, repeated kicking drives a classical rotor into chaotic diffusion, the corresponding quantum rotor stops absorbing energy after a finite time, signaling the onset of dynamical localization. Despite the complete absence of disorder, this phenomenon can be understood as a manifestation of Anderson localization in momentum space [17, 18]. The interplay between interactions and dynamical localiza-

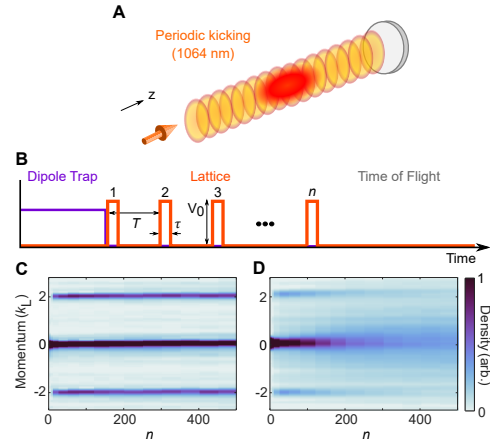


Fig. 1. **Experimentally realizing an interacting quantum kicked rotor.** (A) Schematic of BEC in single pulsed optical lattice. (B) Experimental sequence. After setting the scattering length the trap is removed and kicking is applied with period  $T$ , pulse width  $\tau$ , and amplitude  $V_0$  for  $n$  cycles. The atoms are imaged after a time-of-flight expansion [14]. (C-D) Measured axial momentum distribution versus kick number  $n$  for noninteracting (C) and interacting (D) samples, revealing collisional momentum redistribution.

tion has been explored theoretically, but never experimentally. While numerical treatments suggest a breakdown of dynamical localization into anomalous diffusion [19–21], the mean-field approximation on which they are based may be strongly violated by collisional redistribution and quantum depletion [22]. Certain non-perturbative 1D models display ergodicity-breaking and

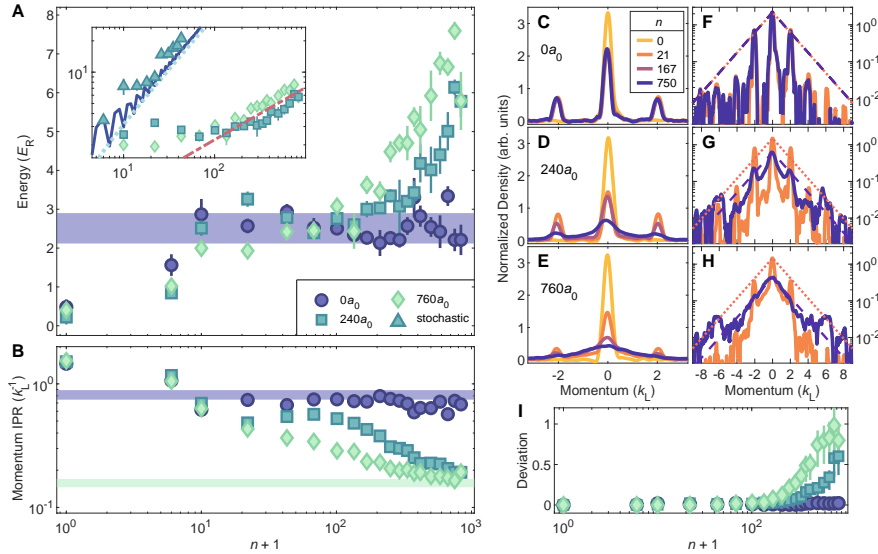


Fig. 2. **Observing the interaction-induced emergence of quantum chaos.** (A) Energy versus kick number for varying  $a$ . Blue horizontal shaded region indicates the measured single-rotor localization energy of  $E_{loc} = 2.5(4)E_R$ . Here  $V_0 = 64E_R$ ,  $T = 1.2\mu\text{s}$  and  $\tau = 300\text{ ns}$  ( $K \approx 2.3$  and  $\bar{k} \approx 1.5$ ). The inset contrasts interaction-induced delocalization and anomalous diffusion with classical diffusion caused by a sequence of random offsets from the average kick spacing  $T$  drawn uniformly from the interval  $[-T/4, T/4]$ . The solid curve is noninteracting quantum theory and the dotted line is a diffusion curve  $4Dn/\bar{k}^2$  with  $D \approx 0.19$  extracted from the classical standard map [15]. The red dot-dashed line is a subdiffusive  $\sqrt{n}$  law serving as a guide to the eye. (B) Momentum-space IPR with transverse dimensions integrated out. The shaded regions are predictions for two exponentially localized distributions with  $1/e$  localization length  $k_{loc} = \sqrt{E_{loc}} \approx 1.6(1)k_L$  [14]. (C-E) Normalized smoothed momentum space densities at various  $n$ . (F-H) The same densities on a logarithmic scale. The orange dotted and purple dashed lines are exponentially localized curves  $\exp(-k/k_{loc})$  with amplitudes normalized to match the peak of the measured distributions at the given  $n$ . (I) Deviation from exponential localization over time based on integrated ratio between measured and exponential distributions with errorbars computed from uncertainty in  $k_{loc}$  [14].

an MBDL phase [4, 5]. The exciting possibilities on both fronts motivate detailed experimental investigation.

Here we report the first experimental study of dynamical localization in the presence of tunable interactions. Measuring results of QKR sequences up to one thousand kicks, we observe a prethermal dynamically-localized regime, followed by interaction-induced anomalous diffusion in momentum space after a variable break time. The role of interactions in destroying reversibility is established using a Loschmidt echo protocol [23, 24]. Numerical and experimental exploration of a quantitative mapping between the QKR problem and kicked Heisenberg spin chains illuminates connections to many-body dynamical localization in a broad array of experimental contexts.

These experiments investigate a  $^7\text{Li}$  Bose-Einstein condensate (BEC) kicked  $n$  times at period  $T$  by a far-detuned optical lattice of spacing  $d = 532\text{ nm}$  and depth  $V_0$  for duration  $\tau$  (see Fig. 1). We report momentum and energy in units of  $k_L = \pi/d$  and  $E_R = \hbar^2 k_L^2/2m$

with  $m$  the mass of  $^7\text{Li}$ . The single-particle QKR is defined by the 1-cycle Floquet map  $U = e^{-i\bar{k}k^2/2}e^{-iK \cos z/\bar{k}}$  describing a sharp cosine potential impulse followed by free evolution. Here  $k$  and  $z$  are momentum and position,  $K = \bar{k}V_0\tau/2\hbar$  is the stochasticity parameter characterizing kicking strength and  $\bar{k} = 8E_RT/\hbar$  is an effective Planck's constant determined by the kick period. Absorption imaging after free expansion is used to measure the momentum distribution; see the supplementary text for a discussion of systematic effects in this procedure. Interatomic interactions are varied by tuning the s-wave scattering length  $a$  (reported in units of the Bohr radius  $a_0$ ) using a magnetic Feshbach resonance. While the kicking primarily couples discrete momentum states along a single dimension, the atoms are entirely unconfined between kicks; scattering between momentum modes thus couples the system to a bath of transverse free-particle states.

The main result of this work is presented in Fig. 2A.

While a noninteracting sample exhibits localization, saturating to a finite energy for over 800 kicks, interacting samples clearly demonstrate the destruction of the dynamically localized plateau with increasing scattering length. At intermediate interaction strength ( $a = 240a_0$ ), we observe saturation to the same energy as non-interacting samples for approximately 300 kicks, suggesting the existence of a reasonably long-lived prethermal state. In contrast, the  $760a_0$  trace exceeds this localized energy after around 100 kicks; whether a quasiequilibrium dynamical state is truly established in this stronger-interacting sample is less clear. Fig. 2B shows another aspect of the same evolution, plotting the momentum space inverse participation ratio (IPR) versus kick number. The IPR characterizes the number of states over which the system is distributed, thereby also probing how collisional momentum redistribution washes out the originally discrete momentum modes, a process less easily inferred from energy measurements. While the  $240a_0$  data exhibit a clear steady-state behavior for 100 kicks, the  $760a_0$  IPR decreases monotonically for almost the entire experiment.

A second key result of these measurements is that the observed delocalizing dynamics clearly exhibit anomalous diffusion: it appears that even interacting quantum kicked rotors absorb energy much more slowly than classical rotors. The inset of Fig. 2A compares the nature of the observed interaction-induced subdiffusive delocalization with linear energy growth in the classically chaotic model. We experimentally simulate classical dynamics by adding stochastic fluctuations to the kicking period  $T$ , making use of the known sensitivity of dynamical localization to timing noise [25]. These experimental data agree both with single-particle quantum numerics and with the linear energy growth predicted by the classical standard map [15], and stand in clear contrast to the measured interaction-induced anomalous diffusion away from the dynamically localized state. The dot-dashed red line indicates a  $\sqrt{n}$  energy growth, and fitting the late-time data to  $n^\alpha$  yields anomalous diffusion exponents  $\alpha$  in the range [0.4, 0.6]. For reference, 1D Gross-Pitaevskii simulations on a ring [21] predict  $\alpha \in [0.5, 0.8]$ , though a direct quantitative comparison to theory is challenging due to the high depletion of the condensate and the three-dimensional nature of the experiment. Theoretical studies of the effect of local nonlinearity on real-space Anderson localization instead suggest  $\alpha \in [0.3, 0.4]$  [26, 27], but the long-range nature of contact interactions in momentum space similarly complicates comparison. This clear observation of anomalous diffusion in the interacting quantum kicked rotor raises a variety of fascinating questions for future exploration. What are the correlations or other mechanisms which generate anomalous diffusion dynamics? What if any theoretical framework is appropriate for quantitatively predicting wavefunction evolution in this regime? What are the universality properties of the subdiffusive exponent?

For further insight into the dynamics of kicked interact-

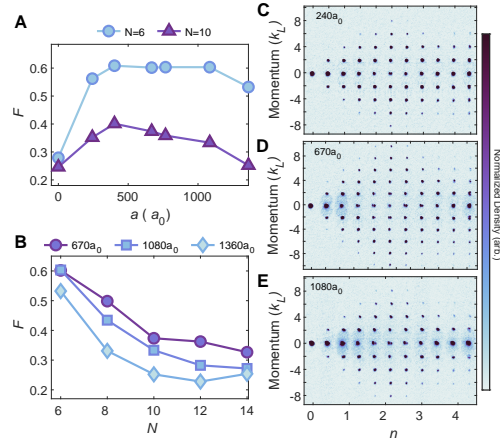


Fig. 3. **Effect of interactions on reversibility in Loschmidt echo experiments.** (A) Measured Loschmidt echo fidelity  $F$  for a range of scattering lengths  $a = [0, 1500] a_0$  for  $N = 6$  (blue circles) and  $N = 10$  (purple triangles), where  $N$  indicates the total number of kicks; a first set of  $N/2$  kicks propagates the system *forward* in time and a second time-reversal set of  $N/2$  kicks propagates it *backwards*. (B) Measured fidelity  $F$  at three different interaction strengths as a function of total number of kicks  $N$  in a Loschmidt echo experiment. (C-E) Averaged absorption images of a BEC after the first  $n$  kicks of an  $N = 10$  Loschmidt echo protocol, for three different  $a$ .

ing quantum systems we examine the evolution of the momentum distribution, shown in Figs. 2C-E. We observe a clear distinction between the noninteracting samples, which settle at a sharply-peaked dynamically-localized momentum distribution, and the interacting samples, which gradually smear out in momentum space due to scattering. Plotting these same densities on a logarithmic scale in Fig. 2F-H illuminates the destruction of dynamical Anderson localization by assessing the departure from exponentially-localized Floquet states. The smeared-out lower-energy modes actually appear to maintain the expected localization length, and thus do not trivially indicate a departure from exponential localization. This observation is also reflected in the fact that two predictions based on exponentially localized distributions bound the measured IPR in Fig. 2B. Instead, the departure from exponential localization manifests in the emergence of increased relative population in the tails of the distribution. It is interesting to note that recent theory suggests that even MBDL phases are expected to exhibit universal power-law decaying tails [29]. In Fig. 2I we quantitatively characterize the overall deviation from exponential localization [14], revealing a break time near 200 kicks for both interaction strengths. These findings provide a second experimental signature of the destruction of the

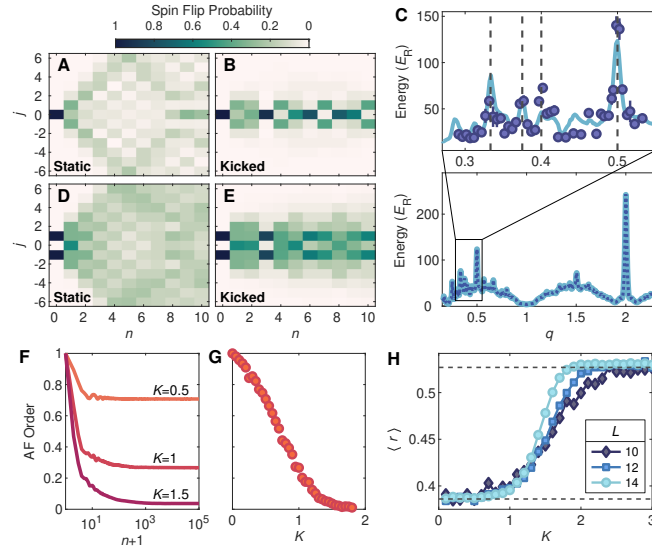


Fig. 4. **Kicked-rotor dynamics and many-body dynamical localization in kicked spin chains.** (A-B) Calculated single-spin-flip evolution for static and kicked spin-1/2 XXX chains of length  $L = 13$  for  $K = 2.4$ ,  $k = 1.5$  and  $\beta = 0$ . (C) Spin chain quantum resonance spectroscopy (solid) demonstrating equivalence to QKR (dashed) in the single spin-flip sector with  $K = 3k$ ,  $L = 51$  and averaging over a Gaussian ensemble of  $\beta$ . Energy is after 10 kicks. Zoomed-in panel compares experimental measurements on the atomic quantum kicked rotor to predictions of spin chain numerics. Dashed vertical lines indicate  $q = 1/3, 3/8, 2/5$ , and  $1/2$ . (D-E) The same as A-B but with 2 spin flips. (F) Time average of the staggered magnetization  $(\sum_j (-1)^j \sigma_j^z)/L$  versus kick number, starting from an initial Néel state with  $k = 1$ ,  $L = 12$ ,  $\beta = 0.1$  and varying  $K$ . (G) Staggered magnetization in the infinite-time limit versus  $K$ , for the same parameters as panel F. (H) Gap-ratio statistic of the  $M = 0$  sector at  $k = 1$  for varying  $L$  averaged over 100 values of  $\beta$ . Dashed lines indicate predictions of the Poisson  $\langle r \rangle \approx 0.386$  and circular-orthogonal ensemble  $\langle r \rangle \approx 0.527$  [28].

dynamically localized state by interactions, now both at the level of macroscopic observables and squared wavefunctions.

The onset of energy delocalization due to interactions suggests a transition to a regime of many-body quantum chaos. Time-reversal dynamics lie at the foundation of our understanding of both classical and quantum chaos [30, 31]. In Fig. 3 we probe the nature of chaotic dynamics in kicked many-body systems by measuring the effect of interactions on a Loschmidt echo time-reversal protocol. The echo is realized using quantum resonances [32] which occur for  $k = 2\pi q$  with  $q$  rational; in particular for  $q = 2$  ( $T \approx 9.95 \mu\text{s}$ ), the free evolution in  $U$  largely vanishes and effective time reversal can be achieved by setting  $q$  to 1 for a single kick halfway through the sequence [14, 23, 24]. This procedure would create exact time reversal for a single zero-quasimomentum state in the absence of interactions. Due to finite quasimomentum spread and non-reversed interactions, the reversal is imperfect, yielding a Loschmidt fidelity  $F = \left| \langle \psi | U_2^\dagger U_1 | \psi \rangle \right|^2$  where  $U_1$  and  $U_2$  are time-

evolution operators differing by some perturbation. Perhaps surprisingly,  $F$  initially *increases* as the scattering length  $a$  is turned up from zero. In this regime  $U_1$  and  $U_2$  are primarily distinguished by the failure to reverse kinetic energy, and thus the increase can be explained by Thomas-Fermi reduction of the initial state momentum spread. Eventually, for large enough  $a$ , the interaction becomes the primary perturbation and  $F$  begins to decrease with  $a$ , marking the transition to predominantly interaction-induced irreversibility. The decay of fidelity with total number of kicks in a Loschmidt echo experiment is shown in Fig. 3B. The use of Loschmidt echo techniques as a probe of many-body quantum chaos not only helps illuminate the origins of the delocalizing dynamics we observe, it also opens up the intriguing future possibility of extending these protocols to measure out-of-time-order correlators and probe scrambling in many-body quantum chaotic systems.

The interplay between many-body dynamical localization and many-body quantum chaos is a topic of broad current interest, relevant in contexts well beyond the ex-

perimental model of the quantum kicked rotor which we explore here. To highlight this breadth, we describe and quantitatively explore a mapping from the QKR to a kicked Heisenberg spin chain, which can be used as a basis for generalization and further exploration. Specifically, we investigate the Floquet map  $U_{\text{kickedXXZ}} = e^{-iK H_{\text{quad}}/4} e^{-iK H_{\text{XXZ}}/4K}$ , with  $H_{\text{quad}} = \sum_j (j + \beta)^2 \sigma_j^z$  a quadratic field and  $H_{\text{XXZ}} = \sum_j (\sigma_j^x \sigma_{j+1}^x + \sigma_j^y \sigma_{j+1}^y + \Delta \sigma_j^z \sigma_{j+1}^z)$  an XXZ Hamiltonian with  $\sigma^{x,y,z}$  the Pauli matrices and  $\Delta$  the anisotropy parameter.  $\beta$  here serves as an analogue to quasimomentum in the QKR model, and time-evolution conserves the total magnetization  $M = \langle \sum_j \sigma_j^z \rangle$ . This model is known to correspond to the QKR in single and few-body regimes [33, 34]; for a single particle or spin flip the correspondence is essentially exact up to finite size effects. Dynamical localization and quantum resonance in the spin model are demonstrated in Fig. 4A-C. In the zoom-in of 4C, we verify the QKR correspondence experimentally by comparing the kicked XXX ( $\Delta = 1$ ) numerics to our experimental observation of fractional  $q$  quantum resonances in the QKR, and find excellent agreement. Because the Heisenberg chain in a random magnetic field is a prototype model for traditional MBL,  $U_{\text{kickedXXZ}}$  is well suited to address the question of whether the emergent Floquet pseudo-randomness in a disorder-free kicked system is sufficient to reproduce MBL phenomenology. To numerically probe many-body dynamical localization in the kicked spin model we study the evolution of an initial Néel state ordering  $|\uparrow\downarrow\uparrow\downarrow\dots\rangle$  in the  $M = 0$  sector with multiple spin-flips, and observe long-lived persistence of ordering for sufficiently small  $K$  (Fig. 4F). A transition from MBDL to ergodicity at larger interaction strengths is indicated both by the Néel state persistence (Fig. 4F-G) and by the Floquet level-spacing gap ratio parameter  $\langle r \rangle$  [14, 28] (Fig. 4H). These numerical results signal a true many-body dynamically localized state in a kicked XXZ chain. This indicates a promising path towards experimentally exploring the interplay between quantum chaos and many-body dynamical localization in a variety of quantum simulator platforms [35–37] and highlighting connections between paradigmatic kicked spin models and the quantum kicked rotor.

In conclusion, we have experimentally realized an ensemble of interacting quantum kicked rotors. Following the evolution of interacting samples over hundreds of kicks, we observe an initial prethermal state, followed by an interaction-induced breakdown of dynamical local-

ization via anomalous diffusion which signals the emergence of many-body quantum chaos. Characterization of the departure from the dynamically localized state indicates subdiffusive energy growth with an exponent near 0.5, and reveals momentum space distributions which are not exponentially localized. Measuring Loschmidt echo time-reversal dynamics with a quantum resonance, we have quantitatively probed the role of interaction-induced irreversibility in the emergence of many-body quantum chaos. Finally, we have experimentally verified a mapping between the quantum kicked rotor and kicked spin chains in the single-particle limit, and presented numerical evidence for a many-body dynamically localized phase in the latter. Together these results illuminate the emergence of interaction-driven quantum chaos in a paradigmatic localized system and pave the way for the exploration and application of many-body dynamical localization and disorder-free dynamic stabilization in a broad range of physical contexts.

We acknowledge useful conversations with Adam Rançon, Norman Yao, and Thomas Schuster. During the performance of the research described here we became aware of related efforts underway in another experimental group [38] which have reached similar conclusions using a complementary approach. **Funding:** D.M.W. acknowledges support from the Air Force Office of Scientific Research (AFOSR FA9550-20-1-0240), the Army Research Office (PECASE W911NF1410154), and the National Science Foundation (CAREER 1555313). D.M.W., R.S., and E.N.-M. acknowledge support from the UCSB NSF Quantum Foundry through the Q-AMASE-i program (Grant No. DMR-1906325). V.G. was supported by US-ARO Contract No. W911NF1310172, NSF DMR-2037158, and the Simons Foundation. **Authors' contributions:** A.C., R.S., H.M., E.Q.S., J.L.T., E.N.-M., T.S. and H.E.K. contributed to operating the experiment and performing the measurements. A.C., R.S. and H.M. analyzed the data. A.C. conceptualized and performed the theoretical simulations of rotor and spin models. V.G. and D.M.W. developed the idea for the experiment. D.M.W. supervised the work. A.C., R.S., H.M., V.G. and D.M.W. wrote the manuscript. All authors contributed to discussion and interpretation of the results. **Competing interests:** The authors declare no competing interests. **Data and materials availability:** All data needed to evaluate the conclusions in this study are presented in the paper and in the supplementary materials.

- 
- [1] R. Nandkishore and D. A. Huse, *Annu. Rev. Condens. Matter Phys.* **6**, 15 (2015).
  - [2] D. A. Abanin, E. Altman, I. Bloch, and M. Serbyn, *Rev. Mod. Phys.* **91**, 021001 (2019).
  - [3] P. Ponte, Z. Papić, F. Huveneers, and D. A. Abanin, *Phys. Rev. Lett.* **114**, 140401 (2015).
  - [4] A. C. Keser, S. Ganeshan, G. Refael, and V. Galitski, *Phys. Rev. B* **94**, 085120 (2016).
  - [5] C. Rylands, E. B. Rozenbaum, V. Galitski, and R. Konik, *Phys. Rev. Lett.* **124**, 155302 (2020).
  - [6] M. Fava, R. Fazio, and A. Russomanno, *Phys. Rev. B* **101**, 064302 (2020).
  - [7] D. Bluvstein, A. Omran, H. Levine, A. Keesling, G. Semeghini, S. Ebadi, T. T. Wang, A. A. Michailidis,

- N. Maskara, W. W. Ho, S. Choi, M. Serbyn, M. Greiner, V. Vuletić, and M. D. Lukin, *Science* **371**, 1355 (2021).
- [8] K. Singh, C. J. Fujiwara, Z. A. Geiger, E. Q. Simmons, M. Lipatov, A. Cao, P. Dotti, S. V. Rajagopal, R. Senaratne, T. Shimasaki, M. Heyl, A. Eckardt, and D. M. Weld, *Phys. Rev. X* **9**, 041021 (2019).
- [9] A. Rubio-Abadal, M. Ippoliti, S. Hollerith, D. Wei, J. Rui, S. L. Sondhi, V. Khemani, C. Gross, and I. Bloch, *Phys. Rev. X* **10**, 021044 (2020).
- [10] P. Peng, C. Yin, X. Huang, C. Ramanathan, and P. Cappellaro, *Nat. Phys.* (2021).
- [11] R. Bouganne, M. B. Aguilera, A. Ghermaoui, J. Beugnon, and F. Gerbier, *Nat. Phys.* **16**, 21 (2020).
- [12] S. A. Weidinger and M. Knap, *Sci. Rep.* **7**, 1 (2017).
- [13] K. Agarwal, S. Gopalakrishnan, M. Knap, M. Müller, and E. Demler, *Phys. Rev. Lett.* **114**, 160401 (2015).
- [14] Materials and methods are available as supplementary materials.
- [15] B. V. Chirikov, *Phys. Rep.* **52**, 263 (1979).
- [16] F. L. Moore, J. C. Robinson, C. F. Bharucha, B. Sundaram, and M. G. Raizen, *Phys. Rev. Lett.* **75**, 4598 (1995).
- [17] S. Fishman, D. R. Grempel, and R. E. Prange, *Phys. Rev. Lett.* **49**, 509 (1982).
- [18] D. R. Grempel, R. E. Prange, and S. Fishman, *Phys. Rev. A* **29**, 1639 (1984).
- [19] D. L. Shepelyansky, *Phys. Rev. Lett.* **70**, 1787 (1993).
- [20] G. Gligorić, J. D. Bodyfelt, and S. Flach, *Europhys. Lett.* **96**, 30004 (2011).
- [21] S. Lellouch, A. Rançon, S. De Bièvre, D. Delande, and J. C. Garreau, *Phys. Rev. A* **101**, 043624 (2020).
- [22] J. Liu, C. Zhang, M. G. Raizen, and Q. Niu, *Phys. Rev. A* **73**, 013601 (2006).
- [23] A. Ullah and M. D. Hoogerland, *Phys. Rev. E* **83**, 046218 (2011).
- [24] J. Martin, B. Georgeot, and D. L. Shepelyansky, *Phys. Rev. Lett.* **100**, 044106 (2008).
- [25] W. H. Oskay, D. A. Steck, and M. G. Raizen, *Chaos, Solitons and Fractals* **16**, 409 (2003).
- [26] A. S. Pikovsky and D. L. Shepelyansky, *Phys. Rev. Lett.* **100**, 094101 (2008).
- [27] S. Flach, D. O. Krimer, and C. Skokos, *Phys. Rev. Lett.* **102**, 024101 (2009).
- [28] L. D'Alessio and M. Rigol, *Phys. Rev. X* **4**, 041048 (2014).
- [29] V. Vuatelet and A. Rançon, Effective thermalization of a many-body dynamically localized bose gas (2021), arXiv:2103.14388 [cond-mat.quant-gas].
- [30] E. B. Rozenbaum, S. Ganeshan, and V. Galitski, *Phys. Rev. Lett.* **118**, 086801 (2017).
- [31] T. Gorin, T. Prosen, T. H. Seligman, and M. Žnidarič, *Phys. Rep.* **435**, 33 (2006).
- [32] M. Lepers, V. Zehmlé, and J. C. Garreau, *Phys. Rev. A* **77**, 043628 (2008).
- [33] T. Boness, S. Bose, and T. S. Monteiro, *Phys. Rev. Lett.* **96**, 187201 (2006).
- [34] T. Boness, K. Kudo, and T. S. Monteiro, *Phys. Rev. E* **81**, 046201 (2010).
- [35] C. Monroe, W. C. Campbell, L.-M. Duan, Z.-X. Gong, A. V. Gorshkov, P. W. Hess, R. Islam, K. Kim, N. M. Linke, G. Pagano, P. Richerme, C. Senko, and N. Y. Yao, *Rev. Mod. Phys.* **93**, 025001 (2021).
- [36] A. Browaeys and T. Lahaye, *Nat. Phys.* **16**, 132 (2020).
- [37] Y. Salathé, M. Mondal, M. Oppliger, J. Heinsoo, P. Kurpiers, A. Potočnik, A. Mezzacapo, U. Las Heras, L. Lamata, E. Solano, S. Filipp, and A. Wallraff, *Phys. Rev. X* **5**, 021027 (2015).
- [38] J. Toh, *et al*, manuscript in preparation. (2021).
- [39] S. E. Pollack, D. Dries, M. Junker, Y. P. Chen, T. A. Corcovilos, and R. G. Hulet, *Phys. Rev. Lett.* **102**, 090402 (2009).
- [40] P. Deuar and P. D. Drummond, *Phys. Rev. Lett.* **98**, 120402 (2007).
- [41] A. Tenart, C. Carcy, H. Cayla, T. Bourdel, M. Mancini, and D. Clément, *Phys. Rev. Res.* **2**, 013017 (2020).
- [42] M. Rigol, V. Dunjko, and M. Olshanii, *Nature* **452**, 854 (2008).
- [43] B. Gadway, D. Pertot, R. Reimann, M. G. Cohen, and D. Schneble, *Opt. Express* **17**, 19173 (2009).
- [44] Y. B. Ovchinnikov, J. H. Müller, M. R. Doery, E. J. D. Vredenbregt, K. Helmersen, S. L. Rolston, and W. D. Phillips, *Phys. Rev. Lett.* **83**, 284 (1999).
- [45] B. Klappauf, W. Oskay, D. Steck, and M. Raizen, *Physica D* **131**, 78 (1999), classical Chaos and its Quantum Manifestations.
- [46] S. Fishman, I. Guarneri, and L. Rebuzzini, *J. Stat. Phys.* **110**, 911 (2003).
- [47] I. Dana and D. L. Dorofeev, *Phys. Rev. E* **73**, 026206 (2006).
- [48] L. M. Sieberer, T. Olsacher, A. Elben, M. Heyl, P. Hauke, F. Haake, and P. Zoller, *npj Quantum Inf.* **5**, 1 (2019).
- [49] N. Goldman and J. Dalibard, *Phys. Rev. X* **4**, 031027 (2014).

## Supplementary Materials

### CONTENTS

1. Materials and Methods	7
1.1. Experimental platform and sequence	7
1.2. Delocalization data analysis	8
1.3. Loschmidt experimental sequence and data analysis	9
1.4. Noninteracting QKR numerics	10
1.5. Kicked XXZ model numerics	10
2. Supplementary Text	11
2.1. Additional Delocalization Data	11
2.2. Monte Carlo distributions for exponential localization deviation	12
2.3. Systematics: Finite pulse width	12
2.4. Systematics: Position space dynamics and TOF conversion	13
2.5. Systematics: Beam-induced transverse dynamics	15
2.6. Systematics: Effects of scattering on measured Loschmidt fidelity	15
2.7. Interpretation of the kicking in the spin chain mapping	16
2.8. MBDL for anisotropic kicked XXZ chains	17

### 1. MATERIALS AND METHODS

#### 1.1. Experimental platform and sequence

The experiments begin with a Bose-Einstein condensate (BEC) of around  $10^5$   ${}^7\text{Li}$  atoms in a far-detuned optical dipole trap with trapping frequencies  $\omega_{x,z}/2\pi \approx 40$  Hz and  $\omega_y/2\pi \approx 56$  Hz, where  $z$  is the axis of the optical lattice,  $y$  is the direction of gravity, and  $x$  is the remaining orthogonal axis. The condensate is produced by optical evaporation at an s-wave scattering length of  $a = 240a_0$ , set by an applied magnetic field in the vicinity of the broad Feshbach resonance at 737 Gauss [39]. Immediately after evaporation, the fields are ramped to their desired value over 60-90 ms and maintained for the remainder of the experiment. The dipole trap is then extinguished and the BEC repeatedly subjected to a pulsed 1D optical lattice with lattice constant  $d = 532$  nm, laser wave vector  $k_L = \pi/d$ , and recoil energy  $E_R = \hbar^2 k_L^2/2m$  with  $m$  the mass of  ${}^7\text{Li}$ . The full dynamics are then well described by the second-quantized Hamiltonian

$$\mathcal{H} = \int d^3r \hat{\Psi}^\dagger(\mathbf{r}, t) H(\mathbf{r}, t) \hat{\Psi}(\mathbf{r}, t) + \frac{g}{2} \int d^3r \hat{\Psi}^\dagger(\mathbf{r}, t) \hat{\Psi}^\dagger(\mathbf{r}, t) \hat{\Psi}(\mathbf{r}, t) \hat{\Psi}(\mathbf{r}, t) \quad (\text{S1})$$

$$H(\mathbf{r}, t) = \frac{p^2}{2m} + \frac{V_0}{2} \cos(2k_L z) I(x, y) \sum_n f_\tau(t - nT). \quad (\text{S2})$$

The key kick parameters are the lattice depth  $V_0$ , effective pulse width  $\tau$ , and kick period  $T$ .  $V_0$  is calibrated through a standard Kapitza-Dirac diffraction technique.  $f_\tau(t)$  denotes a unit amplitude pulse function beginning at  $t = 0$  of width  $\tau$ . The experimental pulse is approximated by a piecewise function with a linear rise and fall of 200 ns duration before and after a plateau of variable hold time. For the experimental data in the main text with  $\tau = 300$  ns between the half-maximum points, this hold duration is 100 ns. The scattering length  $a$  determines the two-body coupling coefficient  $g = 4\pi\hbar^2 a/m$ . Here  $I(x, y)$  denotes the transverse intensity profile of the lattice beams normalized to unity maximum; this is approximately Gaussian  $I(x, y) \approx e^{-2(x^2+y^2)/\sigma^2}$  with a measured  $1/e^2$  beam radius of  $\sigma \approx 65$   $\mu\text{m}$ . The total duration of kicking is at most 1 ms for our longest experiments, significantly shorter than the 4 ms it takes the BEC to fall under the influence of gravity through the lattice beam waist.

To measure the momentum distribution, we perform absorption imaging of the atoms after free expansion. The time-of-flight (TOF) duration is 3.5 ms for the delocalization data and 2 ms for the Loschmidt data. Due to the low mass of  ${}^7\text{Li}$  and the breadth of the Feshbach resonance, coil inductance prevents sweeping the magnetic fields to the noninteracting regime for this expansion period. This means additional scattering occurs during expansion, which

may lead to systematic errors in the measured quantities (see section 2.6 of this document). For the energy, we are able to account for this scattering in our analysis due to the energy-conserving nature of the collisions. For metrics such as the IPR, this systematic is challenging to avoid. However by tracking the evolution of these observables as a function of kick number at a fixed TOF duration, we can largely attribute the qualitative observed dynamics to the evolution under the Hamiltonian (S1) as opposed to the expansion. At large  $n$ , the majority of scattering happens during the kicking duration so expansion effects become negligible.

## 1.2. Delocalization data analysis

This section discusses the analysis behind Fig. 2. Because the momentum distributions of the interacting samples change significantly over the course of the delocalization experiments, the quantities shown in Fig. 2 are computed directly from raw or averaged images as opposed to fitting procedures. However, this can make measurable quantities such as energy sensitive to noise, especially near the edge of the camera sensor due to the quadratic weighting. To maximize the signal-to-noise ratio in our measurement, we analyze raw images using an adaptive region-of-interest (ROI). First, a single base ROI capturing all detectable atoms at all times is created for each interaction strength. The integrated density in this ROI is used to post-select images with total atom numbers falling within a  $\pm 10\%$  window of the mean, in order to reduce variations in the interaction energy, which depends directly on atom density. For these data we take 10 images at each kick number, of which typically 4-7 are discarded by this post-selection procedure. The ROI boundaries at each kick number are then determined by the points at which the cumulative summed distributions of the averaged image outward from a center point reach a threshold value. The thresholds are set empirically and the boundaries obtained by the following procedure. First we compute the transverse bound by integrating out the entire axial direction to get the overall transverse distribution, find the point it crosses an 85% threshold and then expand the resulting boundary by a factor of 1.5 (1.2 in the supplementary delocalization data of section 2.1) to ensure all atoms are captured. We then compute an axial boundary going point by point along the transverse direction; at each transverse point we integrate over 10 neighboring transverse pixel rows to get a ‘‘local’’ axial distribution, find the point it crosses a 99.8% threshold and expand by a factor 1.15. Finally we smooth each ROI boundary and take a moving average across different kick numbers (4 on each side). Crucially, we have confirmed that the qualitative observation of delocalization is not significantly altered from the simple case where we use just the initial single base ROI across all shots. However, the details of the trends should be more accurately captured by the adaptive procedure because the signal-to-noise ratio over the ROI is optimized at each kick number. All measurable quantities are then calculated from the imaged densities within this region.

Since we do not observe any substantial atom loss during the kicking duration, we treat the imaged atomic densities as normalized distributions. For Figs. 2A-B, we compute the measured quantities from individual experimental runs and then average the results, with the reported error bar as the standard error of the mean. For Fig. 2I, we instead compute the averaged distributions first before computing the deviation from exponential localization; the errorbars are computed from a Monte-Carlo simulation of the uncertainty in  $k_{\text{loc}}$  discussed later in this section. A smoothing filter is applied to the displayed densities in Figs. 2C-H for visual clarity, but not in the subsequent calculation of the localization deviation in Fig. 2I.

To measure the energy, we compute the post-expansion spatial variance of the distribution in both the kicking  $z$  and transverse  $x$  directions of the image. Assuming cylindrical symmetry, the kinetic energy is then calculated as  $m((\langle z^2 \rangle + 2\langle x^2 \rangle) / 2t_{\text{TOF}}^2)$  with  $t_{\text{TOF}} \approx 3.5$  ms (see section 2.4 for a discussion of possible corrections to the conversion of position to energy). For an accurate measurement of the interacting samples, inclusion of the transverse energy is necessary to account for energy-conserving scattering processes that occur both during the kicking and TOF. In addition, the inhomogeneous intensity profile of the beam  $I(x, y)$  leads to a transverse energy oscillation in all samples including the noninteracting ones (see section 2.5). Since we are not interested in this effect, we remove it to leading order by subtracting off the noninteracting transverse energy from each trace, so that the noninteracting energy is purely the kinetic energy along the kicking direction. To compute the error bars on the interacting data, we add the error of the total interacting energy and noninteracting transverse energy in quadrature. The single-particle localization energy  $E_{\text{loc}}$  is estimated by averaging the noninteracting trace for  $n \geq 100$ , and the reported uncertainty is based on the standard deviation of those points. We note that this uncertainty is not only due to experimental imperfections, but also due to natural dynamical fluctuations, as evidenced by the results of noninteracting simulations like those shown in Fig. S3.

We compute an effective 1D momentum-space IPR by first integrating out the transverse dimension and then summing the squares of the subsequent normalized axial density. We confirmed that this qualitatively matches the result of directly integrating the squared 2D distribution while largely eliminating the beam-induced transverse oscillation. Specifically for computing this metric, we apply a smoothing filter to the normalized densities consistently across all 3 interaction strengths. This suppresses high-frequency background noise which sets a lower bound on

the measurable IPR due to the squaring procedure. The measured values are compared to two predictions based on an exponentially localized distribution. The blue shaded region is obtained by numerically computing the IPR for the momentum space distribution  $\exp(-|k|/k_{\text{loc}}) \sum_j \exp(-(k - 2k_{L,j})^2/w^2)$ , which models a Gaussian comb with an exponential envelope. This is a reasonable expectation for a finite-size, localized noninteracting condensate occupying only discrete momentum modes. The width parameter  $w$  is measured from fitting the  $n = 0$  noninteracting condensate and takes into account the momentum-space resolution of the TOF given the finite condensate spatial extent. The width of the region is based on Monte Carlo simulation of uncertainty in  $k_{\text{loc}}$ , where the resulting distribution is fit to a Gaussian to extract the mean and standard deviation. The green shaded region is calculated analytically for a pure exponential distribution of infinite extent and is given by  $1/4k_{\text{loc}}$ . Taking into account the finite width of the imaging region changes the distribution normalization and leads to the following correction factor  $(1 - \exp(-2k_0/k_{\text{loc}}))/(1 - \exp(-k_0/k_{\text{loc}}))^2$ ; here  $k_0 \approx 9.85k_L$  is the half-width of our images which yields a negligible correction factor of  $\approx 1.006$ . The width of the region is computed through linearized error propagation.

In Fig. 2I, the plotted localization metric is  $\int_{-k_0}^{k_0} \max[r(k) - 1, 0] dk / 2k_0$ . Here,  $r(k) = |\psi(k)|^2 / \exp(-k/k_{\text{loc}})$  is the ratio of the measured axial density denoted  $|\psi(k)|^2$  and an exponential localization envelope. Here the maximum of  $|\psi(k)|^2$  is set to unity. Taking the maximum of  $r(k) - 1$  and 0 ensures that the result is only sensitive to regions of the distribution which decay more slowly than exponentially. That is, it interprets 0 as “at least exponentially” localized with respect to a given localization length, and thus characterizes departures from a given dynamically localized state in the traditional sense of exponentially localized wavefunctions. We note however that the system remaining exponentially localized but with a larger localization length would result in a non-zero value for this metric, which motivates the direct inspection of the distributions in Figs. 2F-H. The reported values and errorbars are extracted by propagating a Gaussian uncertainty in the measured  $k_{\text{loc}}$  through a Monte-Carlo simulation. We find that the resulting distributions interpolate between sharply peaked at 0 with a rapid fall-off when well-localized, to positively skewed with non-zero peak in the delocalized regime. We empirically find that a log-normal distribution fits the Monte Carlo result well, and we use this fit to extract the data reported in Fig. 2I. In particular, the markers indicate the mean of the distribution and the errorbars represent the interquartile range containing the central 50% of the distribution. Because of the skewness, we investigate the Monte Carlo simulated distributions in more detail in section 2.2.

### 1.3. Loschmidt experimental sequence and data analysis

Here we discuss the methods and analysis used to produce Fig. 3. The Loschmidt experiments begin similarly to the previously described sequence; for an  $N$  kick Loschmidt sequence, the BEC is first kicked  $N/2$  times near quantum resonance at the parameters  $V_0 \approx 50E_R$ ,  $\tau = 300$  ns, and  $T = 9.93$   $\mu$ s. For this data, we adjusted the lattice depth  $V_0$  for different interaction strengths to achieve the same amount of absorbed energy after the first  $N/2$  kicks. This compensates for a decrease in energy absorption at the same lattice depth for higher interaction strengths, which we attribute to the increase of the Thomas-Fermi radius of the BEC relative to the lattice beam size. Neglecting this effect would artificially enhance the fidelity at very large interaction strengths due to a reduction in the effective stochasticity parameter  $K$ . We plot the zero mode fraction after the first  $N/2$  kicks without time-reversal (denoted  $F'$  Gauss) in Fig. S6 to benchmark this kicking amplitude normalization procedure.

After the first  $N/2$  kicks, we wait a half period  $T/2$  to shift the wavefunction spatially by half a lattice spacing, causing the sign of subsequent kicks to be reversed. We then apply another sequence of  $N/2$  kicks using the same lattice parameters to complete the echo sequence. The time series in Fig. 3C-E show absorption images averaged over 5 shots for each kick number  $n$  in a  $N = 10$  experiment. Since we begin with a zero-momentum condensate mode, to measure the Loschmidt fidelity we simply need to count the fraction of atoms remaining in this mode. While atoms in other momentum modes coupled by the lattice are easily distinguished, atoms that have undergone scattering events into a smeared-out background distribution are not always well-separated. Thus, to extract the return fraction we fit the axial atomic distribution around the zero-momentum mode with a pair of Gaussians of varying width. The narrower Gaussian accounts for atoms remaining in the zero-momentum condensate after expansion, while the broader Gaussian measures the atoms that have been collisionally ejected from the condensate [40, 41]. In Fig. 3B, we show the fraction of atoms remaining in the narrow Gaussian and use this quantity as an estimate of the Loschmidt fidelity. Scattering during the expansion means that this necessarily underestimates the true fidelity, a possibility further addressed in section 2.6.

#### 1.4. Noninteracting QKR numerics

One-dimensional simulations of the noninteracting kicked rotor problem for comparison with experimental data are executed in two ways. We either perform a split-step Fourier integration of the QKR Hamiltonian (S2) (ignoring the transverse distribution  $I(x, y)$ ) to model the finite-width pulse shapes, or iterate the QKR Floquet map described in the main text. The simulations are typically performed with periodic boundary conditions over a single lattice site (except when modeling the TOF readout; see section 2.4). We perform a Gaussian sampling of quasimomenta with standard deviation  $\sim 0.1k_L$ , in rough accordance with the measured BEC temperature of around 10-15 nK. For simulation of the stochastic kicking protocol, we use the same techniques and additionally average over 100 different realizations of the fluctuations (note this is slightly different than in the experiment where a single kick period disorder realization is used).

#### 1.5. Kicked XXZ model numerics

To investigate the mapping between spin chains and kicked quantum rotors and the possibility of many-body dynamical localization in kicked XXZ chains, we perform exact diagonalization of  $U_{\text{kickedXXZ}}$  on systems of length up to  $L = 14$ . We center the chains about  $j = 0$  (i.e.  $j \in [1 - L, L - 1]/2$ , integer for  $L$  odd and half-integer for  $L$  even) and consider open boundary conditions. Reflection symmetry about the center of the chain can be removed by inclusion of a non-zero fluctuation in the field-center  $\beta$ .

In Fig. 4F, the time average of an observable  $O$  after  $n$  cycles is straightforwardly defined as  $\langle O \rangle_n = \left( \sum_{i=1}^n \langle \psi | U_{\text{kickedXXZ}}^{\dagger i} O U_{\text{kickedXXZ}}^i | \psi \rangle \right) / n$ . The long-time limit of this quantity in Fig. 4G is calculated via the Floquet diagonal ensemble as  $\lim_{n \rightarrow \infty} \langle O \rangle_n = \sum_{\alpha} |c_{\alpha}|^2 \langle \psi_{\alpha} | O | \psi_{\alpha} \rangle$ . Here  $c_{\alpha} = \langle \psi_{\alpha} | \psi \rangle$  are the coefficient of the initial state  $|\psi\rangle$  in the basis of the many-body Floquet states  $|\psi_{\alpha}\rangle$  obtained from diagonalization of the Floquet map  $U_{\text{kickedXXZ}}$  [42].

The gap ratio is defined as  $r_{\alpha} = \min(\delta_{\alpha}, \delta_{\alpha+1}) / \max(\delta_{\alpha}, \delta_{\alpha+1})$ , where  $\delta_{\alpha} = \epsilon_{\alpha+1} - \epsilon_{\alpha}$  is the gap between consecutive quasi-energies and  $\epsilon_{\alpha}$  are the quasi-energies. The  $\epsilon_{\alpha}$  are ordered in the interval  $[-\pi, \pi]$  prior to extracting the gaps and gap-ratios. To compute  $\langle r \rangle$  in Fig. 4H, we average  $r_{\alpha}$  over the  $M = 0$  sector as well as for 100 values of  $\beta$  drawn from a normal distribution of standard deviation 0.1. The Hilbert-space size of this sector for  $L = 14$  is 3432. We note that we avoid the exact  $K = 0$  point for gap-ratio calculations.

## 2. SUPPLEMENTARY TEXT

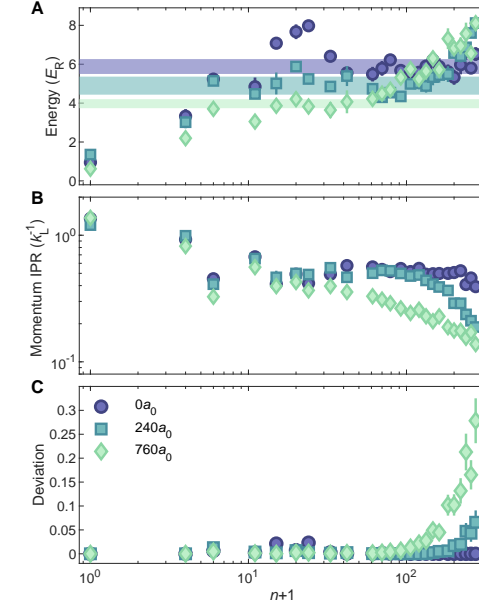


Fig. S1. **Interaction-induced delocalization for a different set of kicking parameters.** The kick parameters are  $V_0 = 70 E_R$ ,  $T = 2.2 \mu\text{s}$  and  $\tau = 300 \text{ ns}$  ( $K \approx 4.6$  and  $k \approx 2.8$ ). The (A) energy, (B) 1D momentum-space IPR and (C) deviation from exponential localization over time for varying scattering lengths. In A, the shaded regions indicate the extracted initial localization lengths for the three interaction strengths which we use for computing C.

## 2.1. Additional Delocalization Data

To supplement the dynamical delocalization signals shown in Fig. 2 and demonstrate that this is not a particularly fine-tuned phenomena in the kicking parameter space, in Fig. S1 we show the same metrics for a larger kicking period  $T = 2.2 \mu\text{s}$ . The overall picture is unchanged, as the interacting samples show starkly different behavior from the noninteracting traces, departing from the localized value of each metric after a variable break time. Here the energy delocalization is obscured slightly as the different interaction strengths seem to initially localize to different energies. We attribute this partly to Thomas-Fermi expansion which reduces both the effective lattice depth experienced by the condensate and the initial kinetic energy of the sample, though we do not entirely rule out the possibility of different early-time prethermal behavior across interaction strengths. The correlation between localization length and quasimomentum spread is observed in noninteracting numerics. The different-colored shaded regions indicate our best estimates for the different localization energies at the 3 interaction strengths by computing the mean energy (and standard deviation) over windows of  $n$  where the data are minimally changing. These values are used to compute the exponential localization deviation in Fig. S1C. We do note a small trend visible at the end of the noninteracting traces; numerics suggest that this is consistent with variations in the localization length that occur over time for certain kicking parameters.

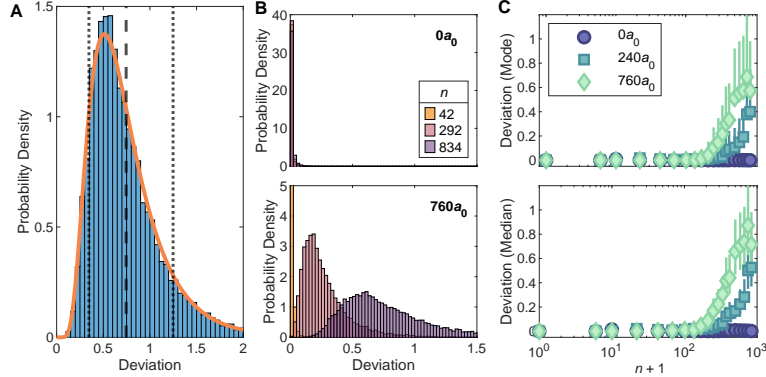


Fig. S2. **Characterizing Monte Carlo distributions for deviation from exponential localization.** (A) Distribution for the  $760a_0$  data in Fig. 2 at  $n = 500$ . Orange line indicates the fit to a log-normal distribution. Vertical dashed line indicates the mean, and the vertical dotted lines surrounding it indicate the interquartile range reported as the errorbars. (B) Evolution of the distribution over time for noninteracting and interacting samples. Note the difference in y-scale. The  $n = 42$  trace in the lower panel is cut-off vertically for visual clarity on the larger  $n$  distributions. (C) Alternative characterizations of the exponential localization deviation in terms of the mode and median of the simulated distributions (indicated by the markers, the errorbars are left as the interquartile range), as opposed to the mean shown in the main text Fig. 2I.

## 2.2. Monte Carlo distributions for exponential localization deviation

In Fig. S2, we show further details on the Monte Carlo simulated distributions for quantitatively characterizing the deviation from exponential localization in Figs. 2I and S1C (in particular this data corresponds to Fig. 2I). The distributions are generated by computing the defined deviation parameter for  $10^4$  values of  $k_{loc}$  drawn from a Gaussian centered at  $1.58k_L$  and with standard deviation  $0.12k_L$ . An example distribution for a sample which has delocalized is shown in Fig. S2A, clearly showing the skewed probability densities we obtain from this procedure. The solid orange line indicates the log-normal distribution fit we use to extract parameters such as the mean and interquartile range of the distribution. We note that the use of a log-normal distribution here is only motivated empirically as a systematic method to determine such quantities.

In Fig. S2B, we contrast how these simulated distributions evolve in time for localized noninteracting samples and delocalizing interacting ones. In the noninteracting case, the distributions are extremely sharply peaked at 0 and are relatively unchanging in-time, agreeing with the expectation of dynamical localization. In the latter however, the distribution is only peaked at 0 for short times indicative of the finite duration prethermal plateau we report, and gradually shifts away to non-zero values as the sample heats up. Importantly, at the later times the  $760a_0$  distribution has essentially vanishing probability density at 0 deviation, allowing us to confidently claim observation of departure from exponential localization. In Fig. S2C, we confirm that the reported behavior of deviation over time in Fig. 2I would not qualitatively change if we instead used the median or mode of the distribution instead of the mean.

## 2.3. Systematics: Finite pulse width

The delta-function kicking assumption in the theoretical QKR model is not perfectly realized in experiment owing to the finite atomic mass of  ${}^7\text{Li}$ . The assumption corresponds to the Raman-Nath diffraction regime which is approximately expressed by the condition  $2\sqrt{V_0}E_R\tau/\hbar \ll 1$  [43]. For the experiment with  $\tau = 0.3 \mu\text{s}$  and  $V_0 = 64E_R$  as in Fig. 2, this parameter is approximately 0.76 (there is an ambiguity of a factor  $2\pi$  in defining the condition [44], which would reduce the parameter to 0.12). Either way, this suggests that the system is in between the Raman-Nath and Bragg diffraction regimes and thus finite-pulse-width effects require careful investigation.

We numerically explore the effects of realistic pulse duration on single-particle QKR localization by comparing square pulse simulations of varying pulse width  $\tau$  to the delta-kick Floquet map solution. To make this comparison, we keep the effective stochasticity parameter  $K \sim V_0\tau$  characterizing the kicking strength constant as we let  $\tau \rightarrow 0$ . Results for two values of  $K$  are shown in Fig. S3. In general, we find that larger pulse duration tends to decrease

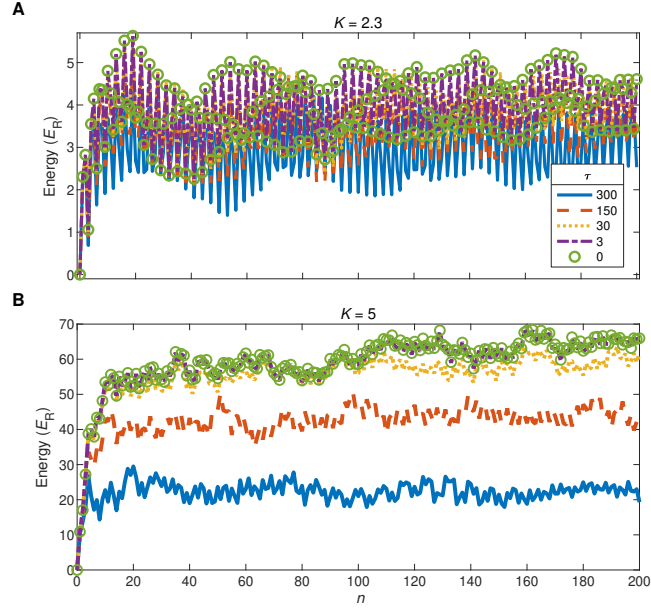


Fig. S3. **Effects of finite pulse width on noninteracting QKR localization.** (A) Time evolution of energy for  $K = 2.3$ . The  $\tau = 300$  ns trace is comparable to the data in the main text. (B) Equivalent simulation for  $K = 5$ . The relative difference in localization energy between the achievable finite pulse durations in our experiment and the delta-kick limit becomes much more substantial at larger  $K$ .

the localization energy, which from a classical perspective corresponds to a particle traversing a significant part of the cosine potential during the kick and thus feeling a smaller effective impulse. This effect depends on the value of  $K$  which determines the extent to which higher momentum modes are excited in the localized state. The many-body delocalization data in the main text was taken around  $K \approx 2.3$ . These simulations indicate that for this data there is a roughly 20% decrease in the measured noninteracting localization energy with respect to the delta-kick limit.

The finite pulse duration can be thought of as leading to an effective kicking strength which decays with increasing momentum, causing even the classical phase space to localize above a certain momentum [45]. This is an important consideration in probing the destruction of the quantum dynamical localization which occurs in the classically chaotic regime. For our parameters, the estimate given in [45] for the momentum boundary between classically chaotic and integrable regions due to pulse width is roughly  $\pm 33.2k_L$ , which is much larger than any excitation we observe in the data for Fig. 2 and S1. Thus we do not expect that the finite pulse duration qualitatively affects the observed delocalization dynamics.

We note that the reduction of absorbed energy by finite pulse width does play a practical role in determining which sets of system/kicking parameters are amenable to observation of interaction-induced delocalization. Because collisional processes are proportional to real-space density-density overlaps between different momentum modes, for a poor choice of kicking parameters a strong excitation of higher momentum modes in conjunction with real-space expansion (discussed in the next section) may rapidly dilute the system, and yield an effectively non-interacting sample before the interaction-induced delocalization break time.

#### 2.4. Systematics: Position space dynamics and TOF conversion

From a theoretical perspective, the difference between open and periodic boundary conditions in the single-particle QKR is resolved by Bloch's theorem [46, 47]. Different quasimomenta evolve independently, manifesting different

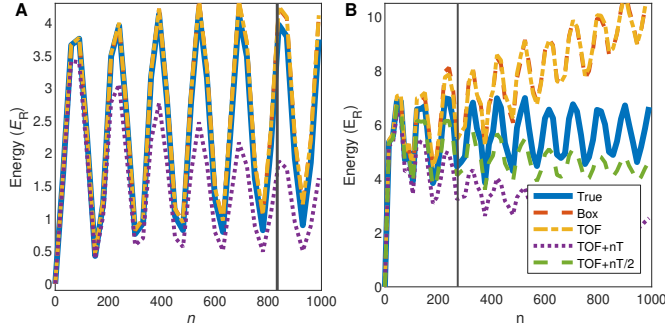


Fig. S4. **Effects of position-space dynamics on extracting energy from TOF images.** Noninteracting numerical simulations comparing different methods for measuring energy in TOF and the true energy of the kicked rotor. **(A)** The kicking parameters are comparable to the ones used in the main text ( $T = 1.2\mu\text{s}$  and  $\tau = 300\text{ns}$ ), but with lattice depth reduced to  $V_0 = 38E_R$  to compensate for modeling only delta function kicking. We expect that the strong oscillations shown here are largely washed out in the experimental data by effective averaging over kicking strengths due to transverse extent of the condensate and fluctuations in the beam intensity from run-to-run. The traces here are sampled every 30 kicks for visual clarity, and the energy actually fluctuates at a much higher frequency. This simulation reveals that for the main data, the correct energy is straightforwardly extracted by simply using the TOF time to convert position to momentum. The vertical line indicates the max kick number reached in the data. **(B)** A similar simulation but with  $T = 2.2\mu\text{s}$  roughly corresponding to the supplementary delocalization data in Fig. S1 (with adjusted lattice depth  $V_0 = 52E_R$ ). To illustrate the potential pitfalls of the readout method, here we model a TOF duration of only 2 ms, as opposed to the 3.5 ms used in the experiment. In this case, using only the TOF time in the velocity conversion leads to a false delocalization signal at late times. Instead, we show that an additional method using the TOF duration plus half the kicking time leads to the most faithful representation of the QKR energy for the longest time. We chose to use this conversion in the analysis of S1, though our simulations do not indicate a large difference between these two methods when modeling the full 3.5 ms TOF and restricting only to the max kick number indicated by the vertical line. Here the sampling is every 15 kicks for visual clarity.

realizations of pseudo-randomness in the Anderson model mapping. The connection between the theoretical QKR and kicked quantum gas experiments is made by considering ensemble averages over quasimomenta. However, in practice, experimental readout of the kinetic energy even in the noninteracting case can be further complicated by spatial motion in a non-compact position variable during the course of the kicking. This effect was largely negligible for many previous QKR realizations using heavy atomic species and/or short kicking durations, but in these experiments using light  ${}^7\text{Li}$  atoms and large kick numbers, careful consideration of the effect is required for an accurate energy measurement. Ideally, one would simply extend the TOF duration to suppress such effects, but technical limitations associated with the imaging procedure mean that this cannot be done indefinitely.

In interpreting the TOF absorption images as momentum space distributions, one must convert pixel position to velocity by dividing by an appropriate time. Without spatial motion, the correct time is trivially just the TOF duration. With spatial motion, a strict lower bound on the velocity conversion is set by the combined duration of the kicking and TOF which is equivalent to the assumption that each momentum mode propagates ballistically for the entire course of the experiment, ignoring the reshuffling of momentum modes by repeated kicking. To determine which conversion scheme leads to the most accurate energy measurement, we simulate the delta-function QKR model with an extended position space variable to model the TOF expansion explicitly. We are then able to compare the exact energy with various position-to-velocity conversions to determine the best metric.

Simulations for different kicking parameters and TOF durations are shown in Fig. S4A and B, revealing that in fact the simplest approach of using the TOF to convert position to momentum works well for the parameters of the experiments reported in the main text. For experiments at other parameter values, however, the appropriate conversion can change. In Fig. S4A corresponding to the main data, we show that simply using the TOF as a conversion factor matches the true energy. For the simulations in S4B, however, adding in half of the kicking duration gives a substantially more accurate approximation of the true energy than the simple TOF conversion, which produces a false delocalization signal at longer times. We also examine “box”-counting schemes where the image is instead binned into discrete modes which are multiples of  $2k_L$  momentum, though the added complexity of this scheme is not justified by the results.

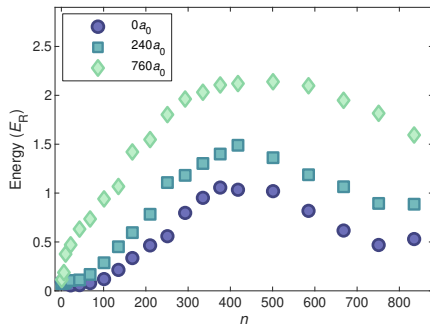


Fig. S5. **Transverse dynamics in experimental quantum kicked rotors.** Measured transverse kinetic energy versus time for the main delocalization data in Fig. 2. Each interaction strength undergoes an oscillation due to harmonic motion in the time-averaged lattice potential. The difference in evolution among different interaction strengths is due to scattering effects.

### 2.5. Systematics: Beam-induced transverse dynamics

While the main concern of QKR experiments is with momenta along the lattice direction, our experiments are three-dimensional and degrees of freedom transverse to the lattice beam cannot in general be ignored especially in the presence of scattering. In Fig. S5, we explicitly show the measured *transverse* kinetic energy for the main delocalization data in the text. Here we can see all three interaction strengths undergoing an oscillation in their transverse energy, which can be interpreted simply as harmonic motion in the time-averaged intensity distribution of the pulsed Gaussian lattice beam. The clear difference in the evolution between the different interaction strengths indicates the effects of 3D scattering for a system with uniform  $I(x, y)$ . As discussed in the Methods section 1.2, this motivates inclusion of the difference between the noninteracting and interacting transverse energy traces in the plotted energy of Fig. 2. We have separately confirmed that ignoring the transverse dynamics altogether does not eliminate the observed delocalization signal.

### 2.6. Systematics: Effects of scattering on measured Loschmidt fidelity

Readout of the momentum distribution of interacting samples can be complicated by scattering during the TOF, and this particularly impacts the measurements of metrics such as IPR and return probability  $F$ , where the signatures of scattering events occurring at different stages of the experiment (i.e. during the lattice pulse trains versus during the time-of-flight) are not easily extracted from the resulting distribution. Here we examine how scattering affects the reported Loschmidt echo return probability shown in Fig. 3. In Fig. S6 we present a comparison of two different methods for measuring the fidelity, which we argue should bound the true value and indicate the effect of this systematic. The *Gaussian fitting* method was described in the methods section 1.3 and presented in Fig. 3. The *raw counting* method computes the fidelity by integrating the raw distribution in a  $\pm k_L$  width around the central mode. If all the scattering occurs prior to the TOF, then the *Gaussian fitting* method is the appropriate counting procedure, as it discards all scattered atoms and only counts the remaining zero-order atoms. If, however, the majority of scattering occurs during the TOF, then this population should be included in the return probability, and so the *raw counting* method would more accurately reflect the true fidelity.

In Fig. S6A, we compare these two methods before (red) and after (blue) the application of the time-reversal kicks, as a function of scattering length. In both cases we find that the *raw counting* method measures a higher fidelity than the *Gaussian fitting* method due to accounting for the scattered population. As expected, the two converge in the noninteracting limit where the overall scattered population vanishes, but become different as the scattering length and consequently the scattered fraction increase (the dependence of scattered fraction on scattering length is plotted in Fig. S7). This behavior of the *Gaussian fitting* and *raw counting* methods is consistent with the limits of validity expected for each, and supports the claim that the two methods bound the systematic measurement error in counting the zero-order population that results from scattering during the TOF.

Having established approximate bounds for the true fidelity as a function of scattering length, we further remark that both methods produce a time-reversed fidelity which exhibits a crossover in behavior as a function of scattering

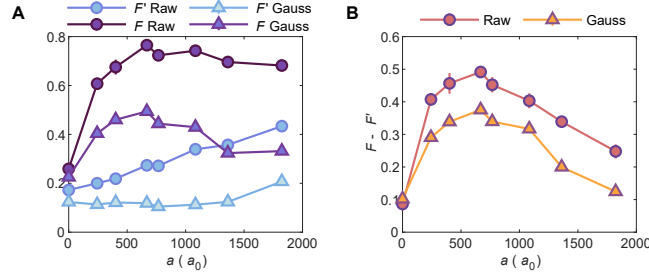


Fig. S6. **Comparison of atom counting methods for Loschmidt fidelity.** (A) Zero mode fraction measured at the halfway point ( $F'$ ) and at the end ( $F$ ) of an 8-kick Loschmidt echo protocol for both raw and Gaussian counting methods. (B) The difference in zero mode fraction between  $F$  and  $F'$  in an 8-kick Loschmidt echo protocol for both methods.

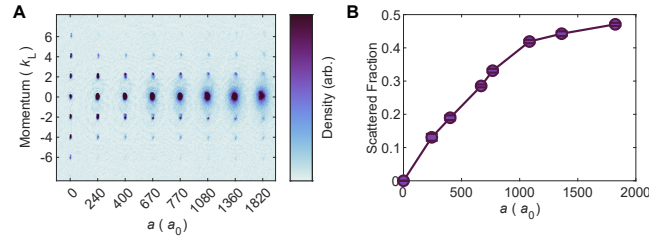


Fig. S7. **Experimentally measured scattered fraction during Loschmidt experiments.** (A) TOF absorption images of a BEC after an  $N = 8$  Loschmidt protocol at various scattering lengths. (B) Corresponding scattered fraction as computed using the *Gaussian fitting* described in the methods section 1.3.

length. The fidelity as a function of  $a$  grows with weak interactions, and it becomes constant, or even decreases, as a function of  $a$  with stronger interactions. We note also that imperfect calibration of the effective kicking strength could give rise to errors in the measured return fidelity. In Fig. S6B, we attempt to account for this effect across the two methods by considering the difference in fidelity before and after the set of time-reversal kicks. This produces two curves of similar functional form, further supporting our observation of a crossover into interaction-induced irreversibility.

## 2.7. Interpretation of the kicking in the spin chain mapping

For the single-particle QKR, it is standard to consider periodic pulsing of the spatial potential separated by intervals of free kinetic energy evolution. In the spin-chain mapping, this corresponds to pulsed spin-exchange interactions and free evolution in a quadratic magnetic field. In the main text, we describe the exact mapping of the QKR parameters  $K$  and  $\hbar$  in  $U$  to the spin model  $U_{\text{kickedXXZ}}$ , but instead take the interpretation of an interacting XXZ Hamiltonian with a pulsed quadratic magnetic field, which we expect will be the most natural implementation in analog quantum platforms (the inherent Trotterization of a kicking Hamiltonian naturally lends itself to digital quantum simulators [48]). We remark that such a distinction is only manifest at the level of the micromotion operator [49]. For the stroboscopic dynamics and Floquet level statistics analyzed in Fig. 4, the problems are identical and simply require a relabeling of parameters. In particular for the interpretation we take with a pulsed quadratic field,  $K/\hbar$  should be reinterpreted as a spin-spin coupling multiplied by the kicking period, and  $\hbar$  as the magnetic field impulse.

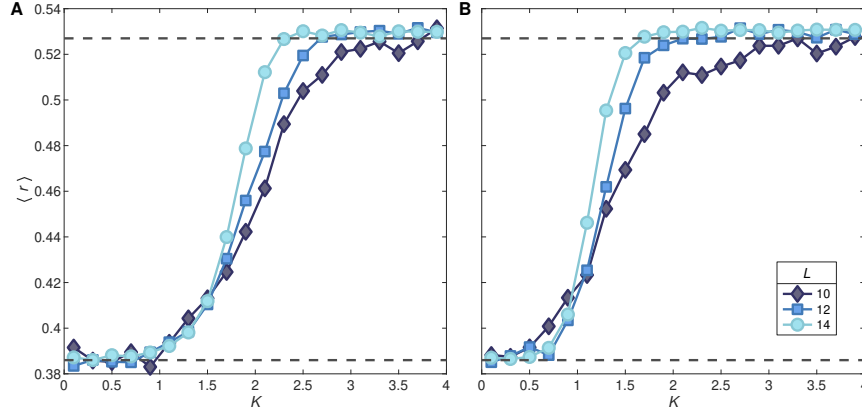


Fig. S8. **Transition from MBDL to ergodicity for kicked XXZ model.** (A) Gap-ratio statistic for  $k = 1$ ,  $\Delta = 0.5$  and averaging over a Gaussian ensemble of  $\beta$  with standard deviation 0.1 for varying  $K$  and  $L$ . (B) The same parameters except  $\Delta = 2$ . Dashed horizontal lines indicate the same Poisson and circular-orthogonal ensemble predictions of Fig. 4H.

### 2.8. MBDL for anisotropic kicked XXZ chains

Here we show that the isotropic  $\Delta = 1$  case considered in Fig. 4 is not a fine-tuned point for realizing MBDL in the kicked XXZ model. In Fig. S8A and B, we show the gap-ratio parameter computed for  $\Delta = 0.5$  and  $\Delta = 2$  respectively. In both cases we observe a transition from MBDL to chaos as the interaction strength  $K$  is increased, which is qualitatively similar to that of the  $\Delta = 1$  case. We find that the region of  $K$  for which the MBDL phase exists shrinks as the value of  $\Delta$  is increased. For  $\Delta = 0$  (noninteracting), we find that  $\langle r \rangle$  agrees with the Poisson prediction for all values of  $K$  shown here.

# Bibliography

- [1] A. Cao, C. J. Fujiwara, R. Sajjad, E. Q. Simmons, E. Lindroth, and D. Weld, *Probing nonexponential decay in floquet–bloch bands*, *Zeitschrift für Naturforschung A* **75** (2020), no. 5 443–448.
- [2] A. Cao, R. Sajjad, E. Q. Simmons, C. J. Fujiwara, T. Shimasaki, and D. M. Weld, *Transport controlled by poincaré orbit topology in a driven inhomogeneous lattice gas*, *Phys. Rev. Research* **2** (Aug, 2020) 032032.
- [3] A. Cao, R. Sajjad, H. Mas, E. Q. Simmons, J. L. Tanlimco, E. Nolasco-Martinez, T. Shimasaki, H. E. Kondakci, V. Galitski, and D. M. Weld, *Prethermal dynamical localization and the emergence of chaos in a kicked interacting quantum gas*, 2021.
- [4] Z. Geiger, *An Apparatus for Dynamical Quantum Emulation Using Ultracold Lithium*. PhD thesis, UC Santa Barbara, 2017.
- [5] K. Singh, *Floquet Engineering with Ultracold Lithium in Optical Lattices*. PhD thesis, UC Santa Barbara, 2018.
- [6] C. Fujiwara, *Dynamics of Ultracold Lithium in Modulated Optical Lattices*. PhD thesis, UC Santa Barbara, 2019.
- [7] W. Ketterle, D. S. Durfee, and D. Stamper-Kurn, *Making, probing and understanding bose-einstein condensates*, cond-mat/9904034.
- [8] O. Morsch and M. Oberthaler, *Dynamics of bose-einstein condensates in optical lattices*, *Rev. Mod. Phys.* **78** (Feb, 2006) 179–215.
- [9] F. Dalfovo, S. Giorgini, L. P. Pitaevskii, and S. Stringari, *Theory of bose-einstein condensation in trapped gases*, *Rev. Mod. Phys.* **71** (Apr, 1999) 463–512.
- [10] A. J. Leggett, *Bose-einstein condensation in the alkali gases: Some fundamental concepts*, *Rev. Mod. Phys.* **73** (Apr, 2001) 307–356.
- [11] *Bose-Einstein Condensation in Dilute Gases*. Cambridge University Press, 2008.

- [12] S. E. Pollack, D. Dries, M. Junker, Y. P. Chen, T. A. Corcovilos, and R. G. Hulet, *Extreme tunability of interactions in a  $^7\text{Li}$  bose-einstein condensate*, *Phys. Rev. Lett.* **102** (Mar, 2009) 090402.
- [13] T. Hartmann, F. Keck, H. J. Korsch, and S. Mossman, *Dynamics of bloch oscillations*, *New Journal of Physics* **6** (2004) 2.
- [14] M. Glück, A. R. Kolovsky, and H. J. Korsch, *Wannier–stark resonances in optical and semiconductor superlattices*, *Physics Reports* **366** (2002), no. 3 103 – 182.
- [15] Z. A. Geiger, K. M. Fujiwara, K. Singh, R. Senaratne, S. V. Rajagopal, M. Lipatov, T. Shimasaki, R. Driben, V. V. Konotop, T. Meier, and D. M. Weld, *Observation and uses of position-space bloch oscillations in an ultracold gas*, *Phys. Rev. Lett.* **120** (May, 2018) 213201.
- [16] M. Holthaus, *Floquet engineering with quasienergy bands of periodically driven optical lattices*, *Journal of Physics B: Atomic, Molecular and Optical Physics* **49** (nov, 2015) 013001.
- [17] A. Eckardt, *Colloquium: Atomic quantum gases in periodically driven optical lattices*, *Rev. Mod. Phys.* **89** (Mar, 2017) 011004.
- [18] C. J. Fujiwara, K. Singh, Z. A. Geiger, R. Senaratne, S. V. Rajagopal, M. Lipatov, and D. M. Weld, *Transport in floquet-bloch bands*, *Phys. Rev. Lett.* **122** (Jan, 2019) 010402.
- [19] A. Cao, C. J. Fujiwara, R. Sajjad, E. Q. Simmons, E. Lindroth, and D. Weld, *Probing nonexponential decay in floquet–bloch bands*, *Zeitschrift für Naturforschung A* **75** (Mar, 2020) 443–448.
- [20] J. J. Sakurai, *Modern Quantum Mechanics Revised Edition*. Addison-Wesley, 1994.
- [21] L. A. Khal'fin, *Contribution to the decay theory of a quasi-stationary state*, *Sov. Phys. JETP* **6** (1958) 1371.
- [22] *Seeking non-exponential decay*, .
- [23] R. G. Winter, *Evolution of a quasi-stationary state*, *Phys. Rev.* **123** (Aug, 1961) 1503–1507.
- [24] L. Fonda, G. C. Ghirardi, and A. Rimini, *Decay theory of unstable quantum systems*, *Reports on Progress in Physics* **58** (1978) 587.
- [25] S. Wilkinson, C. F. Bharucha, M. C. Fischer, K. W. Madison, P. R. Morrow, Q. Niu, B. Sundaram, and M. G. Raizen, *Experimental evidence for non-exponential decay in quantum tunnelling*, *Nature* **387** (1997) 575–577.

- [26] Q. Niu and M. G. Raizen, *How landau-zener tunneling takes time*, *Phys. Rev. Lett.* **80** (Apr, 1998) 3491–3494.
- [27] C. Rothe, S. I. Hintschich, and A. P. Monkman, *Violation of the exponential-decay law at long times*, *Phys. Rev. Lett.* **96** (Apr, 2006) 163601.
- [28] A. Crespi, F. V. Pepe, P. Facchi, F. Sciarrino, P. Mataloni, H. Nakazato, S. Pascazio, and R. Osellame, *Experimental investigation of quantum decay at short, intermediate, and long times via integrated photonics*, *Phys. Rev. Lett.* **122** (Apr, 2019) 130401.
- [29] D. Steck, *Quantum and atom optics*, 2019.
- [30] E. B. Norman, S. B. Gazes, S. G. Crane, and D. A. Bennett, *Tests of the exponential decay law at short and long times*, *Phys. Rev. Lett.* **60** (May, 1988) 2246–2249.
- [31] A. Cao, R. Sajjad, E. Q. Simmons, C. J. Fujiwara, T. Shimasaki, and D. M. Weld, *Transport controlled by poincaré orbit topology in a driven inhomogeneous lattice gas*, *Physical Review Research* **2** (Aug, 2020).
- [32] V. V. Ivanov, A. Alberti, M. Schioppo, G. Ferrari, M. Artoni, M. L. Chiofalo, and G. M. Tino, *Coherent delocalization of atomic wave packets in driven lattice potentials*, *Phys. Rev. Lett.* **100** (Jan, 2008) 043602.
- [33] A. Alberti, V. V. Ivanov, G. M. Tino, and G. Ferrari, *Engineering the quantum transport of atomic wavefunctions over macroscopic distances*, *Nat. Phys.* **5** (2009) 547–550.
- [34] C. Sias, H. Lignier, Y. P. Singh, A. Zenesini, D. Ciampini, O. Morsch, and E. Arimondo, *Observation of photon-assisted tunneling in optical lattices*, *Phys. Rev. Lett.* **100** (Feb, 2008) 040404.
- [35] S. R. Wilkinson, C. F. Bharucha, K. W. Madison, Q. Niu, and M. G. Raizen, *Observation of atomic wannier-stark ladders in an accelerating optical potential*, *Phys. Rev. Lett.* **76** (Jun, 1996) 4512–4515.
- [36] E. Haller, R. Hart, M. J. Mark, J. G. Danzl, L. Reichsöllner, and H.-C. Nägerl, *Inducing transport in a dissipation-free lattice with super bloch oscillations*, *Phys. Rev. Lett.* **104** (May, 2010) 200403.
- [37] D. H. Dunlap and V. M. Kenkre, *Dynamic localization of a charged particle moving under the influence of an electric field*, *Phys. Rev. B* **34** (Sep, 1986) 3625–3633.

- [38] Q. Thommen, J. C. Garreau, and V. Zehnlé, *Theoretical analysis of quantum dynamics in one-dimensional lattices: Wannier-stark description*, *Phys. Rev. A* **65** (Apr, 2002) 053406.
- [39] H. Korsch and S. Mossman, *An algebraic solution of driven single band tight binding dynamics*, *Phys. Lett. A* **317** (2003) 54–63.
- [40] K. Kudo and T. S. Monteiro, *Theoretical analysis of super-bloch oscillations*, *Phys. Rev. A* **83** (May, 2011) 053627.
- [41] A. Eckardt, M. Holthaus, H. Lignier, A. Zenesini, D. Ciampini, O. Morsch, and E. Arimondo, *Exploring dynamic localization with a bose-einstein condensate*, *Phys. Rev. A* **79** (Jan, 2009) 013611.
- [42] A. Alberti, G. Ferrari, V. V. Ivanov, M. L. Chiofalo, and G. M. Tino, *Atomic wave packets in amplitude-modulated vertical optical lattices*, .
- [43] M. Clifford and S. Bishop, *Rotating periodic orbits of the parametrically excited pendulum*, *Phys. Lett. A* **201** (1995) 191.
- [44] X. Xu, M. Wiercigroch, and P. Cartmell, *Rotating orbits of the parametrically-excited pendulum*, *Chaos, Solitons and Fractals* **23** (2004) 1537.
- [45] D. Capecchi and S. R. Bishop, *Periodic oscillations and attracting basins for a parametrically excited pendulum*, *Dynamics and Stability of Systems* **9** (1994) 123.
- [46] E. Díaz, A. García Mena, K. Asakura, and C. Gaul, *Super-bloch oscillations with modulated interaction*, *Phys. Rev. A* **87** (Jan, 2013) 015601.
- [47] R. Ma, M. E. Tai, P. M. Preiss, W. S. Bakr, J. Simon, and M. Greiner, *Photon-assisted tunneling in a biased strongly correlated bose gas*, *Phys. Rev. Lett.* **107** (Aug, 2011) 095301.
- [48] B. V. Chirikov, *Research concerning the theory of non-linear resonance and stochasticity*. CERN, Geneva, 1971. Translated at CERN from the Russian (IYAF-267-TRANS-E).
- [49] B. V. Chirikov, *A universal instability of many-dimensional oscillator systems*, *Physics Reports* **52** (1979), no. 5 263 – 379.
- [50] B. Chirikov and D. Shepelyansky, *Chirikov standard map*, *Scholarpedia* **3** (2008), no. 3 3550. revision #194619.
- [51] G. Casati, B. V. Chirikov, F. M. Israeliev, and J. Ford, vol. 93 of *Lecture Notes in Physics*, p. 334–352. Springer Berlin Heidelberg, 1979.

- [52] F. Izrailev and Shepelyanskii, *Quantum resonance for a rotator in a nonlinear periodic field*, *Theor. Math. Phys.* **43** (1980) 553–561.
- [53] S. Fishman, D. R. Grempel, and R. E. Prange, *Chaos, quantum recurrences, and anderson localization*, *Phys. Rev. Lett.* **49** (Aug, 1982) 509–512.
- [54] D. R. Grempel, R. E. Prange, and S. Fishman, *Quantum dynamics of a nonintegrable system*, *Phys. Rev. A* **29** (Apr, 1984) 1639–1647.
- [55] P. W. Anderson, *Absence of diffusion in certain random lattices*, *Phys. Rev.* **109** (Mar, 1958) 1492–1505.
- [56] F. L. Moore, J. C. Robinson, C. F. Bharucha, B. Sundaram, and M. G. Raizen, *Atom optics realization of the quantum  $\delta$ -kicked rotor*, *Phys. Rev. Lett.* **75** (Dec, 1995) 4598–4601.
- [57] S. Wimberger, M. Sadgrove, S. Parkins, and R. Leonhardt, *Experimental verification of a one-parameter scaling law for the quantum and “classical” resonances of the atom-optics kicked rotor*, *Phys. Rev. A* **71** (May, 2005) 053404.
- [58] G. J. Duffy, S. Parkins, T. Müller, M. Sadgrove, R. Leonhardt, and A. C. Wilson, *Experimental investigation of early-time diffusion in the quantum kicked rotor using a bose-einstein condensate*, *Phys. Rev. E* **70** (Nov, 2004) 056206.
- [59] C. Ryu, M. F. Andersen, A. Vaziri, M. B. d’Arcy, J. M. Grossman, K. Helmerson, and W. D. Phillips, *High-order quantum resonances observed in a periodically kicked bose-einstein condensate*, *Phys. Rev. Lett.* **96** (Apr, 2006) 160403.
- [60] B. G. Klappauf, W. H. Oskay, D. A. Steck, and M. G. Raizen, *Experimental study of quantum dynamics in a regime of classical anomalous diffusion*, *Phys. Rev. Lett.* **81** (Nov, 1998) 4044–4047.
- [61] M. B. d’Arcy, R. M. Godun, M. K. Oberthaler, D. Cassettari, and G. S. Summy, *Quantum enhancement of momentum diffusion in the delta-kicked rotor*, *Phys. Rev. Lett.* **87** (Jul, 2001) 074102.
- [62] M. K. Oberthaler, R. M. Godun, M. B. d’Arcy, G. S. Summy, and K. Burnett, *Observation of quantum accelerator modes*, *Phys. Rev. Lett.* **83** (Nov, 1999) 4447–4451.
- [63] J. Chabé, G. Lemarié, B. Grémaud, D. Delande, P. Szriftgiser, and J. C. Garreau, *Experimental observation of the anderson metal-insulator transition with atomic matter waves*, *Phys. Rev. Lett.* **101** (Dec, 2008) 255702.
- [64] M. Lopez, J.-F. m. c. Clément, P. Szriftgiser, J. C. Garreau, and D. Delande, *Experimental test of universality of the anderson transition*, *Phys. Rev. Lett.* **108** (Feb, 2012) 095701.

- [65] I. Manai, J.-F. m. c. Clément, R. Chicireanu, C. Hainaut, J. C. Garreau, P. Szriftgiser, and D. Delande, *Experimental observation of two-dimensional anderson localization with the atomic kicked rotor*, *Phys. Rev. Lett.* **115** (Dec, 2015) 240603.
- [66] A. Ullah, S. Ruddell, J. Currivan, and M. Hoogerland, *Quantum resonant effects in the delta-kicked rotor revisited*, *Eur. Phys. Jour. D.* **66** (2012) 315.
- [67] B. Gadway, D. Pertot, R. Reimann, M. G. Cohen, and D. Schneble, *Analysis of kapitza-dirac diffraction patterns beyond the raman-nath regime*, *Opt. Express* **17** (Oct, 2009) 19173–19180.
- [68] Y. B. Ovchinnikov, J. H. Müller, M. R. Doery, E. J. D. Vredenburg, K. Helmerson, S. L. Rolston, and W. D. Phillips, *Diffraction of a released bose-einstein condensate by a pulsed standing light wave*, *Phys. Rev. Lett.* **83** (Jul, 1999) 284–287.
- [69] B. Klappauf, W. Oskay, D. Steck, and M. Raizen, *Quantum chaos with cesium atoms: pushing the boundaries*, *Physica D* **131** (1999), no. 1 78–89.
- [70] D. A. Abanin, E. Altman, I. Bloch, and M. Serbyn, *Colloquium: Many-body localization, thermalization, and entanglement*, *Rev. Mod. Phys.* **91** (May, 2019) 021001.
- [71] D. M. Basko, I. L. Aleiner, and B. L. Altshuler, *Metal-insulator transition in a weakly interacting many-electron system with localized single-particle states*, *Ann. Phys. (Amsterdam)* **321** (2006) 1126–1205.
- [72] I. V. Gornyi, A. D. Mirlin, and D. G. Polyakov, *Interacting electrons in disordered wires: Anderson localization and low- $t$  transport*, *Phys. Rev. Lett.* **95** (Nov, 2005) 206603.
- [73] V. Oganesyan and D. A. Huse, *Localization of interacting fermions at high temperature*, *Phys. Rev. B* **75** (Apr, 2007) 155111.
- [74] A. Pal and D. A. Huse, *Many-body localization phase transition*, *Phys. Rev. B* **82** (Nov, 2010) 174411.
- [75] M. Schreiber, S. S. Hodgman, P. Bordia, H. P. Lüschen, M. H. Fischer, R. Vosk, E. Altman, U. Schneider, and I. Bloch, *Observation of many-body localization of interacting fermions in a quasirandom optical lattice*, *Science* **349** (2015), no. 6250 842–845.
- [76] J.-y. Choi, S. Hild, J. Zeiher, P. Schauß, A. Rubio-Abadal, T. Yefsah, V. Khemani, D. A. Huse, I. Bloch, and C. Gross, *Exploring the many-body localization transition in two dimensions*, *Science* **352** (2016), no. 6293 1547–1552.

- [77] J. Smith, A. Lee, B. Neyenhuis, P. W. Hess, P. Hauke, M. Heyl, D. A. Huse, and C. Monroe, *Many-body localization in a quantum simulator with programmable random disorder*, *Nat. Phys.* **12** (2016) 907–911.
- [78] P. Roushan, C. Neill, J. Tangpanitanon, V. M. Bastidas, A. Megrant, R. Barends, Y. Chen, Z. Chen, B. Chiaro, A. Dunsworth, A. Fowler, B. Foxen, M. Giustina, E. Jeffrey, J. Kelly, E. Lucero, J. Mutus, M. Neeley, C. Quintana, D. Sank, A. Vainsencher, J. Wenner, T. White, H. Neven, D. G. Angelakis, and J. Martinis, *Spectroscopic signatures of localization with interacting photons in superconducting qubits*, *Science* **358** (2017), no. 6367 1175–1179.
- [79] A. C. Keser, S. Ganeshan, G. Refael, and V. Galitski, *Dynamical many-body localization in an integrable model*, *Phys. Rev. B* **94** (Aug, 2016) 085120.
- [80] C. Rylands, E. B. Rozenbaum, V. Galitski, and R. Konik, *Many-body dynamical localization in a kicked lieb-liniger gas*, *Phys. Rev. Lett.* **124** (Apr, 2020) 155302.
- [81] R. Chicireanu and A. Rançon, *Dynamical localization of interacting bosons in the few-body limit*, *Phys. Rev. A* **103** (Apr, 2021) 043314.
- [82] M. Fava, R. Fazio, and A. Russomanno, *Many-body dynamical localization in the kicked bose-hubbard chain*, *Phys. Rev. B* **101** (Feb, 2020) 064302.
- [83] V. Vuetelet and A. Rançon, *Effective thermalization of a many-body dynamically localized bose gas*, 2021.
- [84] D. L. Shepelyansky, *Delocalization of quantum chaos by weak nonlinearity*, *Phys. Rev. Lett.* **70** (Mar, 1993) 1787–1790.
- [85] J. Reslen, C. E. Creffield, and T. S. Monteiro, *Dynamical instability in kicked bose-einstein condensates*, *Phys. Rev. A* **77** (Apr, 2008) 043621.
- [86] P. Qin, A. Andreanov, H. C. Park, and S. Flach, *Interacting ultracold atomic kicked rotors: loss of dynamical localization*, *Sci Rep* **7** (2017) 41139.
- [87] L. Rebuzzini, S. Wimberger, and R. Artuso, *Delocalized and resonant quantum transport in nonlinear generalizations of the kicked rotor model*, *Phys. Rev. E* **71** (Mar, 2005) 036220.
- [88] J. Liu, C. Zhang, M. G. Raizen, and Q. Niu, *Transition to instability in a periodically kicked bose-einstein condensate on a ring*, *Phys. Rev. A* **73** (Jan, 2006) 013601.
- [89] S. Lellouch, A. Rançon, S. De Bièvre, D. Delande, and J. C. Garreau, *Dynamics of the mean-field-interacting quantum kicked rotor*, *Phys. Rev. A* **101** (Apr, 2020) 043624.

- [90] G. Gligorić, J. D. Bodyfelt, and S. Flach, *Interactions destroy dynamical localization with strong and weak chaos*, *Europhys. Lett.* **96** (oct, 2011) 30004.
- [91] B. Vermersch, D. Delande, and J. C. Garreau, *Bogoliubov excitations in the quasiperiodic kicked rotor: Stability of a kicked condensate and the quasi-insulator-to-metal transition*, *Phys. Rev. A* **101** (May, 2020) 053625.
- [92] S. Notarnicola, A. Silva, R. Fazio, and A. Russomanno, *Slow heating in a quantum coupled kicked rotors system*, *J. Stat. Mech.* (2020) 024008.
- [93] A. Tenart, C. Carcy, H. Cayla, T. Bourdel, M. Mancini, and D. Clément, *Two-body collisions in the time-of-flight dynamics of lattice bose superfluids*, *Phys. Rev. Research* **2** (Jan, 2020) 013017.
- [94] P. Deuar and P. D. Drummond, *Correlations in a bec collision: First-principles quantum dynamics with 150 000 atoms*, *Phys. Rev. Lett.* **98** (Mar, 2007) 120402.
- [95] P. Ziń, J. Chwedeńczuk, A. Veitia, K. Rzażewski, and M. Trippenbach, *Quantum multimode model of elastic scattering from bose-einstein condensates*, *Phys. Rev. Lett.* **94** (May, 2005) 200401.
- [96] Y. B. Band, M. Trippenbach, J. P. Burke, and P. S. Julienne, *Elastic scattering loss of atoms from colliding bose-einstein condensate wave packets*, *Phys. Rev. Lett.* **84** (Jun, 2000) 5462–5465.
- [97] A. Perrin, H. Chang, V. Krachmalnicoff, M. Schellekens, D. Boiron, A. Aspect, and C. I. Westbrook, *Observation of atom pairs in spontaneous four-wave mixing of two colliding bose-einstein condensates*, *Phys. Rev. Lett.* **99** (Oct, 2007) 150405.
- [98] M. Ueda, *Quantum equilibration, thermalization and prethermalization in ultracold atoms*, *Nature Reviews Physics* (2020) 1–13.
- [99] W. H. Oskay, D. A. Steck, and M. G. Raizen, *Timing noise effects on dynamical localization*, *Chaos, Solitons and Fractals* **16** (2003), no. 3 409–416.
- [100] D. H. White, S. K. Ruddell, and M. D. Hoogerland, *Phase noise in the delta kicked rotor: from quantum to classical*, *New Journal of Physics* **16** (nov, 2014) 113039.
- [101] B. G. Klappauf, W. H. Oskay, D. A. Steck, and M. G. Raizen, *Observation of noise and dissipation effects on dynamical localization*, *Phys. Rev. Lett.* **81** (Aug, 1998) 1203–1206.
- [102] H. Ammann, R. Gray, I. Shvarchuck, and N. Christensen, *Quantum delta-kicked rotor: Experimental observation of decoherence*, *Phys. Rev. Lett.* **80** (May, 1998) 4111–4115.

- [103] A. S. Pikovsky and D. L. Shepelyansky, *Destruction of anderson localization by a weak nonlinearity*, *Phys. Rev. Lett.* **100** (Mar, 2008) 094101.
- [104] S. Flach, D. O. Krimer, and C. Skokos, *Universal spreading of wave packets in disordered nonlinear systems*, *Phys. Rev. Lett.* **102** (Jan, 2009) 024101.
- [105] V. Vuatelet and A. Rançon, *Effective thermalization of a many-body dynamically localized bose gas*, 2021.
- [106] B. Daszuta and M. F. Andersen, *Atom interferometry using  $\delta$ -kicked and finite-duration pulse sequences*, *Phys. Rev. A* **86** (Oct, 2012) 043604.
- [107] J. Mangaonkar, C. Vishwakarma, S. S. Maurya, S. Sarkar, J. L. MacLennan, P. Dutta, and U. D. Rapol, *Effects of finite momentum width on the reversal dynamics in a bec based atom optics delta-kicked rotor*, *Journal of Physics B: Atomic, Molecular and Optical Physics* **53** (nov, 2020) 235502.
- [108] M. Delvecchio, C. Groiseau, F. Petiziol, G. S. Summy, and S. Wimberger, *Quantum search with a continuous-time quantum walk in momentum space*, *Journal of Physics B: Atomic, Molecular and Optical Physics* **53** (feb, 2020) 065301.
- [109] A. Ullah and M. D. Hoogerland, *Experimental observation of loschmidt time reversal of a quantum chaotic system*, *Phys. Rev. E* **83** (Apr, 2011) 046218.
- [110] J. Martin, B. Georgeot, and D. L. Shepelyansky, *Cooling by time reversal of atomic matter waves*, *Phys. Rev. Lett.* **100** (Feb, 2008) 044106.
- [111] T. S. Monteiro, A. Rançon, and J. Ruostekoski, *Nonlinear resonances in  $\delta$ -kicked bose-einstein condensates*, *Phys. Rev. Lett.* **102** (Jan, 2009) 014102.
- [112] M. Lepers, V. Zehnlé, and J. C. Garreau, *Kicked-rotor quantum resonances in position space*, *Phys. Rev. A* **77** (Apr, 2008) 043628.
- [113] S. Wimberger, I. Guarneri, and S. Fishman, *Classical scaling theory of quantum resonances*, *Phys. Rev. Lett.* **92** (Feb, 2004) 084102.
- [114] I. Dana and D. L. Dorofeev, *General quantum resonances of the kicked particle*, *Phys. Rev. E* **73** (Feb, 2006) 026206.
- [115] T. Gorin, T. Prosen, T. H. Seligman, and M. Žnidarič, *Dynamics of loschmidt echoes and fidelity decay*, *Phys. Rep.* **435** (2006), no. 2 33–156.
- [116] B. Swingle, G. Bentsen, M. Schleier-Smith, and P. Hayden, *Measuring the scrambling of quantum information*, *Phys. Rev. A* **94** (Oct, 2016) 040302.

- [117] E. B. Rozenbaum, S. Ganeshan, and V. Galitski, *Lyapunov exponent and out-of-time-ordered correlator's growth rate in a chaotic system*, *Phys. Rev. Lett.* **118** (Feb, 2017) 086801.
- [118] E. J. Meier, F. A. An, and B. Gadway, *Atom-optics simulator of lattice transport phenomena*, *Phys. Rev. A* **93** (May, 2016) 051602.
- [119] X. Mi, P. Roushan, C. Quintana, S. Mandra, J. Marshall, C. Neill, F. Arute, K. Arya, J. Atalaya, R. Babbush, J. C. Bardin, R. Barends, A. Bengtsson, S. Boixo, A. Bourassa, M. Broughton, B. B. Buckley, D. A. Buell, B. Burkett, N. Bushnell, Z. Chen, B. Chiaro, R. Collins, W. Courtney, S. Demura, A. R. Derk, A. Dunsworth, D. Eppens, C. Erickson, E. Farhi, A. G. Fowler, B. Foxen, C. Gidney, M. Giustina, J. A. Gross, M. P. Harrigan, S. D. Harrington, J. Hilton, A. Ho, S. Hong, T. Huang, W. J. Huggins, L. B. Ioffe, S. V. Isakov, E. Jeffrey, Z. Jiang, C. Jones, D. Kafri, J. Kelly, S. Kim, A. Kitaev, P. V. Klimov, A. N. Korotkov, F. Kostritsa, D. Landhuis, P. Laptev, E. Lucero, O. Martin, J. R. McClean, T. McCourt, M. McEwen, A. Megrant, K. C. Miao, M. Mohseni, W. Mruczkiewicz, J. Mutus, O. Naaman, M. Neeley, M. Newman, M. Y. Niu, T. E. O'Brien, A. Opremcak, E. Ostby, B. Pato, A. Petukhov, N. Redd, N. C. Rubin, D. Sank, K. J. Satzinger, V. Shvarts, D. Strain, M. Szalay, M. D. Trevithick, B. Villalonga, T. White, Z. J. Yao, P. Yeh, A. Zalcman, H. Neven, I. Aleiner, K. Kechedzhi, V. Smelyanskiy, and Y. Chen, *Information scrambling in computationally complex quantum circuits*, 2021.
- [120] T. Boness, S. Bose, and T. S. Monteiro, *Entanglement and dynamics of spin chains in periodically pulsed magnetic fields: Accelerator modes*, *Phys. Rev. Lett.* **96** (May, 2006) 187201.
- [121] T. Boness, K. Kudo, and T. S. Monteiro, *Doubly excited ferromagnetic spin chain as a pair of coupled kicked rotors*, *Phys. Rev. E* **81** (Apr, 2010) 046201.
- [122] E. Lieb, T. Schultz, and D. Mattis, *Two soluble models of an antiferromagnetic chain*, *Annals of Physics* **16** (1961), no. 3 407–466.
- [123] L. D'Alessio and M. Rigol, *Long-time behavior of isolated periodically driven interacting lattice systems*, *Phys. Rev. X* **4** (Dec, 2014) 041048.
- [124] M. Rigol, V. Dunjko, and M. Olshanii, *Thermalization and its mechanism for generic isolated quantum systems*, *Nature* **452** (2008), no. 7189 854–858.
- [125] C. Monroe, W. C. Campbell, L.-M. Duan, Z.-X. Gong, A. V. Gorshkov, P. W. Hess, R. Islam, K. Kim, N. M. Linke, G. Pagano, P. Richerme, C. Senko, and N. Y. Yao, *Programmable quantum simulations of spin systems with trapped ions*, *Rev. Mod. Phys.* **93** (Apr, 2021) 025001.

- [126] A. Browaeys and T. Lahaye, *Many-body physics with individually controlled rydberg atoms*, *Nat. Phys.* **16** (2020), no. 2 132–142.
- [127] Y. Salathé, M. Mondal, M. Oppliger, J. Heinsoo, P. Kurpiers, A. Potočnik, A. Mezzacapo, U. Las Heras, L. Lamata, E. Solano, S. Filipp, and A. Wallraff, *Digital quantum simulation of spin models with circuit quantum electrodynamics*, *Phys. Rev. X* **5** (Jun, 2015) 021027.
- [128] X. Antoine, W. Bao, and C. Besse, *Computational methods for the dynamics of the nonlinear schrödinger/gross–pitaevskii equations*, *Computer Physics Communications* **184** (2013), no. 12 2621 – 2633.
- [129] B. Schmidt and U. Lorenz, *Wavepacket: A matlab package for numerical quantum dynamics. i: Closed quantum systems and discrete variable representations*, *Computer Physics Communications* **213** (2017) 223 – 234.
- [130] X. Antoine and R. Duboscq, *Gpelab, a matlab toolbox to solve gross–pitaevskii equations ii: Dynamics and stochastic simulations*, *Computer Physics Communications* **193** (2015) 95 – 117.
- [131] A. Askar and A. S. Cakmak, *Explicit integration method for the time-dependent schrodinger equation for collision problems*, *The Journal of Chemical Physics* **68** (1978), no. 6 2794–2798, [<https://aip.scitation.org/doi/pdf/10.1063/1.436072>].
- [132] M. A. Ajaib, *Numerical methods and causality in physics*, 2013.
- [133] S. Teukolsky, W. H. Press, and W. T. Vetterling, *Numerical Recipes: The Art of Scientific Computing*. Cambridge University Press, 2007.
- [134] V. Xu, M. Jaffe, C. D. Panda, S. L. Kristensen, L. W. Clark, and H. Müller, *Probing gravity by holding atoms for 20 seconds*, *Science* **366** (2019), no. 6466 745–749, [<https://science.sciencemag.org/content/366/6466/745.full.pdf>].
- [135] S. Kling, T. Salger, C. Grossert, and M. Weitz, *Atomic bloch-zener oscillations and stückelberg interferometry in optical lattices*, *Phys. Rev. Lett.* **105** (Nov, 2010) 215301.
- [136] P. Plotz and S. Wimberger, *St uckelberg-interferometry with ultra-cold atoms*, .
- [137] S. Shevchenko, S. Ashhab, and F. Nori, *Landau–zener–stückelberg interferometry*, *Physics Reports* **492** (2010), no. 1 1 – 30.
- [138] B. M. Garraway and N. V. Vitanov, *Population dynamics and phase effects in periodic level crossings*, *Phys. Rev. A* **55** (Jun, 1997) 4418–4432.

- [139] X. Li, M. Ke, B. Yan, and Y. Wang, *Reduction of interference fringes in absorption imaging of cold atom cloud using eigenface method*, *Chin. Opt. Lett.* **5** (Mar, 2007) 128–130.
- [140] C. F. Ockeloen, A. F. Tauschinsky, R. J. C. Spreeuw, and S. Whitlock, *Detection of small atom numbers through image processing*, *Phys. Rev. A* **82** (Dec, 2010) 061606.
- [141] L. Niu, X. Guo, Y. Zhan, X. Chen, W. M. Liu, and X. Zhou, *Optimized fringe removal algorithm for absorption images*, *Applied Physics Letters* **113** (2018), no. 14 144103, [<https://doi.org/10.1063/1.5040669>].
- [142] B. Song, C. He, Z. Ren, E. Zhao, J. Lee, and G.-B. Jo, *Effective statistical fringe removal algorithm for high-sensitivity imaging of ultracold atoms*, *Phys. Rev. Applied* **14** (Sep, 2020) 034006.